

Tribocorrosion behavior of novel nickel-free lean duplex stainless steel manufactured via laser-based powder bed fusion

Materials Engineering/Faculty of Technology

Master's thesis

Department of Mechanical and Materials Engineering

Author:

Abhinav Anand

Supervisors:

Assistant Professor Ashish Ganvir

Adjunct Professor Heidi Piili, D.Sc.(Tech.)

28.5.2024

Turku

The originality of this thesis has been checked in accordance with the University of Turku quality assurance system using the Turnitin Originality Check service.

Master's thesis

Subject: Materials Engineering

Author: Abhinav Anand

Title: Tribocorrosion behavior of novel nickel-free lean duplex stainless steel manufactured via laser-based powder bed fusion

Supervisors: Assistant Professor Ashish Ganvir, Adjunct Professor Heidi Piili, D.Sc.(Tech.)

Number of pages: 81 pages

Date: 28.5.2024

Laser-based powder bed fusion of metals (PBF-LB/M) is an additive manufacturing technology gaining attention in various industries due to its ability to allow design flexibility to fabricate complex structures precisely. In the marine sector, there is a growing interest in PBF-LB/M because of its potential to produce components such as heat exchangers, propeller shafts, impellers, and exhaust manifolds with lesser lead time, reduced cost, and customization. While 316L stainless steel has been a popular choice for marine applications due to its excellent corrosion resistance in seawater atmosphere, nickel-free duplex stainless steel (NiFDSS) emerges as a cost-effective and lightweight alternative, prompting research into its suitability for PBF-LB/M fabrication.

This thesis investigates the optimization of process parameters in PBF-LB/M of NiFDSS to attain defect-free samples. Experimental analyses focus on understanding the microstructural transformations of NiFDSS, transitioning from a fully ferritic to a duplex microstructure post-heat treatment. The study evaluates the tribological and corrosion properties of NiFDSS using a tribocorrosion setup under an artificial seawater environment.

Results obtained in this study indicate a relative density achievement of 98.83% for PBF-LB/Mod NiFDSS. Corrosion testing reveals superior corrosion resistance of NiFDSS, both in its as-built and heat-treated condition, compared to 316L. However, 316L exhibits better wear resistance characteristics. Further process optimization is needed to enhance the wear behavior of NiFDSS samples.

Overall, the study underscores the potential of NiFDSS as a viable alternative for marine components, particularly in applications where the wear rates are not very high, leveraging the design flexibility of PBF-LB/M to meet industry demands effectively.

Key words: Additive manufacturing, 3D printing, Laser-based powder bed fusion, Nickel-free stainless steel, Lean duplex steel, Tribology, Corrosion, Tribocorrosion, Heat treatment, Phase transformation

Acknowledgements

I am sincerely grateful to Asst. Prof. Ashish Ganvir for inducting me into the Digital Manufacturing and Surface Engineering (DMS) group and providing me with the opportunity to work on this thesis. His guidance, support, and mentorship have been instrumental throughout this work. I extend my gratitude to Prof. Heidi Piili for her unwavering support, insightful feedback, and invaluable guidance throughout the process. Her continuous encouragement and advice have contributed to refining my scientific writing and critical thinking skills since day one.

I express my sincere appreciation to Dr. Zaiqing Que from VTT, Espoo, for his assistance in obtaining the EBSD imaging and to Dr. Vahid Hosseini from ESAB Oy for his help with ThermoCalc simulations and for his suggestions for planning the heat treatment. I am thankful for the support and assistance of Mr. Aki Piironen, engineer of the DMS group, throughout this study. His help in acquiring lab equipment, particularly the densimeter, was invaluable to the success of this research.

I extend my gratitude to all members of the DMS group for creating a supportive environment. Special thanks to my lab mates Mathias Juan and Muhammad Ammar for their assistance during the experiments. Last but not least, I am deeply thankful to my family members for their love and affection throughout this journey.

Table of contents

1	Introduction	8
1.1	Background of the thesis	9
1.2	Outline of the thesis	11
1.3	Aim and research questions	12
1.4	Limitations of the study	12
2	Properties and applications of stainless steel	13
2.1	Austenitic stainless steel	16
2.2	Duplex stainless steel	18
3	Laser powder bed fusion of metals	20
3.1	PBF-LB of 316 L	25
3.2	PBF-LB of duplex stainless steel	28
3.2.1	PBF-LB/M of NiFDSS	30
4	Introduction to tribocorrosion	31
4.1	Principles of tribology	31
4.2	Electrochemistry of corrosion	34
4.3	Synergy of tribology and corrosion- Tribocorrosion	38
5	Aim and purpose of the experimental part	42
6	Experimental setup	44
7	Experimental procedure	47
7.1	Materials used	47
7.2	Powder characterization	47
7.3	Sample fabrication via PBF-LB/M	48
7.3.1	PBF-LB/M of 316L	48
7.3.2	Process parameter optimization of NiFDSS	49
7.4	Heat treatment of as-built NiFDSS	49
7.5	Material characterization of samples	50
7.6	Tribocorrosion tests	51
7.6.1	Corrosion test in static condition	51

7.6.2	Corrosion test in dynamic condition	52
8	Results and discussions	53
8.1	Optimized process parameters for NiFDSS	53
8.2	Microstructure and phase analysis	57
8.3	Tribocorrosion study	59
8.3.1	Wear analysis	59
8.3.2	Corrosion test in static condition	63
8.3.3	Corrosion test in dynamic condition	64
9	Conclusion	66
10	Further studies	67
	References	68
	Appendices	79
	Appendix 1 Ferritic stainless steel	79
	Appendix 2 Images	79

Nomenclature

Symbol	Explanation
A	Amperes
Cr_{eq}	Chromium equivalent
E_{corr}	Corrosion potential
D	Sliding distance
M	Molar
F_f	Frictional force
F_n	Normal load
g	Grams
I_{corr}	Corrosion current
keV	Kilo electron volt
kW	Kilowatts
K/s	Kelvin/second
mm	Millimeter
MPa	Megapascal
nA	Nanoampere
Ni_{eq}	Nickel equivalent
R	Wear track radius
V	Volts
Vol.	Volume
wt .%	Weight %
W_d	Wear depth
W_r	Wear rate
W_v	Wear volume
μm	Micrometer
γ	Austenite phase
δ	Delta ferrite phase
α	Ferrite phase
β_a, β_c	Tafel slopes
$^{\circ}\text{C}$	degree Celsius

Nomenclature

Abbreviation	Explanation
ASS	Austenitic stainless steel
AE	Auxiliary electrode
CAD	Computer-aided design
CE	Counter electrode
CoF	Coefficient of friction
C.R.	Corrosion rate
DSS	Duplex stainless steel
EDAX	Energy dispersive X-ray analysis
EIS	Electrochemical impedance spectroscopy
EBSD	Electron backscatter diffraction
HT	Heat treatment
LED	Laser energy density
NiFDSS	Nickel-free duplex stainless steel
OCP	Open circuit potential
PBF-LB/M	Laser-based powder bed fusion of metal
PPM	Parts per million
PREN	Pitting resistant equivalent number
RE	Reference electrode
RD	Relative density
RPM	Rotation per minute
SEM	Scanning electron microscopy
SS	Stainless steel
.STL	Standard tessellation language
WE	Working electrode
XRD	X-ray diffraction

1 Introduction

Stainless steels (SS) are iron alloys composed of a minimum of 10.5 % chromium, with carbon content below 1.2 %, and supplemented by various other alloying elements, including molybdenum, nickel, nitrogen, manganese, etc [1]. SS has widespread popularity in almost every industry due to its ability to resist corrosion by forming a passive layer of chromium oxide that inhibits contact with corrosive media [2]. SS has been categorized into four groups – austenite, ferrite, duplex, and martensite [3]. Austenite grades of SS contain a higher percentage of chromium, nickel, and molybdenum. It demonstrates exceptional corrosion resistance, possesses higher malleability and ductility, and accounts for over 70 % of SS production [4]. Ferrite grades offer good corrosion resistance but have lower toughness [5]. Duplex grades amalgamate both austenitic and ferritic phases, providing higher strength and superior corrosion resistance [6]. Martensite SS offers high strength but lower corrosion resistance than austenitic grades [7].

AISI 316L, an austenitic stainless steel (ASS), is the most popular SS grade. It has gained widespread acceptance in the marine, biomedical, food, and chemical processing industries over time due to its exceptional corrosion resistance, versatility, and durability, making it a preferred choice for applications where resistance to rust, erosion, and pitting is required [8]. Although duplex grades are less popular than AISI 316L, they present a compelling alternative. Duplex stainless steel (DSS) offers higher corrosion resistance, especially in seawater environments with chlorides and other aggressive substances [9]. Additionally, they have superior resistance to stress corrosion cracking compared to austenitic stainless steels [10]. Duplex grades are suitable candidates for applications requiring enhanced mechanical strength and toughness. Moreover, duplex alloys can be metallurgically tailored to optimize their properties in accordance with specific industrial needs [11].

The major hindrance in using DSS is its expensiveness compared to 316L due to higher alloying elements and complex manufacturing routes. To address cost considerations, lean duplex grades were developed in the mid-1980s to minimize the expense of raw materials, especially nickel [12]. The price of nickel has historically exhibited volatility, and by reducing nickel content, manufacturers have been able to provide customers with a more stable pricing structure, enhancing the economic appeal of lean DSS [13].

The Pitting Resistant Equivalent Number (PREN) has been used to quantify the corrosion resistance of stainless steel, especially pitting corrosion, which occurs in seawater environments, and its identification and effective control are very difficult [14]. The pitting corrosion resistance of stainless steel is assessed using the PREN, calculated by the formula:

$$PREN = Cr + 3.3 \times Mo \% + 16 \times N \% \quad (1)$$

where Cr, Mo, and N represent the weight percentages of chromium, molybdenum, and nitrogen in the steel, respectively [15]. The PREN value is around 30 for lean DSS grades and 25 for a typical 316L grade [16]. Therefore, lean duplex grades are commonly used in subsea components like flexible flowlines, anchor systems, and water injection lines exposed to chloride-induced atmospheric corrosion [17]. Their utility extends to applications such as heat exchangers, while in the chemical process industry, they are used in reactors, distillation columns, and storage tanks [Ref]. Additionally, these alloys can be employed in desalination plants and power generation facilities [Ref].

A new variant of lean DSS, nickel-free duplex stainless steel (NiFDSS), was first developed by researchers at ETH Zurich [18]. Increased amounts of nitrogen and manganese replaced nickel to improve stress corrosion cracking resistance and reduce cost. The alloy demonstrated a yield strength of at least 550 MPa and an elongation to fracture of at least 40%, attributed to interstitial solid solution strengthening by nitrogen. The absence of nickel provides excellent resistance to stress corrosion cracking in chloride solutions. The newly developed alloy costs only a quarter of the 316L cost.

The PREN value for NiFDSS used in this thesis is 30.82, higher than the 316L grade, making it particularly well-suited for less aggressive marine atmospheres and industries where moderate corrosion resistance is essential. Also, NiFDSS has 3% less density than 316L grades, allowing the design of lighter structures that are weight-saving.

1.1 Background of the thesis

Traditionally, steel components have predominantly been manufactured using conventional methods such as casting, forging, and machining. Additive manufacturing (AM), also known as 3D printing, is a process that builds three-dimensional objects layer by layer from CAD models [19]. This fabrication method, widely used in rapid prototyping and tailored designs, offers versatility along with precision in the field of manufacturing and eliminates the need for tooling, thereby streamlining the fabrication process and minimizing associated costs.

Metal-based additive manufacturing routes like laser-based powder bed fusion (PBF-LB/M) allow design flexibility, intricate geometries with capabilities of fabrication of complex and thin-walled geometries such as heat exchangers, and tailored solutions with potential cost efficiencies through reduced material waste and manufacturing time [20,21].

The prevailing literature on PBF-LB/M of stainless steels has primarily emphasized austenitic stainless steels, especially 316L grades. Several research and review papers have examined the corrosion, tribological, and mechanical properties of components made from 316L via PBF-LB/M [22–25]. Figure 1 shows the growing interest in PBF-LB/M of DSS over the years in the scientific community, suggesting that research in this domain is still in its early stages.

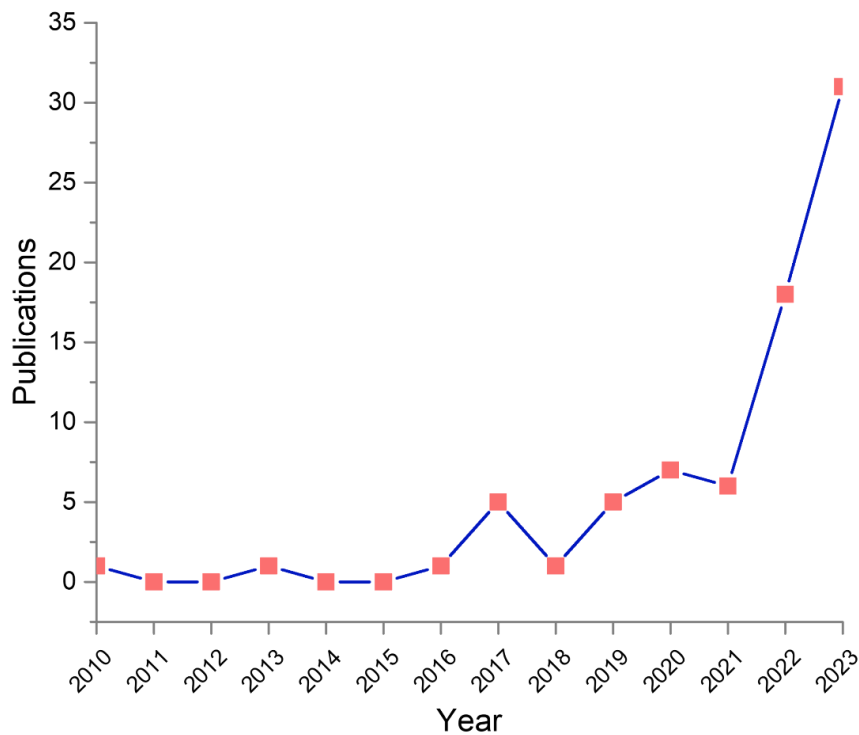


Figure 1. The publication trend of articles retrieved from the Scopus database using the keywords "Duplex Stainless Steel" and "PBF."

PBF-LB/Med DSS grades like NiFDSS offer versatile applications, including the manufacturing of boat propeller shafts, impellers, exhaust manifolds, compact heat exchangers, and integral components for marine systems like anchors and connectors [26]. Additionally, they can find utility in chemical processing, contributing to constructing corrosion-resistant pressure vessels. Only two documented studies report the production of NiFDSS samples using the PBF-LB/M [27,28].

Tribology studies are required for components operating in seawater environments, focusing on comprehending wear resistance, friction, and wear rate in harsh marine conditions [29]. Electrochemical corrosion testing can offer crucial insights by determining corrosion rates and resistance of specific alloys, aiding in evaluating their performance in corrosive conditions [30]. Similarly, tribocorrosion studies are essential for understanding how the components wear and corrode over time due to the combined effects of mechanical stress and exposure to seawater atmosphere [31]. No study has been reported discussing the tribological properties and corrosion resistance of NiFDSS samples fabricated by PBF-LB/M in an artificial seawater environment. Also, tribocorrosion studies of DSS grades fabricated via PBF-LB/M have yet to be conducted.

1.2 Outline of the thesis

The motivation behind this thesis is to fill this research gap. Figure 2 illustrates the research plan adopted in this study. As shown in Figure 2, this study begins with a literature review focusing on the properties and application of DSS, drawing a comparison with 316L grade. A detailed discussion of the PBF-LB/M of duplex and austenitic stainless steel will follow. A concise introduction to tribology, electrochemistry of corrosion, and tribocorrosion has also been provided.

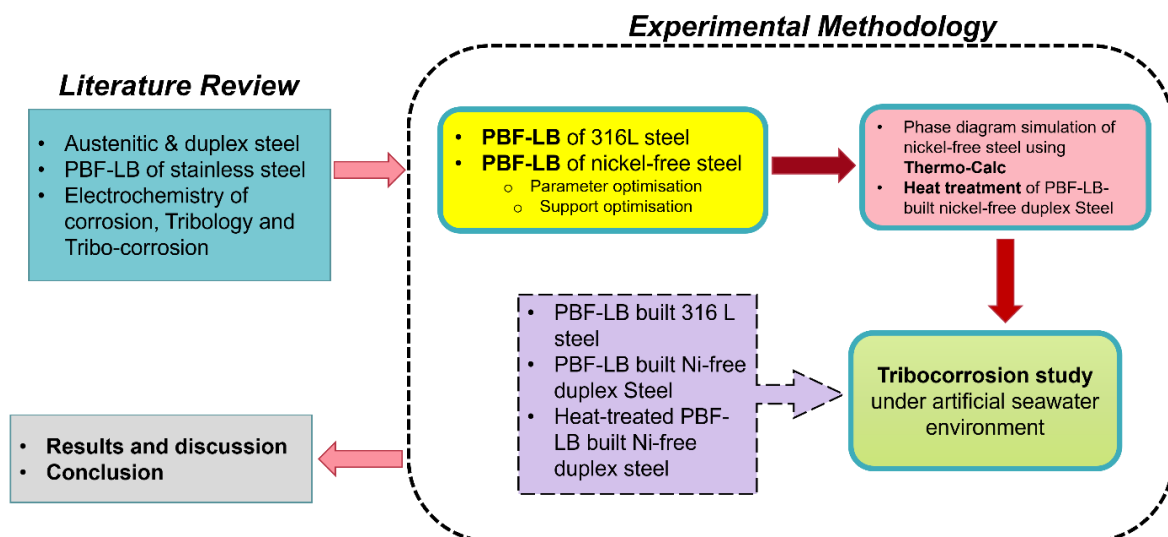


Figure 2. Research plan for the thesis

In the experimental part of this study, the NiFDSS samples were fabricated by optimizing supports and process parameters of PBF-LB/M. Based on the phase diagram computed by Thermo-Calc in the experimental part, the as-built samples were then subjected to heat treatment to undergo phase transformations from complete ferrite to a duplex phase consisting

of both austenite and ferrite in the microstructure. Then, the effect of heat treatment on tribological behavior and corrosion resistance under mechanical loading was analyzed. Throughout the study, PBF-LB/M-built 316L samples were kept as reference material for comparison, as the main aim of this study was to validate if NiFDSS samples could outperform 316L samples in terms of wear and corrosion resistance under seawater environment when the manufacturing route is through PBF-LB/M. Also, 316L samples were not subjected to any heat treatment in this study, as existing literature has already covered its impact on phase composition, tribological behavior, and corrosive properties [21,32–34].

1.3 Aim and research questions

The overall aim of this study is to validate if PBF-LB/M-built NiFDSS is an alternative to 316L for equipment used in seawater environments by answering the following research questions:

- Can NiFDSS fabricated through PBF-LB/M exhibit wear and corrosion resistance comparable to 316L, both in the absence of loading and under mechanical loading within a seawater environment?
- How does the phase transformation induced by heat treatment in PBF-LB-manufactured NiFDSS samples impact their tribological behavior and corrosion resistance?
- Is NiFDSS a viable choice for components in marine environments, and how can PBF-LB/M contribute to manufacturing these components?

1.4 Limitations of the study

The limitation of this thesis includes the lack of a comparative investigation into the mechanical properties of NiFDSS and 316L manufactured through PBF-LB/M. Despite the inclusion of microhardness testing, other mechanical tests, such as tensile and nano-indentation tests, remained unexplored. Moreover, this thesis focused only on uniform corrosion. The tribocorrosion tests were conducted under a single environmental setting, i.e., artificial seawater (0.6 M NaCl with pH 8.2), using only one specific test condition for both steel variants.

2 Properties and applications of stainless steel

Steel, an alloy of iron and carbon, offers enhanced durability and better fracture toughness compared to pure iron. When other alloying elements are absent except carbon, they are termed carbon steels. Mild steel, with its low carbon content (0.05 % to 0.32 %), combines affordability and malleability, making it suitable for structural applications and machine parts, and it allows cost-efficient machining [35]. Medium-carbon steel, with a carbon content of 0.3 % to 0.6 %, has a balance between the strength of high-carbon steel and the formability of low-carbon steel and is used in components requiring increased strength and toughness, such as gears, axels, pressure vessels, etc. [36]. High-carbon steel, with a carbon content of 0.60 % to 1.5 %, is in demand for applications requiring superior hardness, tensile strength, and wear resistance, such as in the production of springs [37]. However, its increased brittleness causes challenges in welding due to the high chances of cracking. Carbon steels often undergo galvanization for rust protection through a hot dip or electroplating with zinc [38]. However, this step doesn't guarantee resistance to corrosion during prolonged usage because if the zinc coating gets damaged, the underlying steel will rust and corrode over time.

In 1913, Harry Brearley of Sheffield, UK, revolutionized the metallurgy of steels by discovering 'rustless steel' by adding 12.8 % chromium content to molten iron [39]. This steel was later renamed stainless steel (SS) as the steel was resistant to staining and corrosion. In the 1950s and 1960s, technological advancements enabled the economical production of large tonnages of SS [40]. In Finland, SS production started in Tornio in 1976 and has evolved into one of the leading SS production sites in the world [41].

Figure 3 explains the unique self-healing capability of SS through a process known as passivation. A thin protective oxide layer forms on its surface when exposed to oxygen. If the steel is scratched or damaged, the chromium in the alloy reacts with oxygen to reform this protective layer, preventing further corrosion [42].

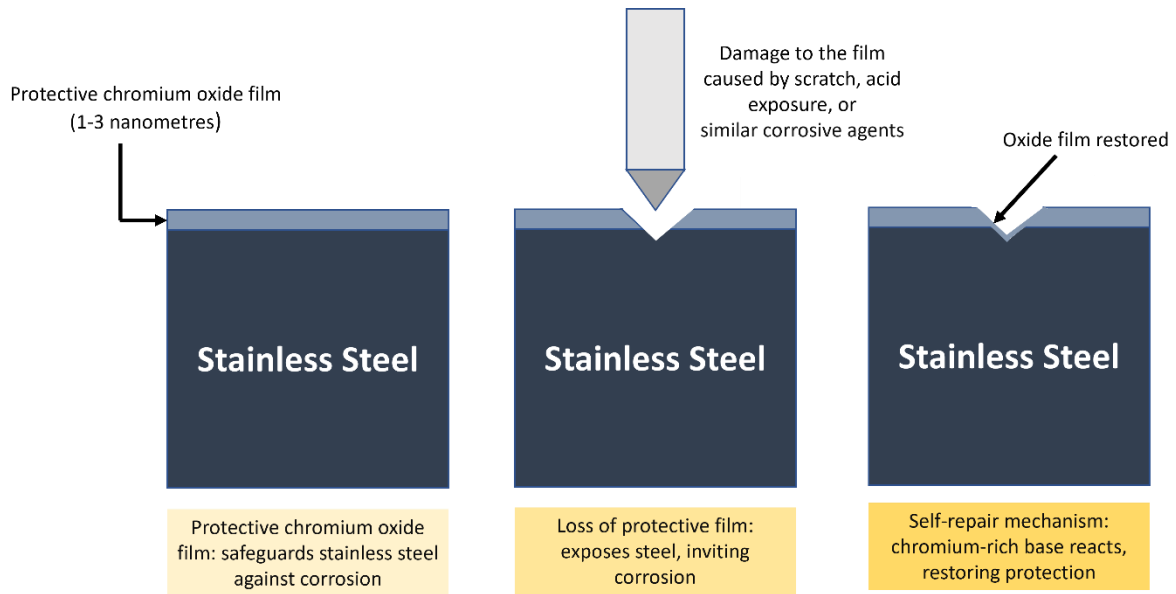


Figure 3. Stainless steel film dynamics: protective chromium oxide layer, vulnerability to damage, and self-repair mechanism.

In many applications, such as the oil and gas, food processing, and aerospace sectors, where the risk of corrosion is very high and unacceptable, this self-healing characteristic improves corrosion resistance and imparts longevity. Figure 4 depicts the percentage consumption of SS across different application categories.

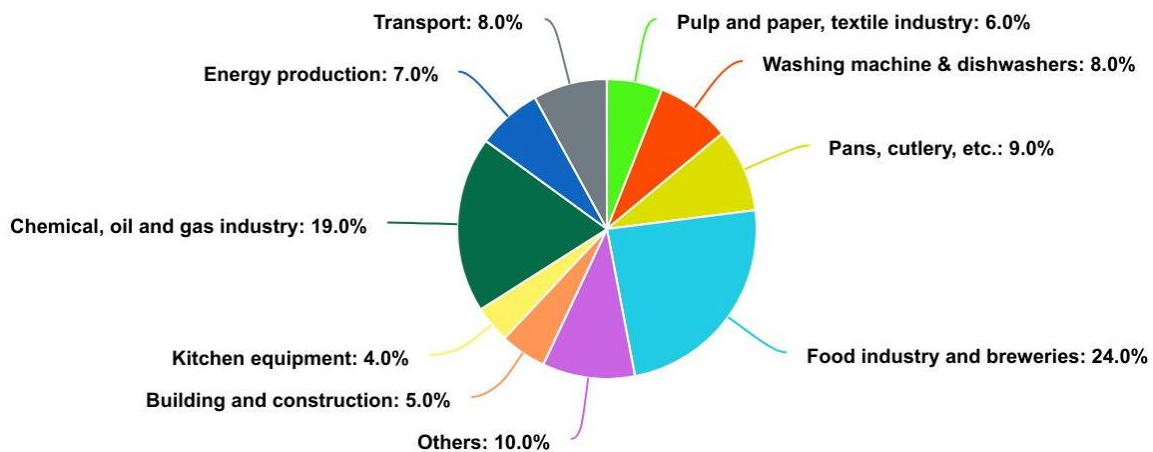


Figure 4. Application of stainless steel in various industries. Data collected from Ref. [41].

SS are classified according to the stable microstructure at room temperature. Austenite, ferrite, and martensite represent the existing phases under equilibrium conditions. Chromium contributes most to the corrosion resistance of SS by forming the passive layer and stabilizing the body-centered cubic (bcc) atomic structure, i.e., ferrite [43]. Other elements like silicon, aluminum, molybdenum, tungsten, niobium, and titanium promote the ferrite phase. The

austenite phase has a face-centered cubic (fcc) atomic structure and is stabilized by alloying elements such as nickel, manganese, carbon, and nitrogen [44]. To maintain an austenitic microstructure at room temperature, SS needs approximately 17 % chromium and 11 % nickel (or equivalents) [43]. The martensitic phase results from the diffusionless shear of austenite into a distorted cubic or hexagonal structure and is formed spontaneously during rapid cooling or can be induced isothermally through external deformation [45]. To have a martensitic phase in the microstructure, a minimum of 12 % chromium with 0.1 to 0.2 % carbon is required [46]. Due to high alloying elements in SS, some undesired intermetallic phases, such as sigma, laves, chi, etc., get precipitated and can coexist in the microstructure. Intermetallic phases impart an undesired hardness, brittleness, and localized corrosion vulnerability since they form along grain boundaries and deplete the remaining microstructure of alloying elements [47].

The Schaffeler-Delong diagram is usually used to predict the phases of an SS alloy upon welding or casting. This diagram considers various alloying elements' contributions to stabilizing the respective phases. Figure 5 explains how each alloying element affects the phases present in the microstructure. For 316L, the alloying elements, primarily nickel, and molybdenum, promote a fully austenitic microstructure, as demonstrated by its position in the Schaeffler Diagram, while for NiFDSS, nickel is substituted with nitrogen and high manganese, resulting in a duplex microstructure balancing ferrite and austenite phases.

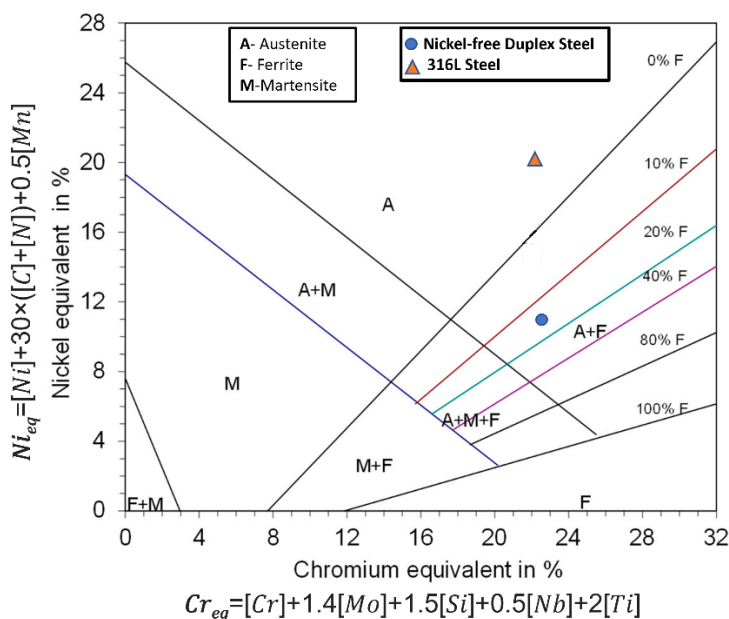


Figure 5. Schaeffler-Delong diagram highlighting the phases present in stainless steel grades depending upon the alloying compositions. Reproduced from Ref. [48] which is under an open-access Creative Common CC BY license

For any SS grades, if the elemental composition is known, it can be predicted whether it will have fully austenitic microstructure such as in 316L or duplex phase consisting of both austenite and ferrite in the matrix for NiFDSS in as-solidified cast or weld conditions at room temperature. ThermoCalc, a software package based on thermodynamic databases, can compute phase diagrams for a specific alloy, predicting the stability and volume fraction of various phases, including non-equilibrium phases such as intermetallics over a temperature range [49]. It simulates phase diagrams for particular alloys by integrating thermodynamic and kinetic models from diverse material databases. It can accurately represent the formation and evolution of intermetallic phases even in the presence of deviations from equilibrium conditions, as it incorporates kinetic models to account for non-equilibrium phase transformations.

The mechanical and corrosion-resistant properties of stainless steel depend upon the combined effect of the alloying elements. Chromium serves as the primary alloying element in SS, providing corrosion resistance. All stainless steels contain a minimum of 10.5 % chromium; the higher the chromium content, the more corrosion resistance will be [50]. Moreover, chromium enhances resistance to high-temperature oxidation of SS [51]. Nickel is added in SS to improve ductility and toughness. Adding molybdenum increases the resistance to uniform and localized corrosion while contributing to a moderate increase in mechanical strength [41]. However, it amplifies the susceptibility of SS to the formation of intermetallic phases in ferritic, duplex, and austenitic steel [52]. Manganese enhances the solubility of nitrogen, resulting in higher dissolution of nitrogen in duplex and austenitic SS. As an austenite-forming element, manganese can also substitute some of the nickel in SS compositions [53,54]. Carbon enhances mechanical strength but diminishes the resistance to intergranular corrosion arising from carbide formation. The addition of nitrogen increases the mechanical strength, and when combined with molybdenum, it enhances resistance to localized corrosion [55].

2.1 Austenitic stainless steel

Austenitic grades are the most popular and the largest group of SS. They are highly formable and weldable and can withstand temperatures ranging from cryogenic to the heat of furnaces and jet engines [56]. They retain strength at higher temperatures (above 500 °C) better than ferritic SS alloys and are creep-resistant [57]. Austenitic grades are widely used for their exceptional mechanical properties, such as high toughness and predictable corrosion

resistance, ranging from grades that can withstand common corrosive environments to those with higher corrosion resistance to withstand boiling seawater [43]. Adding chromium enhances oxidation and corrosion resistance, while nickel equivalents contribute to austenite stability.

ASS grades are used in a wide range of applications. They offer longevity, resistance to corrosion, and biocompatibility for surgical instruments and implants in medical applications. In the power generation and chemical processing industries, which demand higher oxidation and corrosion resistance, ASS is applied in steam turbines, boiler tubes, digesters, storage tanks, and heat exchangers [58]. ASS is suitable for high-stress, high-temperature, and life-critical components in aircraft and automobile industries [58].

Cr-Ni-Mo austenitic SS are categorized as 'general purpose grades.' They exhibit enhanced corrosion resistance due to the addition of molybdenum (2-3 %) [41]. Often labeled as "acid-proof" stainless steels, they have a chromium content of approximately 17% and nickel content ranging from 10% to 13% [59]. 316L grade SS falls under this category. The letter 'L' represents the low carbon content (<0.03 %). The removal of carbon is primarily done to enhance the corrosion resistance of the alloy, especially in environments where sensitization and carbide precipitation on grain boundaries can occur [60]. Minimizing carbon content reduces the susceptibility to intergranular corrosion, making 316L stainless steel well-suited for applications in corrosive environments, such as marine and chemical settings. Figure 6 outlines the primary areas of application for 316L SS.

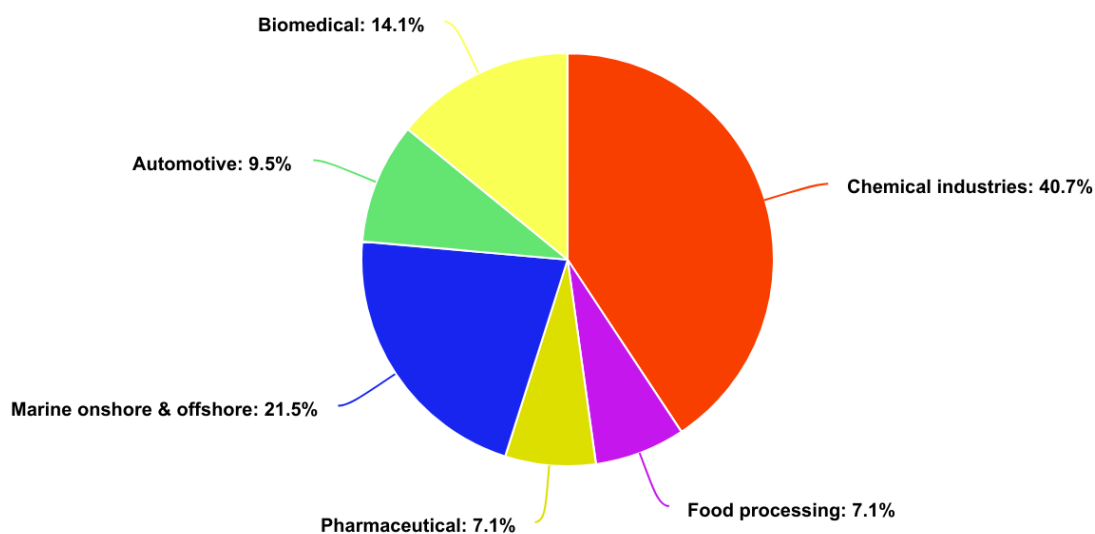


Figure 6. Applications of 316L SS across various industries. Reproduced and modified from Ref. [24] which is under an open-access Creative Common CC BY license

The major challenge in using ASS is its higher cost than carbon steel or ferritic grades [50]. The fluctuation in nickel prices further augments this cost aspect. The inability to undergo heat treatment for hardening limits their applications, and the need for annealing to reduce magnetic sensitivity adds more complexity to their manufacturing processes [61]. Moreover, these alloys are prone to adhesive wear [58]. In high chloride environments, chloride-induced stress corrosion can lead to cracking and pitting, causing premature failure of components like fuel tanks in wet-area marine applications [58].

2.2 Duplex stainless steel

DSS grades represent the latest and most rapidly expanding alloy category within the SS family. Discovered in the 1920s, DSS was not extensively utilized until the 1980s, when there was an increased demand from the chemical industry [43]. These grades exhibit a ferritic-austenitic microstructure, maintaining an approximate 50% balance between both phases. They amalgamate advantageous properties from both ferritic and austenitic SS. They have a higher chromium content (20.1-25.4 %) and a relatively low nickel content (1.4-7 %) compared to austenitic grades, which leads to better price stability [41]. Adding molybdenum (0.3-4 %) and nitrogen (0.15- 0.4 %) improves corrosion resistance. Manganese is incorporated in certain grades to replace nickel and enhance nitrogen solubility in the material. They have higher yield strength than ASS and a higher impact toughness than ferritic steels [62]. Additionally, they are less prone to hydrogen embrittlement than ferritic steels and provide better thermal conductivity than ASS [63]. DSS offers enhanced corrosion resistance due to the balanced contribution of both phases [64]. The ferrite phase is richer in chromium and molybdenum, showing superior corrosion resistance. However, adding nitrogen improves the corrosion resistance of the austenite phase, matching that of the ferrite. This balanced microstructure allows DSS to outperform austenitic grades in aggressive environments [43].

However, DSS is more susceptible to embrittlement from carbides, nitrides, and intermetallic phases in the temperature range of 700 to 955 °C [65]. The formation of sigma and chi phases reduces the corrosion resistance and mechanical properties [64]. The risk of sigma phase formation increases with higher chromium, molybdenum, and tungsten content. To solve this issue, DSS is solutionized at 900-1100 °C and quenched to prevent the precipitation of intermetallic phases, resulting in uniform distribution of alloying elements such as chromium, molybdenum, and nitrogen across both the ferritic and austenitic phases [66].

DSS are suited for marine and harsh industrial environments due to their high resistance to chloride-induced stress corrosion cracking [67]. The oil and gas industry represents another sector where DSS is used. The chemical processing industry is also shifting to duplex stainless steel for various applications such as heat exchangers, pressure vessels, tanks, columns, pumps, valves, and shafting [63].

DSS are classified into five categories according to their PREN values: lean duplex with $\text{PREN} \leq 30$, molybdenum-containing lean duplex with $30 < \text{PREN} \leq 33$, standard duplex with $33 < \text{PREN} < 40$, super duplex with $40 < \text{PREN} < 50$ and hyper duplex with $\text{PREN} \geq 50$ [67]. Lean duplex stainless steels have low levels of nickel and molybdenum. Nickel is substituted by nitrogen and manganese to achieve a balanced combination of austenite and ferrite [68]. This category offers an alternative to 316L and another austenitic grade for structural applications, tank construction, and environments requiring resistance to chloride stress corrosion cracking since they possess similar corrosion resistance, better mechanical properties, and material savings [64]. Standard DSS grades such as S2205 are the workhorse grades in various applications. Super and hyper DSS are used for extremely corrosive environments.

3 Laser powder bed fusion of metals

Laser powder bed fusion of metals (PBF-LB/M) is an AM route that utilizes a guided laser beam to selectively melt metal powders layer-by-layer in an inert atmosphere and facilitates the production of intricately designed metal components. PBF-LB/M has gained significant industrial interest since its advent in the 1990s due to its unparalleled precision, minimal surface waviness, ability to achieve near 100% relative densities, versatility in producing intricate and complex structures, and efficacy in reducing oxide impurities while production due to presence of inert atmosphere which is crucial to preserve corrosion and fatigue resistance in metal alloys since oxides can act as crack initiators [69].

Figure 7 describes the workflow of PBF-LB/M, which is divided into five stages. The first stage is creating a design file based on the specific needs of the manufacturer using software such as AutoCAD, Solidworks, or Fusion360. Supports are sometimes incorporated into the design, especially with more than 45-degree overhangs. This addition ensures structural integrity during the printing process, preventing deformities or collapses caused by unsupported areas and preventing heat from accumulating. In the second stage, the design is converted into the .STL file format, representing 3D surface geometry using connected triangles, which is compatible with AM equipment [70]. Finally, dedicated software such as Autodesk Netfabb is used to slice the .STL file into layers that gives laser path definition for layer-by-layer fabrication. The sliced file is saved in a format compatible with the PBF-LB/M equipment. For example, the Aconity MIDI+, a PBF-LB/M printer, accepts the .ILT format for printing the parts.

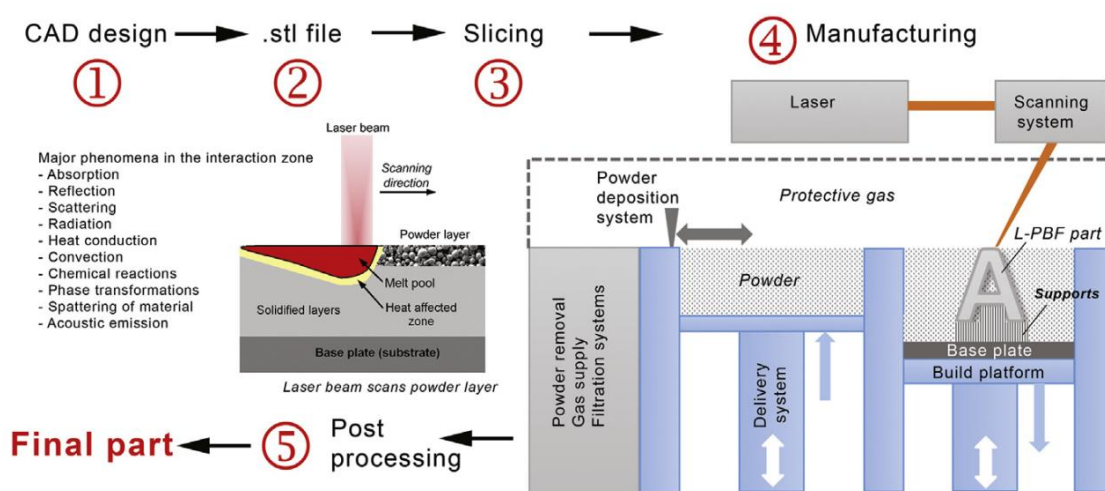


Figure 7. Schematic diagram explaining various stages involved in PBF/LB-M. Reproduced from Ref. [71] which is under the licence of CC BY 4.0

In the fourth stage, the manufacturing process starts with placing metal powders within the powder-bed space, the quantity being dependent on the height of the part. A build plate is positioned to serve as the base for printing and act as a reservoir of accumulated heat. Subsequently, an inert gas such as argon or nitrogen gas is purged into the printer chamber to establish an oxygen level below 1000 parts per million (ppm) because oxygen can lead to the formation of metal oxides, which is detrimental to the mechanical properties of the as-built part. The fabrication procedure initiates with the elevation of the powder bed, followed by the recoater distributing a thin layer of powder onto the build plate. The laser then selectively scans the area, melting the powder particles to solidify into the desired shape. The build plate descends, enabling the deposition of a new layer, and this iterative process continues until the entire component is fabricated. In the final stage, post-processing begins by removing the metal parts from the build plate. These components may undergo additional treatments, such as heat treatment, surface finishing, or machining, tailored to specific requirements decided by the end-use application.

During PBF-LB/M, when the laser interacts with the metal powder, a series of complex physical phenomena unfold, including absorption and reflection of laser energy, alongside forming a melt pool [72]. As the molten metal solidifies through heat conduction and convection, non-equilibrium phase transformations occur due to rapid cooling rates, often accompanied by undesired spattering of molten metal particles from the melt pool. Many ongoing research studies focus on integrating acoustic and thermal sensors to enhance process understanding and control during PBF-LB/M, though detailed exploration is beyond the scope of this thesis [73–75].

Figure 8 categorizes the key parameters involved in PBF-LB/M into four main groups: powder material-based input parameters, machine-based input parameters, manufacturing process parameters, and post-treatment parameters. Metal powders used in PBF-LB/M are generally produced via gas atomization [76]. In this process, a high-pressure inert gas like nitrogen or argon atomizes a stream of molten metal into small droplets. During free fall, the droplets solidify at a very high cooling rate and form round spherical powder particles. The gas atomization process enables precise control over powder morphology and size distribution. Each of the sub-properties of powder used during the printing holds critical importance. Powder morphology and size distribution determine powder flowability and packing density [77]. Thermal and optical properties influence energy absorption and reflectivity during laser interaction. Metallurgical properties dictate microstructure formation,

and rheological properties decide powder flow behavior and layer formation during printing [78].

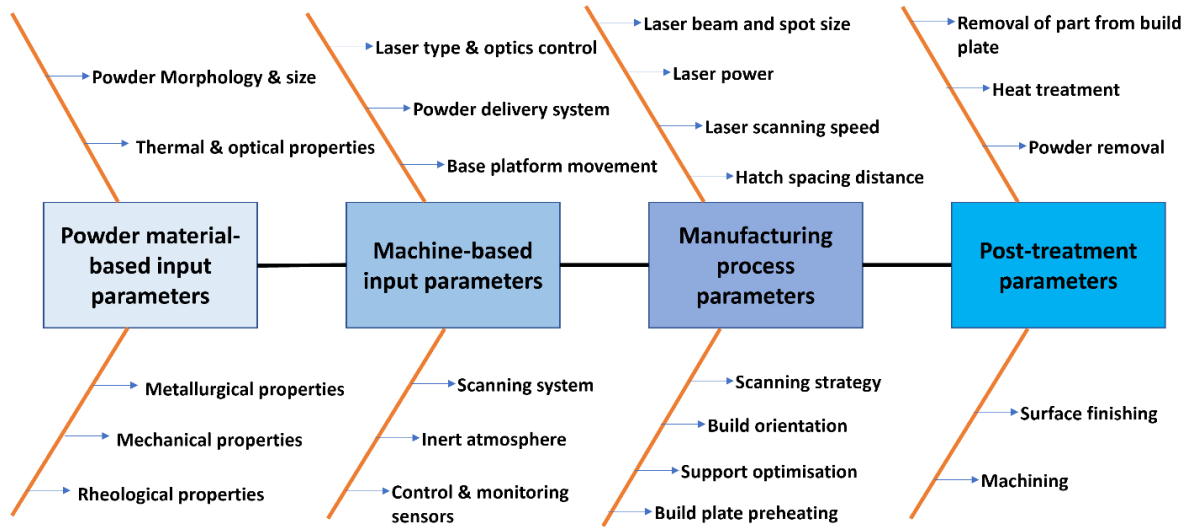


Figure 8. Key parameters impacting the quality of PBF-LB-built components. Reproduced and modified from Ref. [71], which is under the licence of CC-BY 4.0.

In machine-based input parameters, several sub-categories decide the efficacy and precision of the PBF-LB/M process [71]. Laser type and optics control govern the characteristics and modulation of the laser beam. The powder delivery system ensures uniform deposition of powder layers onto the build platform, while base platform movement controls the positioning and movement of the build platform. The scanning system directs the laser beam across the powder bed, resulting in precise melting and solidification of each layer. Inert atmosphere maintenance within the printing chamber safeguards against the oxidation of metal. Control and monitoring sensors offer real-time feedback during manufacturing, facilitating data storage for in-depth analysis and refinement of process parameters, enhancing efficiency and quality control.

Figure 9 highlights the manufacturing process parameters that must be optimized for each metal alloy [79]. Laser beam and spot size dictate the diameter and intensity distribution of the laser beam, influencing the resolution and accuracy of the printed part. Laser power determines the energy delivered (in Joules) to melt the powder per second. Laser scanning speed governs the rate at which the laser traverses the powder bed, thereby determining the melting efficiency and overall build rate. Hatch spacing distance, another essential parameter, defines the separation between adjacent laser scan paths, affecting surface finish and part density. Moreover, layer thickness serves as a fundamental parameter, determining the height

of each deposited layer and thus influencing part resolution, build time, and mechanical properties.

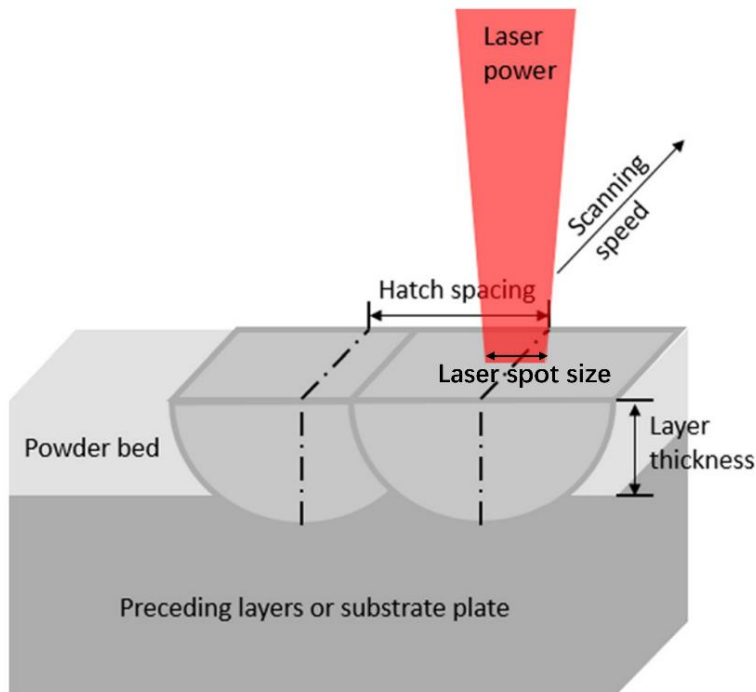


Figure 9. Manufacturing process parameters in PBF-LB/M. Reproduced from Ref. [79], which is under the licence of CC-BY 4.0.

Laser energy density (LED) is a metric in PBF-LB/M, defined as the ratio of laser power to the product of scanning speed, hatch distance, and layer thickness, i.e.,

$$LED (J/mm^3) = \frac{Power (W)}{Scanning\ speed \left(\frac{mm}{s}\right) \times hatch\ distance (mm) \times layer\ thickness (mm)} \quad (2)$$

It serves as a parameter in assessing the quality of fabricated parts. A higher LED than the optimal value often leads to spattering, over-melting, and residual stress within the printed parts, which occurs because the excessive energy input can cause the material to vaporize and splatter, leading to irregularities in the printed layers. Additionally, over-melting can occur, resulting in poor surface finish and reduced mechanical properties. Due to excess heat, there is a chance of residual stress trapped inside as-built parts. Conversely, a lower LED can result in problems like delamination, voids, and partial melting of the powder. This occurs because insufficient LED may not fully fuse the powder particles, leading to poor adhesion between layers and causing delamination. Also, inadequate energy input can result in voids within the printed part, compromising its structural integrity. Therefore, maintaining the LED within the appropriate range is essential for achieving optimal part quality.

Figure 10 illustrates the correlation between PBF-LB/M parts and LED. It demonstrates how variations in LED impact part quality, showcasing delamination in PBF-LB/Med NiFDSS samples manufactured for this thesis study with lower LED (Figure 10 (b)) and crack-free samples produced using optimal parameters (Figure 10 (c)). Figure 10 (d) shows over-melted and distorted samples manufactured with higher LED, particularly evident in the area closer to the build plate, where the sample appears burnt, caused by excessive heat accumulation.

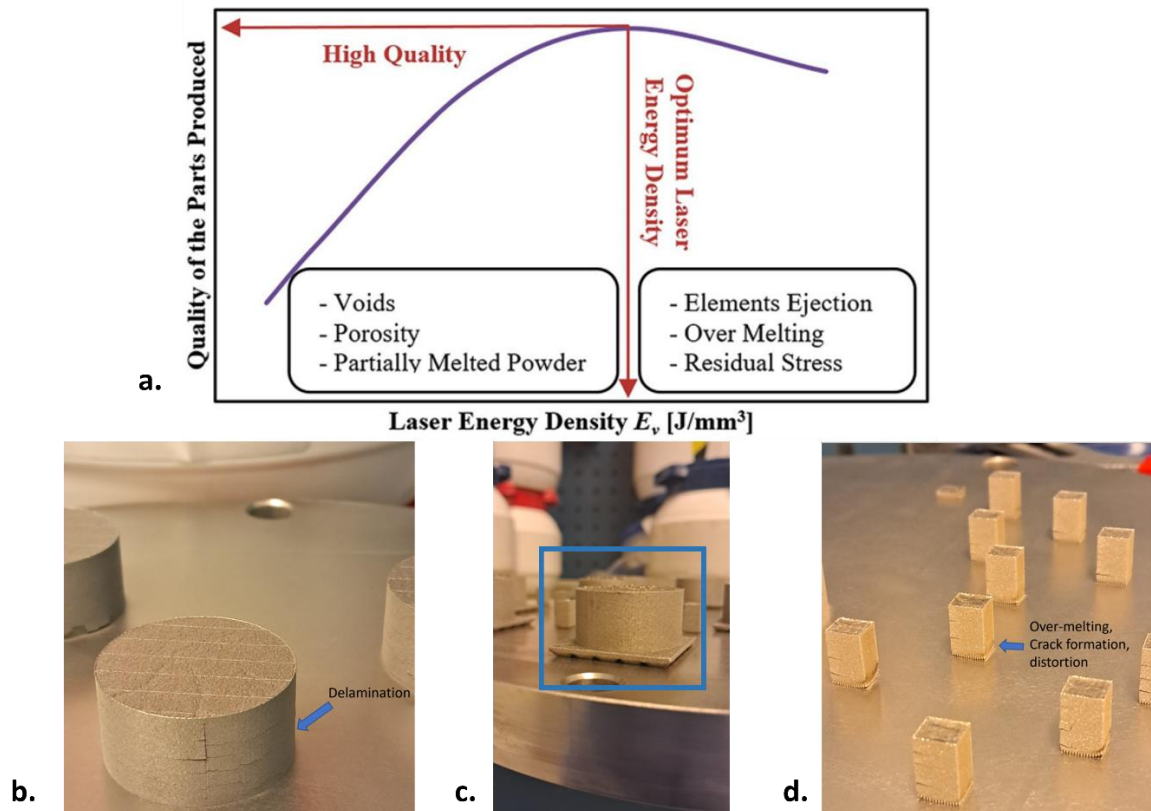


Figure 10. (a) Correlation between PBF-LB/M parts and laser energy density (LED). Reproduced from Ref. [80] which is under the licence of CC-BY 4.0., (b) Delamination observed in NiFDSS samples with lower LED, (c) Crack-free samples produced using optimal parameters, (d) Over-melted and distorted samples manufactured with higher LED.

In addition to these primary parameters, other important considerations include scanning strategy, which decides the path followed by the laser during part fabrication [81]. The user defines the scanning path via software such as Autodesk Netfabb. An angled transition between layers is introduced by rotating the laser scanning direction to avoid stress build-up during printing [82]. Build orientation specifies the part orientation relative to the build platform. Furthermore, support optimization involves strategically designing and placing supports to ensure part stability during printing and to conduct the heat away. Build plate preheating involves heating the build plate to a specified temperature before printing to reduce residual stresses in the final printed component [83].

3.1 PBF-LB of 316 L

Research on PBF-LB/M of austenitic stainless steels has predominantly focused on 316L SS, with some limited studies on 304L SS grade [84]. The emphasis on 316L can be attributed to its widespread use in various industries due to its excellent corrosion resistance, mechanical properties, and biocompatibility. Relative density, in the context of PBF-LB/M, refers to the ratio of the actual density of a printed component to the theoretical density of the material being used. In 2010, Tolosa et al. attained a relative density of 99.9 % in PBF-LB/M manufactured 316L SS. This was achieved using a 200 W laser with an 80 μm laser spot diameter and a scan velocity reaching 1000 mm/s [85]. Following this study, various research papers have documented the PBF-LB/M of 316L SS, consistently achieving relative densities around 99.99 % [86–90].

Figure 11 illustrates the solidification behavior of ASS, which is primarily governed by the equivalent ratio of chromium equivalent to nickel equivalent ($\text{Cr}_{\text{eq}}/\text{Ni}_{\text{eq}}$).

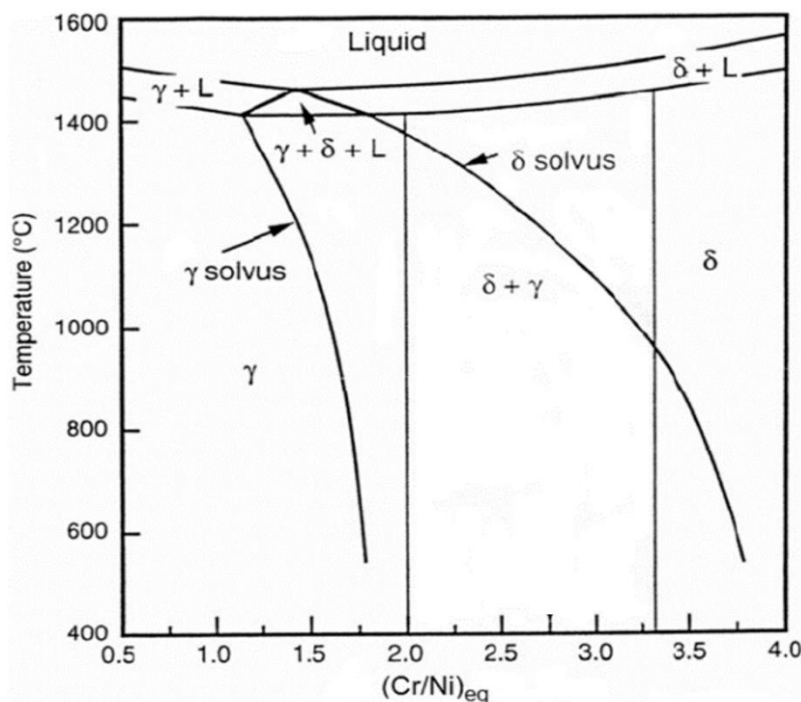


Figure 11. Solidification behavior of stainless steels depending on $\text{Cr}_{\text{eq}}/\text{Ni}_{\text{eq}}$. Reproduced from Ref. [91], which is under an open-access Creative Common CC BY license.

Depending on the $\text{Cr}_{\text{eq}}/\text{Ni}_{\text{eq}}$ ratio, different solidification modes are observed [91,92]:

- A mode ($L \rightarrow L + \gamma \rightarrow \gamma$) occurs when $\text{Cr}_{\text{eq}}/\text{Ni}_{\text{eq}} < 1.25$.
- AF mode ($L \rightarrow L + \gamma \rightarrow L + \gamma + \delta \rightarrow \gamma + \delta \rightarrow \gamma$) is observed when $1.25 < \text{Cr}_{\text{eq}}/\text{Ni}_{\text{eq}} < 1.48$.

- FA mode ($L \rightarrow L + \delta \rightarrow L + \delta + \gamma \rightarrow \delta + \gamma \rightarrow \gamma$) is characterized by $1.48 < Cr_{eq}/Ni_{eq} < 1.95$.
- F mode ($L \rightarrow L + \delta \rightarrow \delta \rightarrow \delta + \gamma \rightarrow \gamma$) occurs when $Cr_{eq}/Ni_{eq} > 1.95$

Where L represents liquid, δ represents ferrite (F), and γ represents austenite (A). For 316L grades, the Cr_{eq}/Ni_{eq} ratio typically falls within the range of 1.25-1.95, leading to either AF or FA solidification modes [93]. These modes favor the development of a fully austenitic matrix, irrespective of the manufacturing method, whether it be PBF-LB/M, casting, or welding [92].

Figure 12 provides the material characterization of as-built PBF-LB/M 316L samples. The SEM image reveals a complex cellular microstructure with fine sub-grains, typical of samples synthesized via PBF-LB/M, indicating rapid solidification. EBSD imaging shows a fully austenitic phase marked in red, proving the presence of a single austenitic phase in the samples. Additionally, XRD mapping of gas-atomized powder and as-built samples confirms the presence of only austenite phases in both cases.

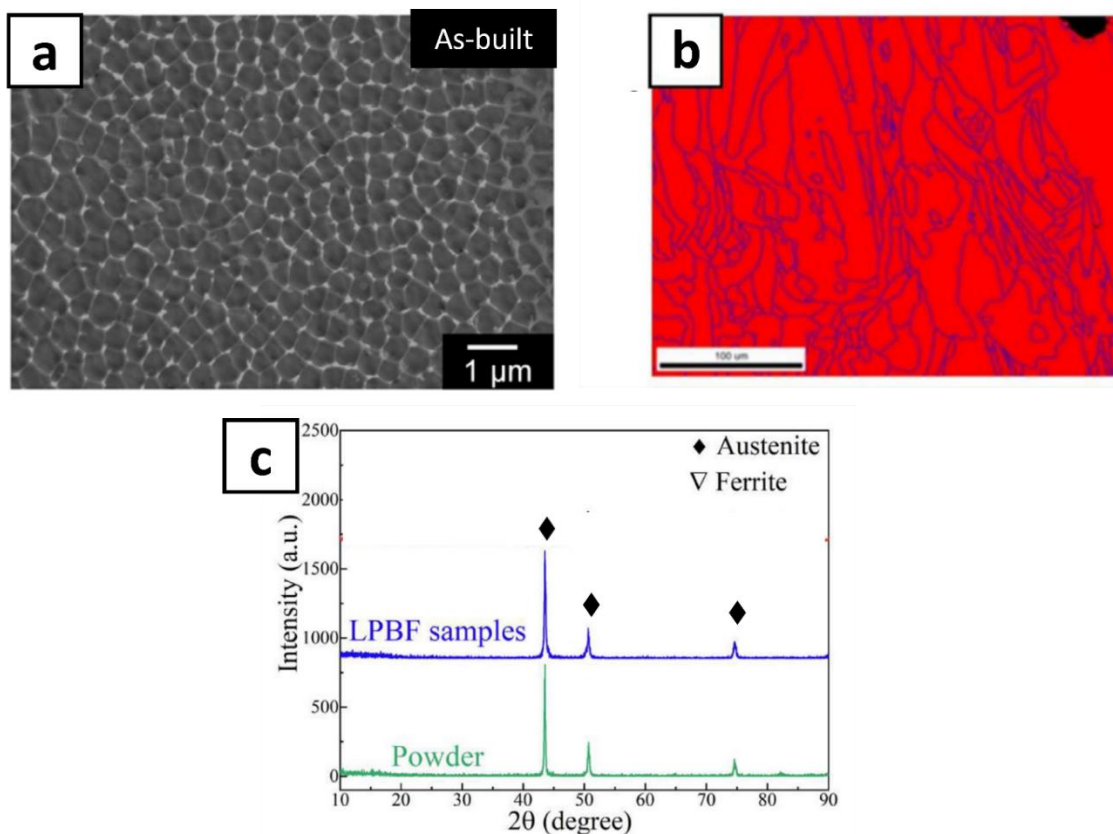


Figure 12. As-built PBF-LB/M 316L samples (a) SEM image showing cellular microstructure, (b) EBSD imaging showing fully austenitic phase (marked as red), (c) XRD mapping of powder and as-built samples showing only austenite peaks in both cases. Reproduced from Ref. [94], which is under the licence of CC-BY 4.0. Reproduced from Ref. [95,96] which is under an open-access Creative Common CC BY license

PBF-LB/M has demonstrated its capability to fabricate 316L stainless steel with mechanical properties surpassing its traditional wrought/cast counterparts [11]. As-built 316L samples have an ultimate tensile strength ranging from 650 to 700 MPa, notably higher than the 450 to 550 MPa range observed in conventional methods [97]. Similarly, the samples have a yield strength between 450 to 600 MPa, exceeding the 160 to 370 MPa range found in traditional manufacturing [97]. Moreover, PBF-LB/Med 316L steel maintains good ductility, with elongation values ranging from 35 to 60 %, compared to the 30 to 45 % range in conventionally manufactured parts [98]. This combination of strength and ductility represents the advantage of PBF-LB/M, offering a promising solution to the long-standing challenge of balancing strength and ductility in conventional manufacturing processes.

Salman et al. studied the effect of annealing heat treatment on the mechanical behavior and phase composition of PBF-LB/Med 316L SS samples [94]. Figure 13 (a) illustrates the effect of annealing on the stress-strain curve. The optimal balance of strength and ductility is achieved during the as-built condition, with subsequent heat treatments not enhancing the performance of the material. The lack of improvement is caused by decreased strength not compensated by a corresponding increase in plastic deformation. Figure 13 (b) presents XRD patterns for the as-built specimens and those subjected to annealing at various temperatures for 6 hours. The peaks indicate the formation of single-phase austenite in all specimens, regardless of heat treatment. Moreover, negligible differences in peak intensities are observed between the as-built and heat-treated samples, suggesting minimal changes in the phase composition after annealing.

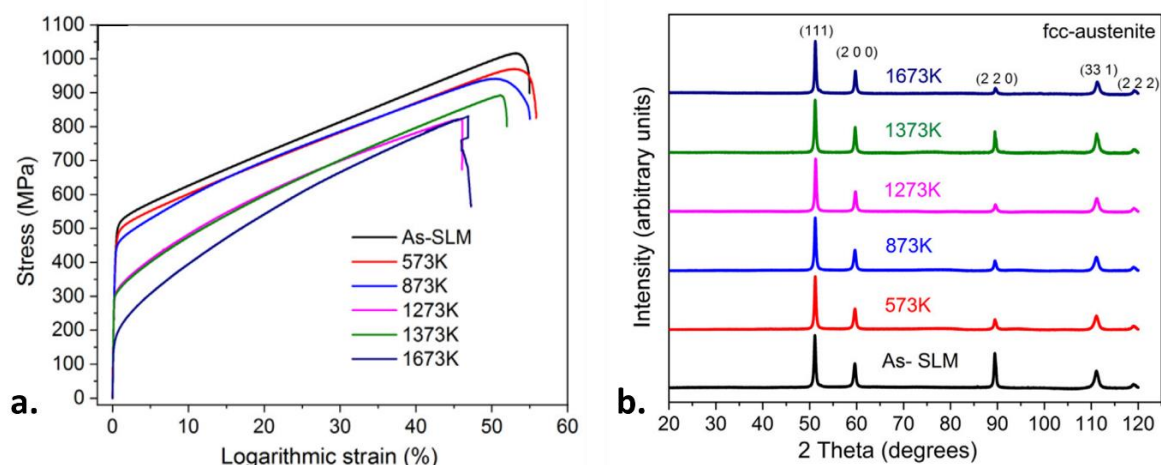


Figure 13. Tensile stress-strain curves for as-built PBF-LB/Med samples and specimens subjected to annealing at different temperatures (b) XRD patterns illustrating austenite phases in as-built samples and samples heat-treated at varying temperatures. Reproduced from Ref. [94] which is under the licence of CC-BY 4.0.

3.2 PBF-LB of duplex stainless steel

DSS has gained popularity over the past few decades across various industries, including chemical and marine engineering, owing to its superior strength and corrosion resistance compared to austenitic SS. Among the most extensively studied grades, 2507 and 2205 grades are the primary research focus, given their widespread industrial applications. Conventionally produced duplex SS through casting and welding have a nearly equal proportion of ferrite and austenite phases after solidification. Since, the Cr_{eq}/Ni_{eq} for DSS is higher than 1.95, the solidification sequence for DSS is $L \rightarrow L+\delta \rightarrow \delta \rightarrow \delta+\gamma$, where L, δ , and γ represent liquid, ferrite, and austenite, respectively [92].

However, the PBF-LB/M manufactured DSS has a primarily ferritic microstructure with minimal austenite and nitride phase formation at the grain boundaries [84]. In contrast to welding processes with power outputs ranging from 1 to 50 kW and conventional casting processes with cooling rates on the order of 10^2 K/s, the PBF-LB/M operates at much lower powers, often below 0.5 kW, resulting in a higher cooling rate of approximately 10^6 K/s [92]. This rapid cooling inhibits the transformation from δ -ferrite to austenite during PBF-LB/M, necessitating post-heat treatment to form the dual-phase structure in duplex SS samples.

The EBSD phase map depicted in Figure 14 illustrates the phase composition of the as-built PBF-LB/Mod Fe-22Cr-5Ni-0.26N DSS grade and the austenite appearance after the heat treatment [99]. After optimizing the process parameters, specimens were printed with a laser power of 100 W, scan speed of 700 mm/s, hatch spacing of 60 mm, and layer thickness of 30 mm, achieving a relative density of 98.78 %. Then, the samples were kept at 1000 °C, 1100 °C, and 1200 °C for 1 hour, followed by quenching in water. Since ferrite is the initial microstructure in the as-built specimen, austenite nucleation occurs from the ferrite phase. The volume fraction of austenite is observed to increase, reaching 60.3 vol% when heat treated at 1000°C. However, the austenite volume fraction gradually decreases with increasing temperature, reaching 56.6 vol. % at 1200 °C. This suggests a strong dependence of ferrite and austenite phase fractions on heat treatment temperature. XRD peaks gave similar results as the powder and as-built samples have only ferritic peaks, while after heat treatment, both austenitic and ferritic peaks are observed.

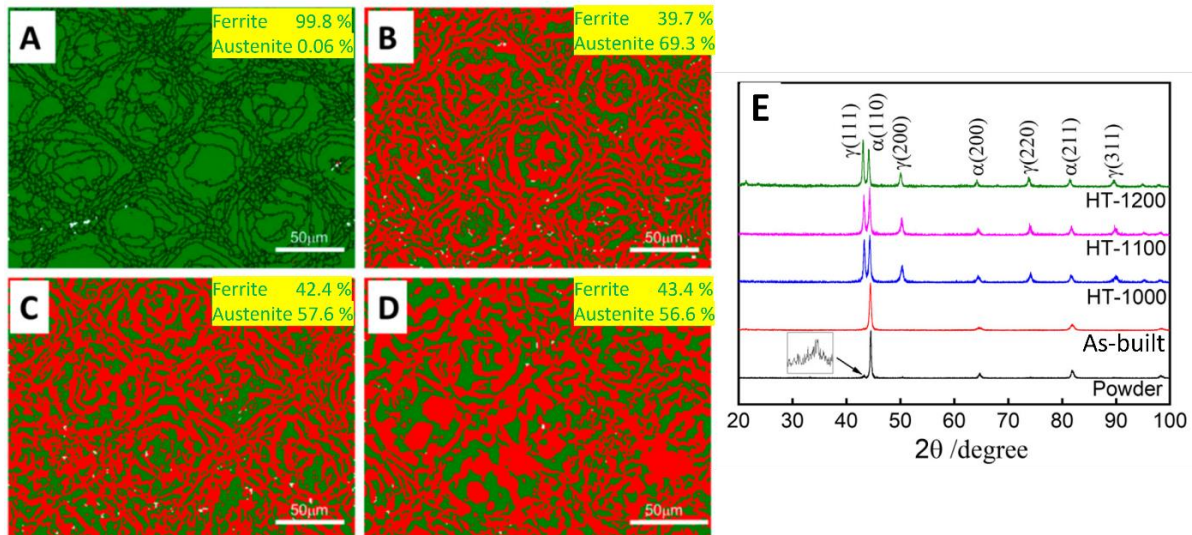


Figure 14. Phase maps obtained through EBSD analysis of the specimens: (a) as-built duplex SS, (b) heat treated at 1000 °C, (c) at 1100°C, (d) at 1200 °C, (e) XRD patterns obtained from powder and different specimens (α -ferrite, γ -austenite). Reproduced from Ref. [99] which is under an open-access Creative Common CC BY license.

Florian et al. studied the effect of heat treatment on the mechanical behavior of PBF-LB/Med 2205 DSS grade [100]. As shown in Figure 15, the as-built sample, having an almost entirely ferritic microstructure, exhibits a higher ultimate strength, reaching 940 MPa, with a very low elongation at a fracture of 12%. After heat treatment in the 1000-1200 °C range for 5 minutes, followed by water quenching, the specimens undergo complete recrystallization, resulting in ultimate strength ranging from 720 MPa to 770 MPa. This transformation is accompanied by the appearance of austenite in the matrix, resulting in a duplex microstructure and improving ductility. Therefore, heat treatment is essential for improving the mechanical properties of DSS produced via PBF-LB/M, transitioning them from predominantly ferritic to duplex microstructures.

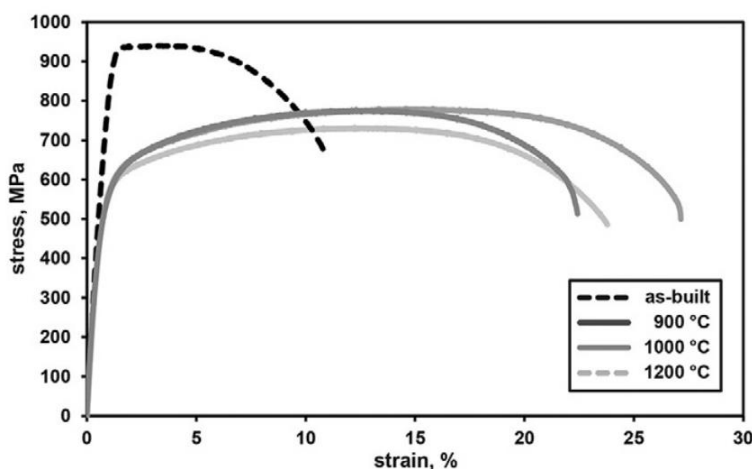


Figure 15. Tensile stress-strain curves of PBF-LB/Med 2205 duplex SS in as-built and heat-treated conditions. Reproduced from Ref. [100], which is under the licence of CC-BY 4.0.

3.2.1 PBF-LB/M of NiFDSS

Only two studies have been reported on PBF-LB/M of NiFDSS. Tuomas et al. conducted a design of experiment for process parameter optimization for fabricating NiFDSS, having laser power ranging from 110 W to 300 W in increments of 20 W, scanning velocity varied from 400 mm/s to 2000 mm/s in steps of 400 mm/s, and hatch distance ranged from 0.05 mm to 0.08 mm with steps of 0.01 mm [27]. The layer thickness remained constant throughout the experiments at 30 μm , and the laser beam diameter was maintained at 80 μm . A relative density of 98.542 % was achieved at a laser power of 110 W, while it was 98.469 % at a laser power of 160 W with a scanning speed of 600 mm/s and hatch distance of 0.08 mm. Similar to the previous study on PBF-LB/M of DSS, a fully ferritic microstructure was obtained in as-built samples. After heat treatment at 900 °C for 0.5 hrs followed by quenching, a 52% austenitic phase was observed in the sample with 110 W laser power.

Following this study, Chinmayee et al. did another comprehensive research on evaluating and comparing the wear behavior of NiFDSS and 316L, manufactured via PBF-LB/M, in a simulated body fluid environment for biomedical applications [28]. The study concluded that NiFDSS has slightly better wear resistance and is more biocompatible than 316L in the human body environment. Building upon these two studies as the foundation, further process parameter optimization was done in this thesis, which is discussed in more detail in Section 7.3.2.

4 Introduction to tribocorrosion

4.1 Principles of tribology

Tribology is a field dedicated to understanding wear, friction, and lubrication when components are subjected to loading and movement against one another [101]. The term "tribology" was coined in 1996 and originated from the Greek word "tribos" which means rubbing [101]. Frictional resistance is experienced at the contact points during relative motion between two bodies. Wear is defined as the gradual loss of material due to these interactions between contacting surfaces during relative motion, and it presents a challenge in various engineering applications, frequently leading to the failure of components and ultimately requiring repair or replacement [102]. Tribological interactions contribute to 23 % of worldwide energy consumption, with friction accounting for 20 % and the remaining 3 % on remanufacturing worn parts and equipment due to wear-related failures [103]. A better understanding of tribology for reducing friction and protecting against wear in industrial equipment can lead to considerable savings in energy and avoid component failure. The factors influencing friction and wear between interacting surfaces in relative motion are called tribological systems.

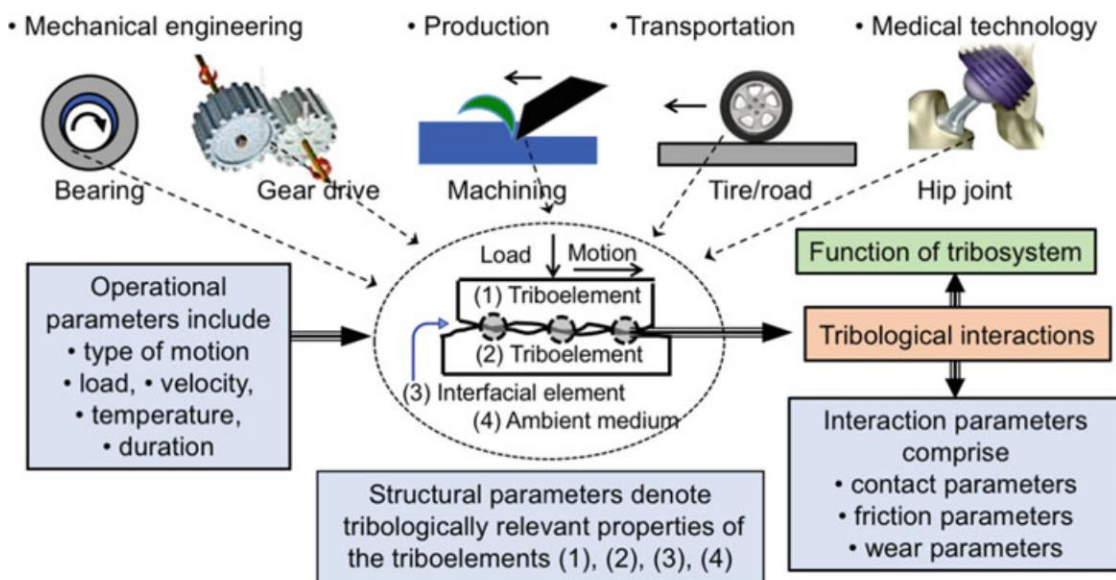


Figure 16. Examples of tribological systems and various tribological parameters influencing the wear and friction. Reproduced from Ref. [103], which is under the licence of CC-BY 4.0.

As shown in Figure 16, different tribological systems exist across various domains, such as bearings, gear drives, machining tools, tires/roads, and hip joints. Tribological parameters have been classified into three main groups [103]. The first one is operational parameters,

which include factors related to how the tribological system operates, including the type of motion it undergoes, the amount of weight or load acted upon, how fast it moves, the temperature it operates at, and how long it operates. Structural parameters are based on the materials used to fabricate the components (triboelements), the environmental conditions under which they operate, and the lubricating medium. Interaction parameters focus on how the surfaces interact and cover details like how the surfaces come into contact, the friction they generate, and how much material is worn away during their interaction.

A tribometer is used to simulate real-world tribological systems in laboratory settings. This device determines tribological properties like the coefficient of friction (CoF), friction force, and wear volume between two surfaces in contact. Figure 17 explains the working principle of a ball-on-disc tribometer. In this setup, a normal load (F_n) is applied by a hanging mass opposite the study sample via strings and pulleys. A ceramic ball holder makes contact with the sample and is called a counterbody. When the apparatus is rotated, wear tracks are formed due to the relative motion between the ceramic ball and the sample. The user defines the wear track radius (R) and the operation time. The lubricating medium can be chosen based on the application. A tribometer is equipped with various sensors like strain gauges, piezoelectric sensors, wear sensors, etc., that allow the real-time calculation of wear, CoF , and frictional force [103]. CoF is the ratio of frictional force (F_f) experienced by the ball divided by the F_n . Once the test run is completed, total wear volume or depth can be evaluated using confocal microscopy. Wear rate, defined by wear volume divided by normal force and total sliding distance, is often used to compare the wear resistance of two different materials. This has been summarised in Table 1.

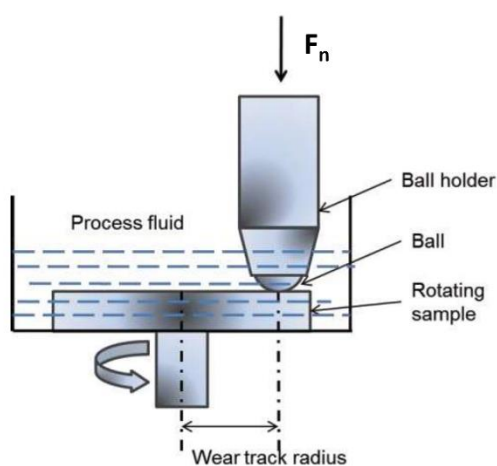


Figure 17. Schematic diagram of a ball-on-disc tribometer. Reproduced from Ref. [104] which is under an open-access Creative Common CC BY license.

Table 1. Analysis of various tribological properties: calculations and formulas

Tribological properties	Evaluation	Formula
Frictional force (F_f)	Tribometer	$F_f = CoF \times F_n$
Coefficient of Friction (CoF)	Tribometer	$CoF = \frac{F_f}{F_n}$
Wear depth (W_d)	Tribometer / Confocal microscope	-
Wear volume (W_v)	Confocal microscope	-
Sliding distance (D)	-	$D = RPM \times 2\pi R \times time$
Wear rate (W_r)	-	$W_r = \frac{W_v}{D \times F_n}$

Wear mechanisms are categorized into four main groups: abrasive, adhesive, fatigue, and corrosive wear, as shown in Figure 18 [102]. Adhesive wear arises from interactions between surfaces and asperity bonding during sliding contact. When the bonding strength at the contact point surpasses that of the bulk material, weaker material may detach and transfer to the counter body. As a result, one surface experiences material loss, forming irregular holes or pits, while the counter surface gains material in the form of a transfer film. Metals, especially those lacking oxide formation, are particularly prone to adhesive wear. Moreover, material toughness plays a crucial role, as materials prone to deformation readily adhere to each other, forming a larger contacting surface where bonding occurs during sliding. Fatigue wear occurs when repeated stress cycles lead to gradual damage on a surface, resulting in surface deformation or fracture over time. Corrosive wear happens when chemical reactions alongside mechanical wear degrade a surface, leading to material loss and part failure [105].

Abrasive wear results in high wear rates and involves multiple indentations of hard asperities from the counter body into a softer material, commonly associated with sliding hard particles over a smoother surface, resulting in damage through plastic deformation at the interface [102]. These hard particles can originate from processing, hard inclusions, or reaction products formed during sliding. Abrasive wear exists in two primary forms: cutting mode, where wear debris in the form of chips is produced, and plowing, which leaves grooves in the softer material. Such abrasive action is prevalent in materials exhibiting non-brittle behavior, like most metals, but can also occur in multiphase materials with soft matrices embedding

hard phases. Abrasive wear can be classified as two-body or three-body wear, depending on the number of interacting bodies involved in the abrasion process. Two-body abrasion occurs in mechanical operations like grinding and cutting, while three-body abrasion involves hard abrasive particles acting as interfacial third-body elements.

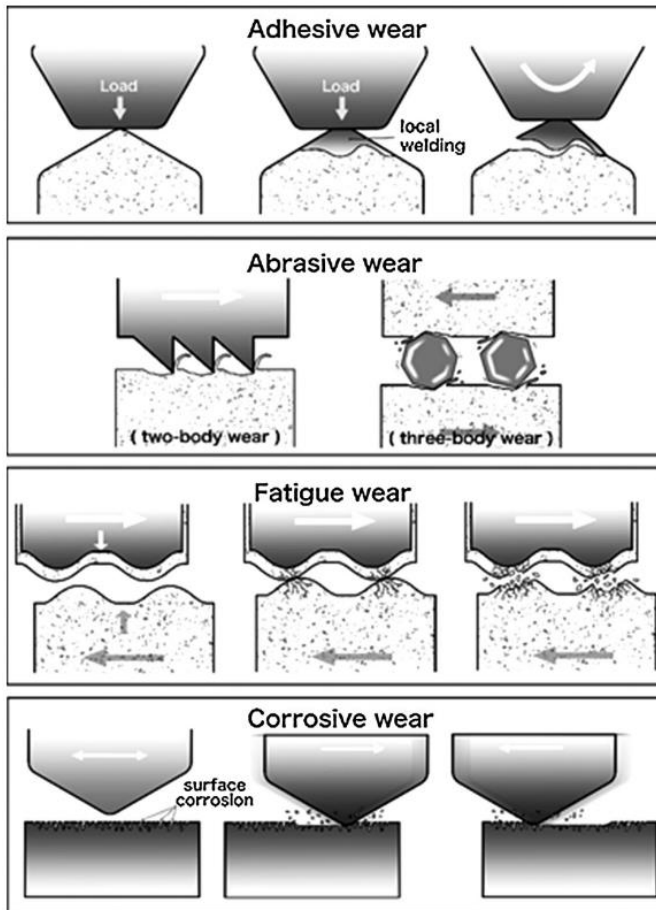
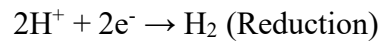
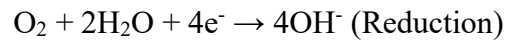
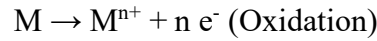


Figure 18. Schematic diagram explaining different wear mechanisms. Reproduced from Ref. [106] which is under an open-access Creative Common CC BY license.

4.2 Electrochemistry of corrosion

Corrosion is defined as the deterioration of a material or its functional properties due to chemical reactions with the surrounding environment [107]. It involves irreversible interfacial reactions between a material and its environment, resulting in material loss or the dissolution of environmental constituents into the material [108]. This phenomenon is especially common in metals, which are prone to chemical reactions that lead to corrosion. A common example of corrosion is the rusting of iron that gradually deteriorates the material properties over time.

In an aqueous solution, metals release electrons and get oxidized, whereas the released electrons are taken by dissolved oxygen or the protons present in the solution, i.e.



Most metals, especially stainless steels, are passive since they form a protective oxide coating on the surface that prevents any interaction of underlying metal to the corroding environment (Figure 19). Therefore, as shown in Figure 19, in passive conditions, the oxidation/reduction reactions occur via an intermediate phase where the metal reacts with oxygen from water, forming a metal oxide [108]. Subsequently, the metal oxide dissolves, releasing dissolved metal ions (M^{n+}) into the surrounding medium. The overall reaction rate is restricted by the sluggish movement of ions through the passive film and further interaction with the solution at the interface.

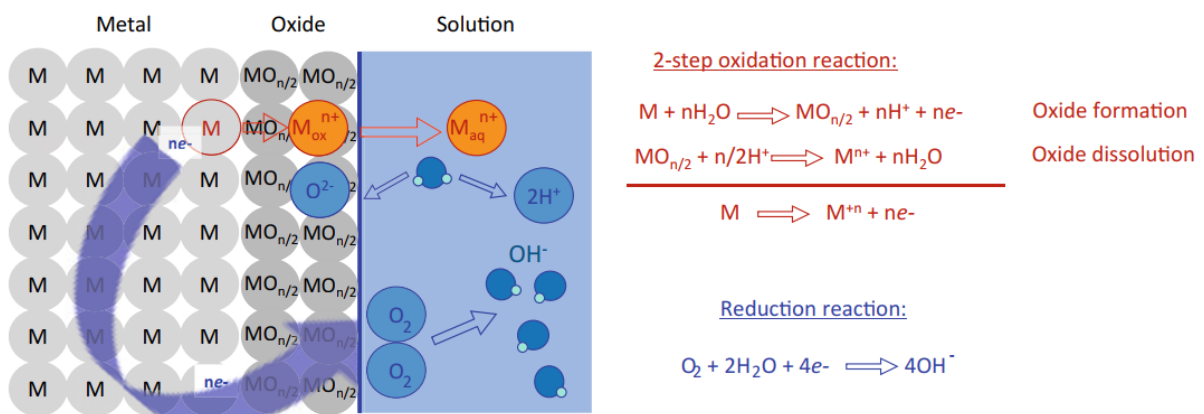


Figure 19. Corrosion phenomena taking place in a passive metal. Reproduced from Ref. [108], which is under the licence of CC-BY 4.0.

Various forms of corrosion exist, including uniform, crevice, pitting, galvanic, stress corrosion cracking, intergranular, and erosion corrosion [109]. Uniform corrosion results in material loss occurring consistently across the entire surface. Pitting corrosion involves localized attack in passive metals due to surface imperfections and aggressive anions, such as Cl^{-} in marine environments.

The study of electrochemical reactions, such as the corrosion rate at the metal-solution interface, is based on electrochemistry principles. Without external factors, corrosion systems act as self-driven electrochemical setups that are short-circuited, where both anodic and cathodic reactions occur on the same surface (check Figure 20). So, in conclusion, metal corrosion involves an internal flow of current between the oxidation site (anode) and the reduction site (cathode) as electrons are transferred between them.

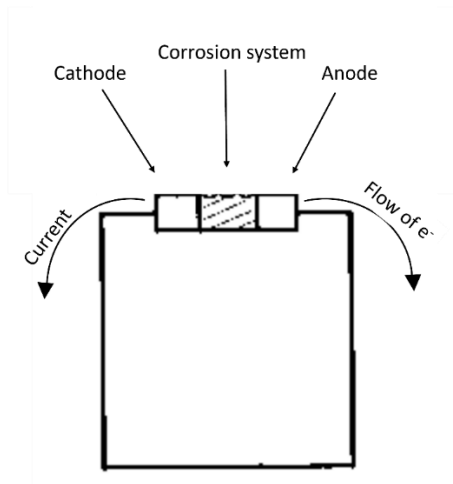


Figure 20. Electrochemical cell formed during metal corrosion. Reproduced from Ref. [110], which is under the licence of CC-BY 4.0.

As outlined by Faraday's law, the amount of metal that undergoes an electrochemical reaction is directly related to the electric charge transferred across the electrode and electrolyte interface [108]. Hence, the corrosion rate is directly proportional to the current (the flow of electrons) passing through the interface. So, the corrosion rate is determined by the formula-

$$\text{Corrosion rate (C.R.)} = \frac{i}{nF} \quad (3)$$

where 'i' represents the current passing over the surface area of the anode, 'n' stands for the stoichiometric coefficient of electrons, while 'F' represents Faraday's constant, which is equal to 96,485 C/mol. The mass loss rate of metal under a corrosive environment is dependent on the C.R., atomic mass of the metal, and its density and is defined as-

$$\text{Mass loss rate (mm/year)} = \frac{3.276 \times i \times \text{Atomic Mass}}{nF \times \text{Density}} \quad (4)$$

Electrochemical Impedance Spectroscopy (EIS) is a widely recognized quantitative approach to finding metal corrosion rates. Figure 21 explains a general EIS setup consisting of three electrode systems connected to a potentiostat [111]. The working electrode (WE) denotes the metal under investigation for corrosion in contact with an aqueous solution. The reference electrode (RE) is typically a glass capillary with an open tip containing a standard electrolyte (Ag/AgCl or Hg/Hg₂Cl₂ solution) and provides a constant potential for the setup. The counter electrode (CE) serves as an additional interface dedicated to functioning as an anode or a cathode for this electrochemical setup. Platinum wires or graphite rods are commonly used as counter electrodes. To examine the corrosion kinetics of the WE, a constant potential of the WE is maintained relative to the RE while determining the current density under these

conditions. By employing a potentiostat, a range of potentials is applied to investigate how changes in potential affect the corrosion rate.

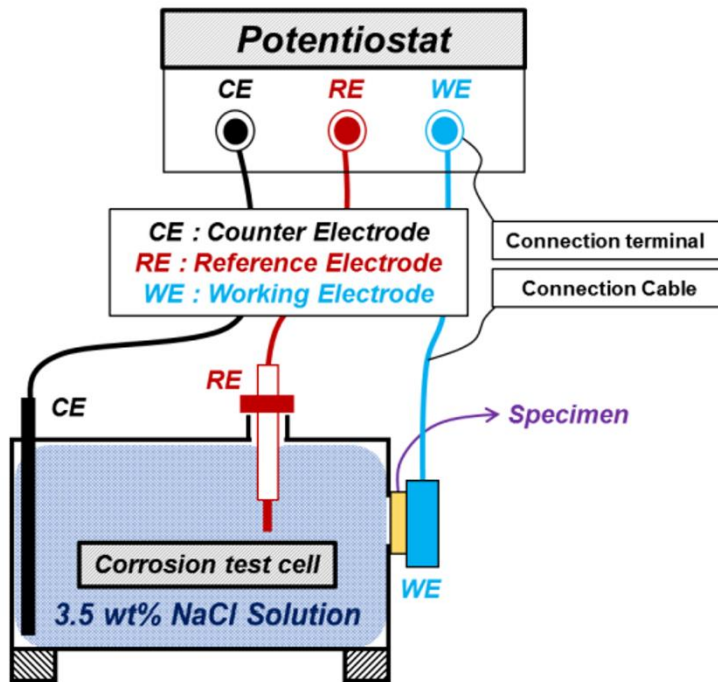


Figure 21. Experimental setup for EIS to measure corrosion rate. Reproduced from Ref. [111] which is under an open-access Creative Common CC BY license.

When the potentiostat has applied a range of potentials, the overall current, which consists of both anodic and cathodic current, is measured, as shown in Figure 22 (a). For calculating corrosion current (I_{corr}), the logarithmic magnitude of the current is taken on the X-axis (Figure 22 (b)). This kind of graph is called a polarization curve. The slope of each half of the modified curve is calculated and referred to as tafel slopes (β_a , β_c). At the extreme points, both curves show linear behavior, a mathematical equation for a line with a linear slope is derived, and the intersection of two lines gives the value for I_{corr} (Figure 22 (c)). The magnitude of this current (I_{corr}) is used to calculate the corrosion rate. Open circuit potential (OCP) is the potential (E_{corr}) at I_{corr} . The OCP is generally defined as the electrode potential of a WE compared to the RE in the absence of applied potential or electric current in the electrochemical cell. It indicates the ability of a metal to passivate in a corrosive environment [112].

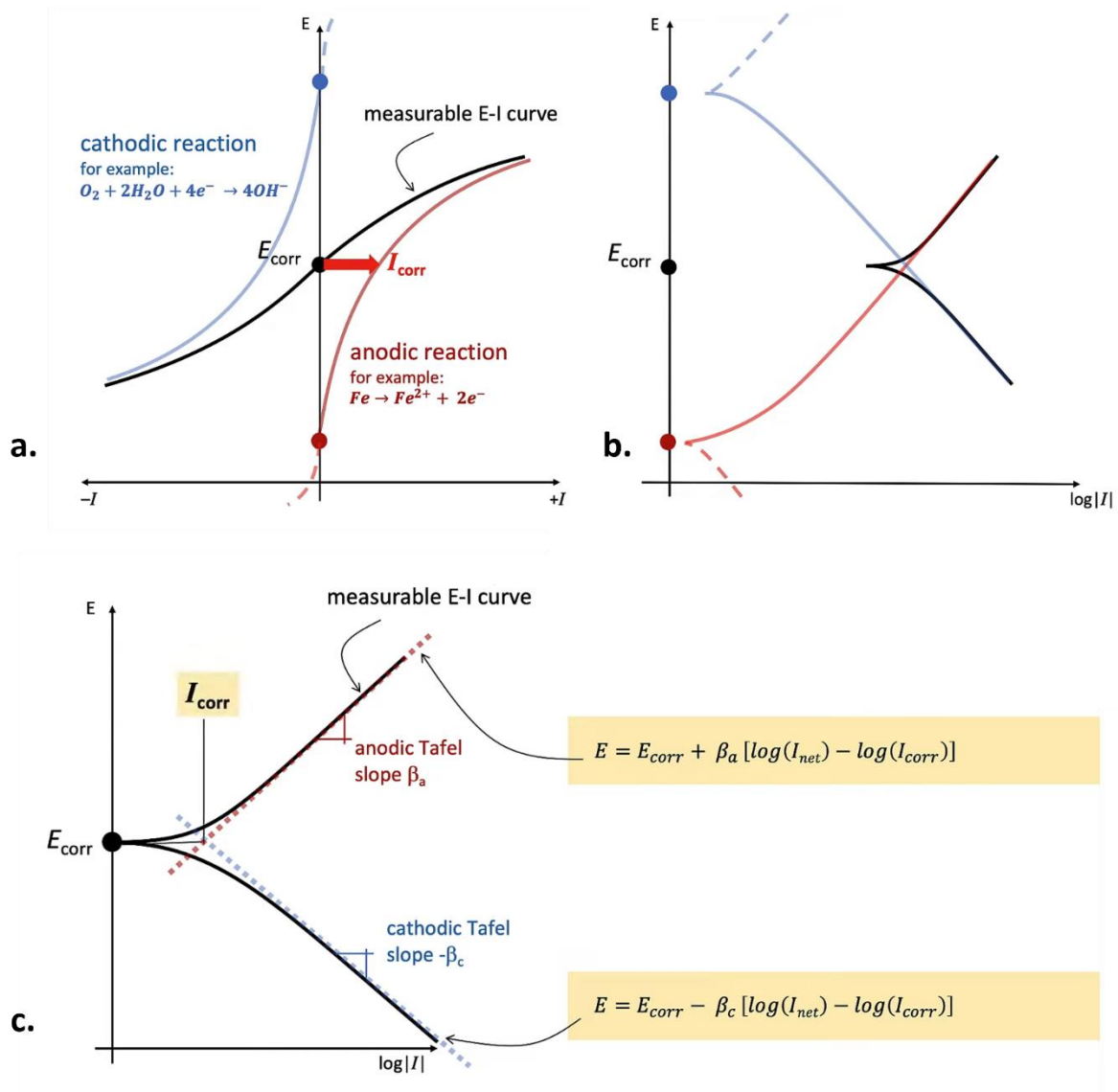


Figure 22. (a) Plot of anodic and cathodic current w.r.t to the applied potential, (b) Tafel plot consisting of a logarithmic magnitude of current on X-axis, (c) Equations used to derive E_{corr} and I_{corr} . Reproduced from Ref. [113] which is under an open-access Creative Common CC BY license.

4.3 Synergy of tribology and corrosion- Tribocorrosion

Tribocorrosion occurs when material degradation arises from the simultaneous effects of both corrosion and wear. Metals like stainless steel have a passive oxide layer that protects them from corrosion. However, when this passive layer gets damaged due to wear, cracking, or deformation, it triggers accelerated corrosion on the exposed surface [114]. This leads to corrosion occurring at a higher rate in the depassivated area until the passive layer is restored, as shown in Figure 23.

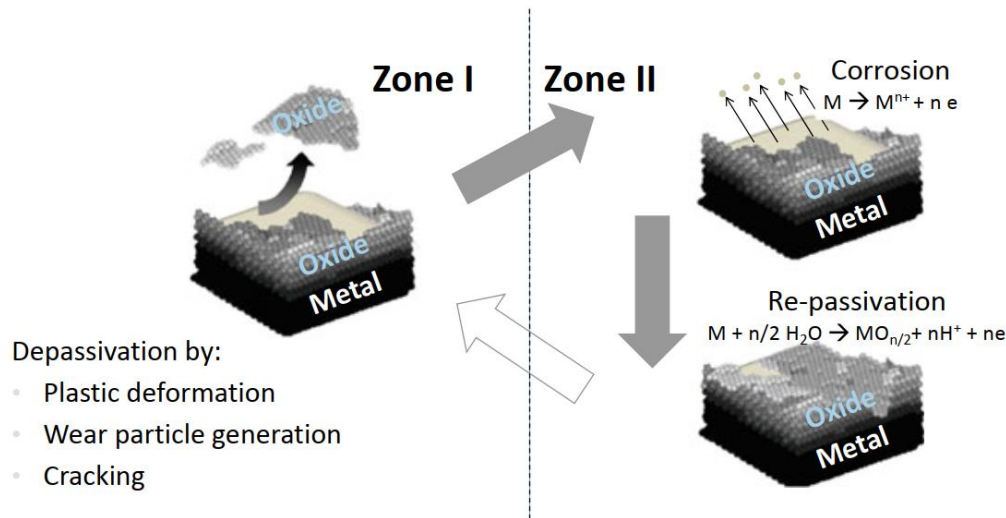


Figure 23. Schematic diagram explaining the cyclic process of depassivation and re-passivation leading to wear-accelerated corrosion. Reproduced from Ref. [114], which is under the licence of CC-BY 4.0.

An illustration of a tribocorrosion system is seen in Figure 24 - an excavator operating in an open-air environment. During idle periods, water from rain or moist ground triggers corrosion of the excavating components. Additionally, when the excavator is in action, the bucket teeth engage with dry ground and endure wear from abrasion caused by hard rocks or sand. During rainy weather, wear and corrosion occur simultaneously, leading to a case of tribocorrosion. Thus, tribocorrosion represents the simultaneous occurrence of wear and corrosion, a phenomenon encountered across various industrial applications needing detailed exploration and study [115].

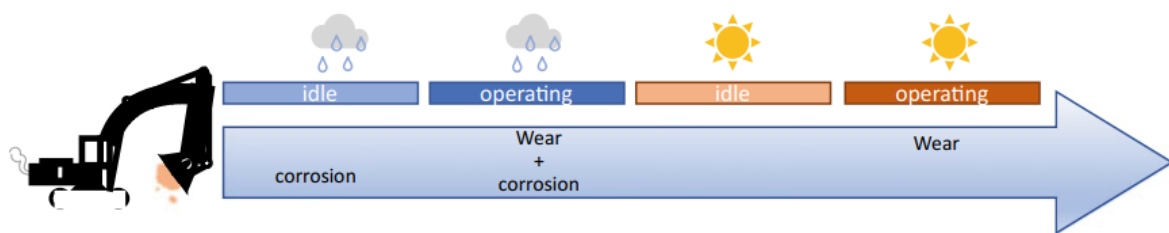
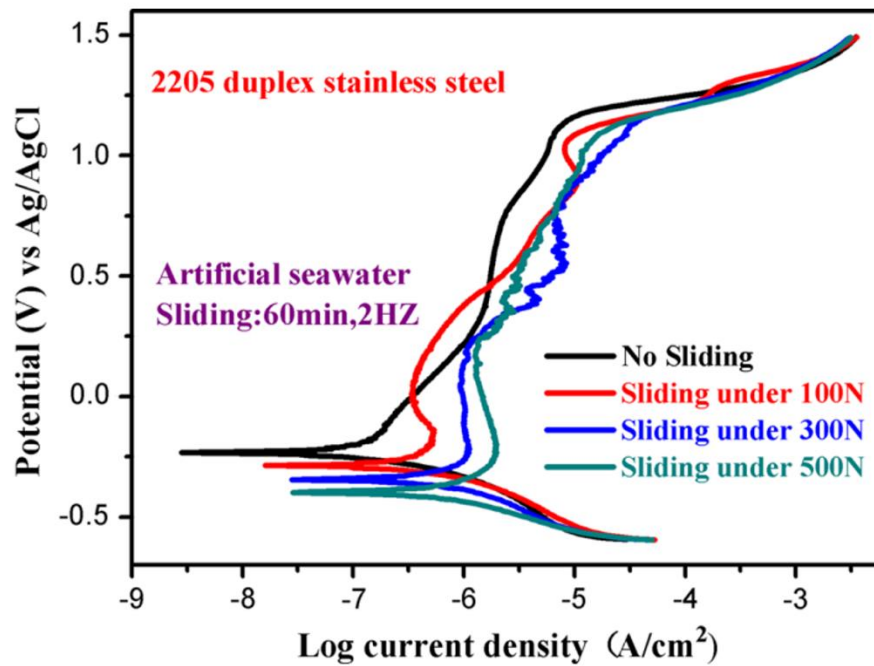


Figure 24. An example of a tribocorrosion system. Reproduced from [115], which is under the licence of CC-BY 4.0.

In marine environments, various components, such as offshore oil and gas pipelines, tidal drilling equipment, anchors and connectors for mooring systems, wind turbines, rotor blades, boat propeller shafts, etc., are exposed to corrosive conditions due to the saline environment. They also experience abrasion wear from sliding and fatigue caused by tidal waves, offshore wind, and vessel movements. This leads to a tribocorrosion system, resulting in material removal, surface degradation over time, and mechanical integrity loss [115].

far, no study has been reported on tribocorrosion study of a duplex SS manufactured via PBF-LB/M.



Load, N	0 N	100 N	300 N	500 N
E_{corr} , V	-0.239	-0.289	-0.353	-0.392
E_{pit} , V	1.203	1.141	1.022	1.012
I_{corr} , μA	0.0421	0.106	0.161	0.261

Figure 26. Polarization curve in static condition (no sliding) and dynamic loading conditions along with the calculated E_{corr} and I_{corr} values. Reproduced from Ref. [118], which is under the licence of CC-BY 4.0.

5 Aim and purpose of the experimental part

The study aims to assess whether PBF-LB/M manufactured NiFDSS can serve as a viable alternative to 316L for marine applications. The goal is to determine the wear and corrosion resistance of PBF-LB/Med NiFDSS compared to 316L under static and dynamic conditions in an artificial seawater environment. Additionally, the purpose is to investigate the influence of heat treatment (HT)-induced phase transformation on the tribological behavior and corrosion resistance of PBF-LB/Med NiFDSS. As shown in Figure 27, this study has been planned in four stages.

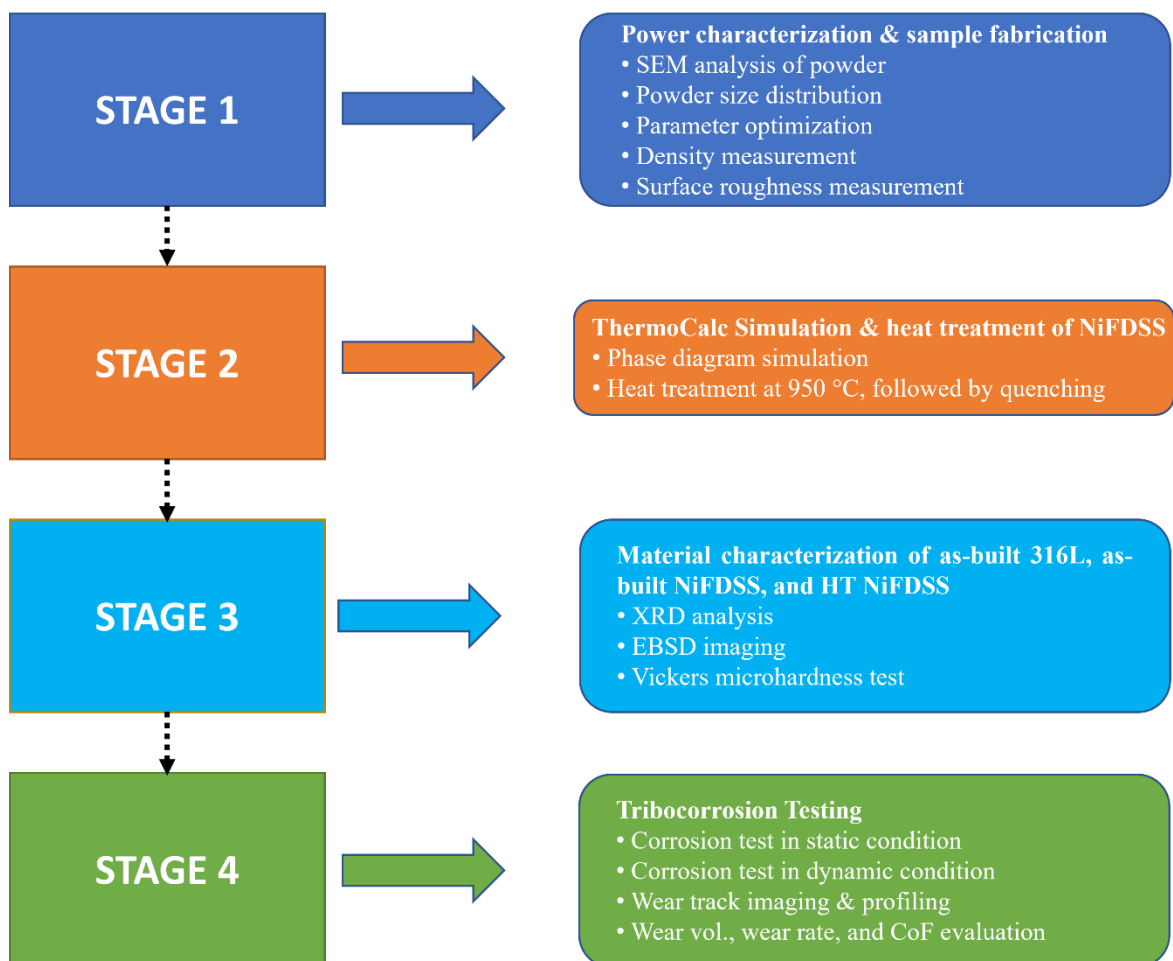


Figure 27. Different stages involved in the experimental part of the thesis.

As Figure 27 shows, stage 1 includes powder characterization and sample fabrication. SEM will be performed to analyze the powder morphology and size. Powder size distribution (PSD) will give the range of powder sizes present and the percentage of particles within specific size ranges. Performing these characterizations will help in understanding the characteristics of the powder, such as its flowability and packing density. The next stage in Figure 27 is to manufacture the sample via PBF-LB/M. For 316L, an optimized set of

parameters is already available in the PBF-LB/M printer database. However, NiFDSS is a novel material, and its process parameters must be optimized to fabricate defect-free parts. So, parameter optimization will be performed, and based on visual inspection and relative density measurements, the optimal parameter will be chosen to print NiFDSS samples. Surface roughness measurement will be done on printed specimens to understand the built quality and surface finish achieved via PBF-LB/M.

Stage 2 study, as shown in Figure 27, will be based on ThermoCalc simulation of the NiFDSS phase diagram. A heat treatment operation will be performed at a selected temperature on as-built NiFDSS samples, based on ThermoCalc results, using a box muffle furnace.




Stage 3 (see Figure 27) will be based on a detailed study of material characterization of as-built 316L, as-built NiFDSS, and HT NiFDSS samples. XRD will be done to understand the phase composition of powders as well as the three different sample types. EBSD imaging will reveal the percentage composition and distribution of phases in the matrix of the specimens. Vickers microhardness test will be done to understand the mechanical properties.

In stage 4, the main theme of this study, as seen in Figure 27, i.e., tribocorrosion tests, will be performed in a seawater environment. At first, a static corrosion test will be done to compare the passivity and anti-corrosion properties of as-built 316L against NiFDSS in as-built and HT cases. The next half will be on conducting corrosion rate evaluations in dynamic conditions. Wear track imaging, W_r , W_v , and CoF will also be evaluated simultaneously. These data can then be used to compare the wear and corrosion resistance of 316L and NiFDSS in marine environments.

6 Experimental setup

Table 2 provides a detailed overview of the various equipment used in this study. Each item listed is accompanied by an image and a description of its application.

Table 2. Various equipment used in this study, along with their images and applications. Reproduced from Ref. [119–125], which is under an open-access Creative Common CC BY license.

Equipment	Image	Purpose of use
Thermo Scientific Apreo 2 SEM setup		For capturing high-resolution images of powder particles.
Malvern MS3000		For analyzing particle size distribution.
Aconity MIDI+ system (equipped with 400 W SM fiber laser, F-Theta optics, and a 3D scanner)		To fabricate samples via PBF-LB/M

<p>Thermo-Calc software package</p>		<p>To predict the stability of various phases in NiFDSS over a wide temperature range</p>
<p>Malvern Panalytical Empyrean XRD</p>		<p>To detect various phases present in as-built 316L, as-built NiFDSS, and HT NiFDSS using X-ray diffraction.</p>
<p>Falcon 608 hardness tester</p>		<p>To evaluate Vickers microhardness of different samples.</p>
<p>Bruker Alicona Infinite Focus G6 confocal microscope</p>		<p>For predicting the surface roughness of as-built samples, W_v measurements and wear profile imaging</p>

<p>Zeiss Crossbeam 540 SEM and an EDAX Hikari Plus EBSD detector</p>		<p>To evaluate the percentage of different phases and their distribution in the microstructure.</p>
<p>Densimeter H-3000s</p>		<p>For measuring relative density %</p>
<p>Nabertherm box muffle furnace</p>		<p>For performing heat treatment of as-built NiFDSS samples</p>
<p>Tribocorrosion setup consisting of DUCOM POD 4.0 tribometer and IviumSoft Vertex potentiostat</p>		<p>To perform tribocorrosion test on as-built 316L, as-built NiFDSS, and HT NiFDSS in an artificial seawater environment</p>

7 Experimental procedure

7.1 Materials used

316L gas-atomized powders used in this study were supplied from SLM Solutions Group AG. NiFDSS gas-atomized powders were purchased from Sandvik Osprey Ltd. Table 3 highlights the information about the chemical composition of the powders as provided by the manufacturers.

Table 3. Chemical composition of 316L and NiFDSS in wt. %

316L:	Cr	Mn	Mo	Si	N	C	S	P	Ni	O	Fe		
	17.84	0.90	2.43	0.64	0.10	0.020	0.01	0.007	12.5	0.02	Balance		
NiFDSS:	Cr	Mn	Mo	Si	N	C	S	P	Ni	O	Nb	Co	Fe
	17.3	11.40	3.24	0.7	0.177	0.028	0.005	0.017	0.10	0.156	0.01	0.01	Balance

7.2 Powder characterization

PSD was calculated using a laser diffraction technique to obtain the distribution curve. The experiments were performed twice to increase the accuracy of the result. Figure 28 illustrates the SEM images of the powder particles along with the PSD curves.

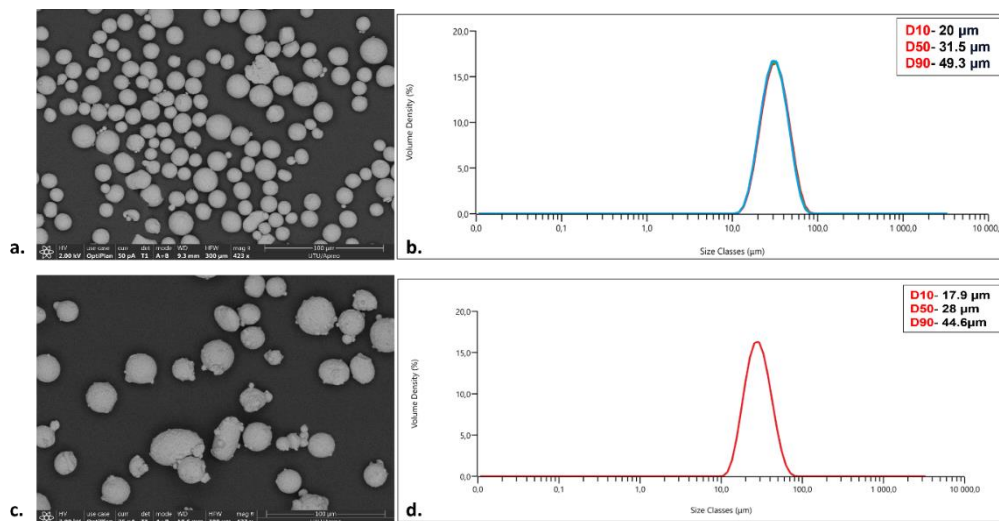


Figure 28. (a) SEM image of 316L powder, (b) PSD curve of 316L powder, (c) SEM image of NiFDSS powder, (d) PSD curve of NiFDSS powder.

The powder particles exhibited a spherical shape with slight protrusions, as depicted in Figure 28 (a, c). The D10, D50, and D90 values in the PSD curves (Figure 28 (b, d)) represent the particle diameters at which 10%, 50%, and 90% of the particles are smaller than or equal to

those diameters and their lower values for NiFDSS powders compared to 316L indicated that the NiFDSS particles were smaller in size.

7.3 Sample fabrication via PBF-LB/M

During sample fabrication, argon supply was maintained in the build chamber to keep the oxygen level below 500 ppm. Two distinct sets of samples were fabricated for various purposes in this study: the first was cylindrical samples measuring 15 mm in height and 30 mm in diameter, used for process parameter optimization and material characterization, and the second, cylindrical discs with a diameter of 60 mm and a height of 11 mm, for tribocorrosion testing.

7.3.1 PBF-LB/M of 316L

For 316L, the process parameters were available in the Aconity database. Laser power of 150 W, scanning speed of 900 mm/s, hatch distance of 0.08 mm, layer thickness of 0.03 mm, and laser spot diameter of 80 μm were used to fabricate 316L samples (check Figure A 1*). As shown in Figure 29, a stripe-hatching pattern scanning strategy was used to fabricate all samples used in this study. The stripe width was 5 mm, and the scanning direction was rotated by 67° for each consecutive layer to ensure that the thermal gradients changed direction, leading to reduced and evenly distributed residual stresses to prevent cracking in parts.

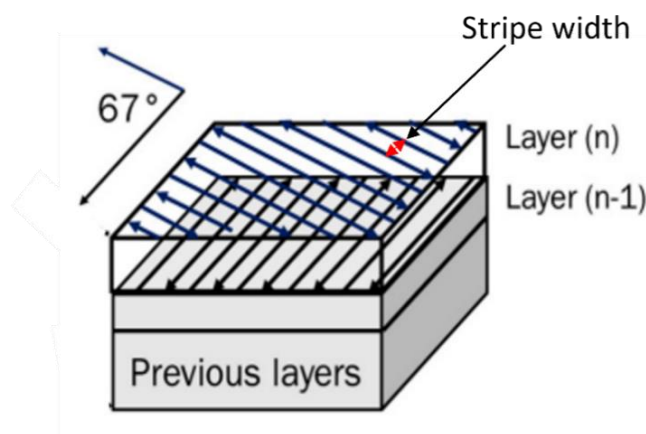


Figure 29. Schematic illustration depicting the stripe hatching pattern scanning strategy, with a rotation of 67° between consecutive layers. Reproduced from Ref. [126] which is under an open-access Creative Common CC BY license.

* Check Appendix 2 for this image.

7.3.2 Process parameter optimization of NiFDSS

Tuomas et al. optimized the process parameters of NiFDSS manufactured via PBF-LB/M [27,127]. The optimized parameters were 110 W or 160 W for laser power, scanning speed at 600 mm/s, layer thickness of 0.03 mm, and hatch distance of 0.08 mm. Initial sets of samples were fabricated using these parameters. Using these samples as the reference, a new design of experiment was adopted. Relative density measurement was performed on each sample to find the porosity %. Samples were weighed both in open air and immersed in distilled water. The optimal laser power for PBF-LB/M of NiFDSS was chosen based on relative density data and visual inspection. The surface roughness of the as-built 316L sample and as-built NiFDSS with the optimized parameter was also evaluated.

7.4 Heat treatment of as-built NiFDSS

Figure 30 shows the volume fraction of various phases in NiFDSS over a temperature range. The X-axis represented the temperature range, whereas the Y-axis depicted the stability of different phases (α , γ , sigma, chi) by giving their volume fractions. Based on the obtained graph, 950 °C was chosen as the heat treatment temperature as both α and γ phases will be present in the matrix, resulting in a duplex structure. Also, undesirable sigma, chi, and other intermetallic will not precipitate at this temperature. The heat treatment was performed in an ambient atmosphere. The specimens were subjected to a heating rate of 10 °C/min until reaching 950 °C, where they were kept for one hour. After that, samples were taken out and quenched in water.

TCFE10 : Fe, Cr, Mo, Si, N, C, Co, S, P, Ni, O, Nb, Mn
Pressure [Pa] = 100000.0, System size [mol] = 1.0, Mass percent Cr = 17.3, Mass percent Mo = 3.24, Mass percent Si = 0.7, Mass percent N = 0.177, Mass percent C = 0.028, Mass percent Co = 0.01, Mass percent S = 0.005, Mass percent P = 0.017, Mass percent Ni = 0.1, Mass percent O = 0.156, Mass percent Nb = 0.01, Mass percent Mn = 11.4

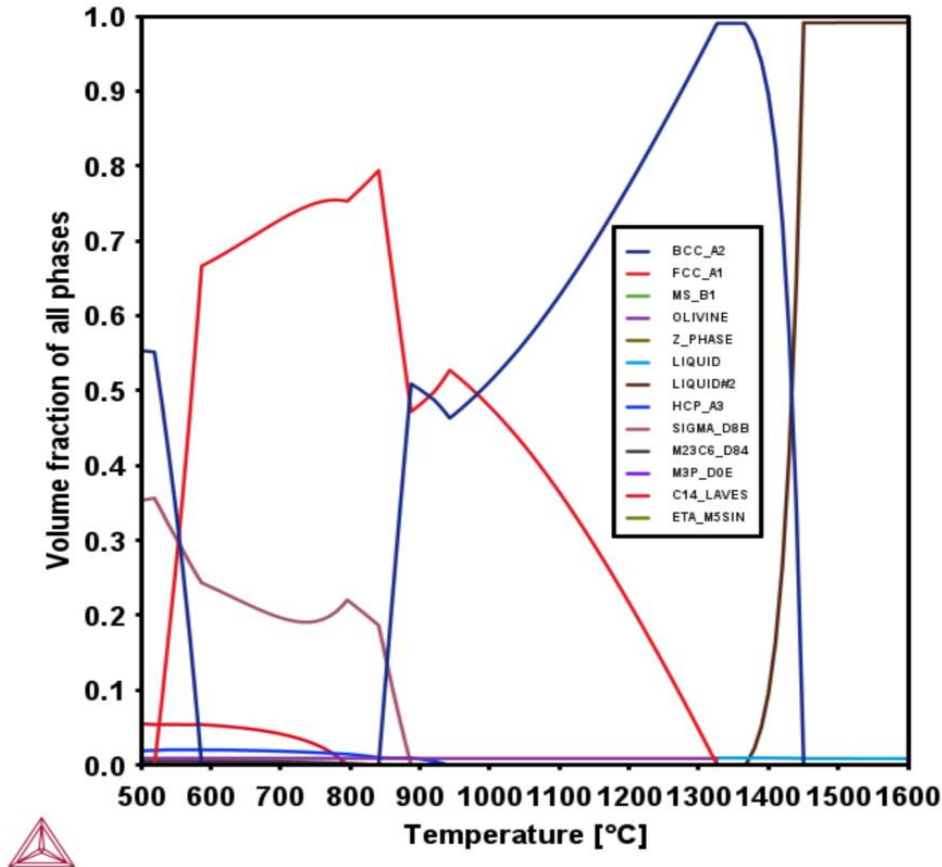


Figure 30. Phase fraction of NiFDSS over different temperature ranges (BCC- α , FCC- γ).

7.5 Material characterization of samples

For the Vickers microhardness test and XRD, as-built 316L, as-built NiFDSS, and HT NiFDSS samples underwent grinding from coarse 80-grit size to fine 4000-grit size using SiC papers. Then, the samples were polished using diamond suspensions of 3 μm , 1 μm and 0.25 μm . Vickers microhardness test was performed with the HV1 scale, and a dwell time of 10 seconds was used in the study. For each sample, eight hardness measurements were taken. XRD analysis was conducted on powders, as-built samples, and HT sample using Cu-K α radiation to collect data within a 2θ range spanning from 20° to 90°.

For EBSD analysis, cross-sectional samples were embedded in conductive resin, ground using SiC papers, and polished to achieve a mirror-like surface finish employing 0.02 μm oxide polishing suspension. EBSD analysis parameters included 20 keV energy, 3 nA current, and a

15 mm working distance. A scanning step size of 300 nm was used. EBSD inverse pole figure and phase maps were subsequently examined.

7.6 Tribocorrosion tests

For tribocorrosion testing, as shown in Figure 31, a ball-on-disc tribometer was employed in conjunction with a three-electrode setup and a potentiostat. Two monitors were used to measure wear and corrosion rates simultaneously. The sample to be tested was connected as WE. Platinum wire and Ag/AgCl (3M) were used as CE and RE, respectively. Before the tribocorrosion test, samples were ground to 4000-grit SiC paper and then polished using diamond suspensions (3 μm , 1 μm , and 0.25 μm) to obtain a mirror finish (i.e. surface roughness < 1 μm). After that, the polished samples were ultrasonicated in acetone and ethanol solution to ensure no contamination. A 0.6 M NaCl solution was used to prepare artificial seawater, the pH of which was adjusted to 8.2 by adding 0.1 M NaOH [118,128].

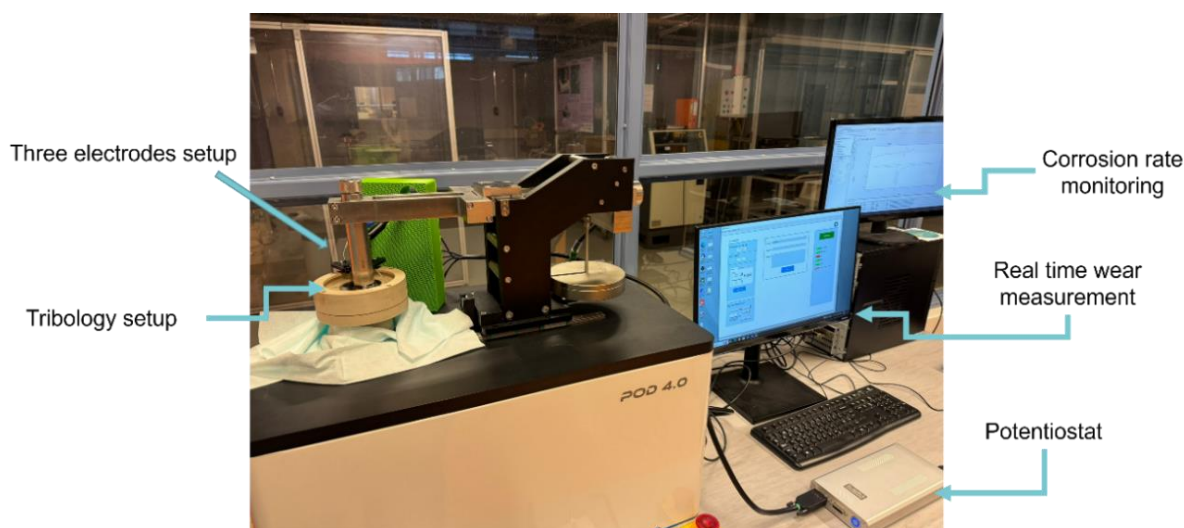


Figure 31. Tribocorrosion setup used in this study.

7.6.1 Corrosion test in static condition

A corrosion test in static condition was performed first, i.e., without counter load and rotation. Ten minutes were allocated to stabilize *OCP*. The polarization scan ranged from -0.8 V to +0.8 V. Scan rate of 0.5 mV/s was used, and the potential step size was 0.1 mV. After the test, polarization curves were obtained for as-built 316L, as-built NiFDSS, and HT NiFDSS. A model data analysis tool was used to analyze the curves to attain the corrosion rate, and it is available with the IviumSoft software package. The surface area exposed to the corrosion environment, equivalent weight, and density values were fed into the software, and the

corrosion rate was automatically calculated (see Figure A 3*). For all the samples, the exposed surface area to the seawater was 25.05 cm². Equivalent weight was calculated according to ASTM Designation G: 102-89 [129]. The calculated equivalent weight for NiFDSS was 25.558 g, while for 316L, it was 25.564 g. Based on the chemical composition of 316L and NiFDSS, the theoretical density was 7.9 g cm⁻³ and 7.73 g cm⁻³, respectively. Finally, the corrosion rate of all the samples was obtained.

7.6.2 Corrosion test in dynamic condition

To replicate tribocorrosion conditions, a 6 mm diameter alumina ball positioned in a holder was brought into contact with the sample, applying a counter load of 60 N on the opposite end. The setup was rotated with 10 RPM, and the selected wear track diameter was 6 mm. The tribology test was performed for 56 minutes. After 2 minutes from the start, corrosion rate monitoring was initiated. Similar to the static condition, the polarization scan ranged from -0.8 V to +0.8 V with a scan rate of 0.5 mV/s and a potential step size of 0.1 mV. The corrosion rate under a wear-induced dynamic environment was calculated using IviumSoft software with a similar approach.

The plot of CoF variation was obtained in real-time using DUCOM monitoring software. W_v was determined by conducting optical profilometry on the wear scars using the MetaMax software of Bruker Alicona Infinite Focus G6, which was also used to capture wear track images (check Figure A 4*). W_r was calculated using the formula mentioned in Table 1.

* Check Appendix 2 for this image.

8 Results and discussions

8.1 Optimized process parameters for NiFDSS

Figure 32 shows the samples fabricated with previously optimized parameters by Tuomas et al. [28]. As shown in Figure 32 (a), delamination between the layers with a 110 W laser power was observed, indicating a lower VED than required. Conversely, with 160 W (see Figure 32 (b)), over-melting and distortion were observed in the samples, indicating higher VED than the optimal value.

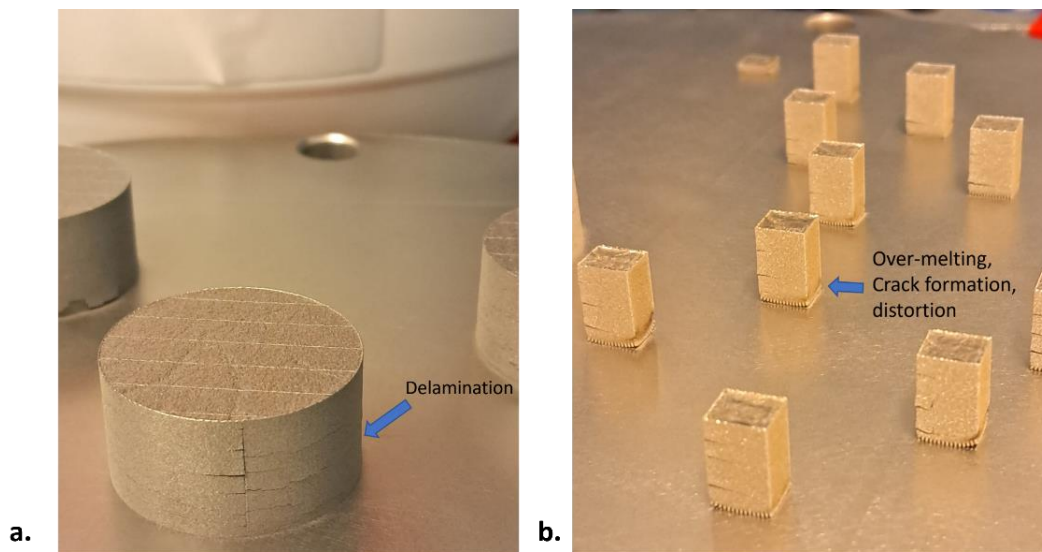


Figure 32. (a) Sample with 110 W laser power (b) Sample with 160 W laser power.

Figure 33 illustrates the new design of the experiment adopted in this study. To find the optimal VED for getting crack-free and denser samples, the laser power parameter was varied from 110 W to 160 W with a step size of 10 W. Other process parameters were kept constant as varying them will increase the experimental work and is beyond the scope of this thesis. In the first trial, eleven specimens were fabricated (see Figure 33) using the abovementioned parameters. Six parameters were selected for the second trial based on visually examining cracks and delamination in the as-built specimens (see Figure A 2*).

* Check Appendix 2 for this image.

1. Power= 110 W, Speed=600 mm/s, Hatch= 0.08 mm, Layer thickness= 0.03 mm, VED= 76.3 J/mm ³
2. Power= 115 W, Speed=600 mm/s, Hatch= 0.08 mm, Layer thickness= 0.03 mm, VED= 79.86 J/mm ³
3. Power= 120 W, Speed=600 mm/s, Hatch= 0.08 mm, Layer thickness= 0.03 mm, VED= 83.30 J/mm ³
4. Power= 125 W, Speed=600 mm/s, Hatch= 0.08 mm, Layer thickness= 0.03 mm, VED= 86.80 J/mm ³
5. Power= 130 W, Speed=600 mm/s, Hatch= 0.08 mm, Layer thickness= 0.03 mm, VED= 90.27 J/mm ³
6. Power= 135 W, Speed=600 mm/s, Hatch= 0.08 mm, Layer thickness= 0.03 mm, VED= 93.75 J/mm ³
7. Power= 140 W, Speed=600 mm/s, Hatch= 0.08 mm, Layer thickness= 0.03 mm, VED= 97.22 J/mm ³
8. Power= 145 W, Speed=600 mm/s, Hatch= 0.08 mm, Layer thickness= 0.03 mm, VED= 100.69 J/mm ³
9. Power= 150 W, Speed=600 mm/s, Hatch= 0.08 mm, Layer thickness= 0.03 mm, VED= 104.16 J/mm ³
10. Power= 155 W, Speed=600 mm/s, Hatch= 0.08 mm, Layer thickness= 0.03 mm, VED= 107.63 J/mm ³
11. Power= 160 W, Speed=600 mm/s, Hatch= 0.08 mm, Layer thickness= 0.03 mm, VED= 111.11 J/mm ³

Figure 33. Design of experiment to find the optimal process parameters. The blue marker boxes represent parameters from the previous study, while the orange markers denote parameters selected for further optimization in this investigation.

Figure 34 represents the samples fabricated after the first trial in which the laser power varied from 110 W to 160 W while other process parameters were kept constant. Visual analysis of the as-built samples revealed minimal cracks between 140 W and 160 W, with no signs of delamination. At 150 W, holes were observed along the curved surface. Hump formation was evident across all samples, particularly pronounced between 145 W to 160 W and less prominent at 120 W. Some issues with the recoater of the Aconity MIDI+ led to non-uniform powder distribution across the build plate, which resulted in missing areas between the support and the build part for samples processed at 110 W, 115 W, 130 W, and 135 W. The first attempt concluded that 140 W was the optimal laser power as there were no signs of burning, distortion, or deformation due to residual stress in the sample.



Figure 34. As-built NiFDSS specimens manufactured with varying laser power from 110 W to 160 W. Based on the observation of the first trial, for the second attempt, samples were fabricated with laser power from 120 to 145 W. During the second attempt between 120 W to 145 W, it was observed that cracks disappeared after 135 W, indicating that the optimal power range lies between 135 W to 145 W. Cracks were observed in samples processed at 120 W, 125 W, and 130 W. Therefore, the conclusion was in alignment with the first attempt.

Figure 35 (a) represents the calculated density of PBF-LB/Med NiFDSS samples with varied laser power. For 140 W laser power, the maximum density of 7.64 g/cm^3 was noted. The

theoretical density of NiFDSS based on chemical composition was 7.73 g/cm^3 . So, the relative density (RD) of the 140 W laser samples can be evaluated as-

$$RD (\%) = \frac{\text{Calculated density}}{\text{Theoretical density}} \times 100 \quad (5)$$

$$i.e. RD (\%) = \frac{7.640}{7.73} \times 100 = 98.83 \%$$

Therefore, based on visual and RD measurements, 140 W was selected as the optimal laser power to fabricate defect-free NiFDSS samples. PBF-LB/Med NiFDSS samples fabricated with optimized parameters (140 W laser power, 600 mm/s scanning speed, hatch distance 0.08 mm, and layer thickness of 0.03 mm) are shown in Figure 35 (b). Compared to the previous study by Tuomas et al. [27,28], in which RD of 98.542 % was achieved with a laser power of 120 W, in this study, with a laser power of 140 W, RD of 98.83 % was obtained.

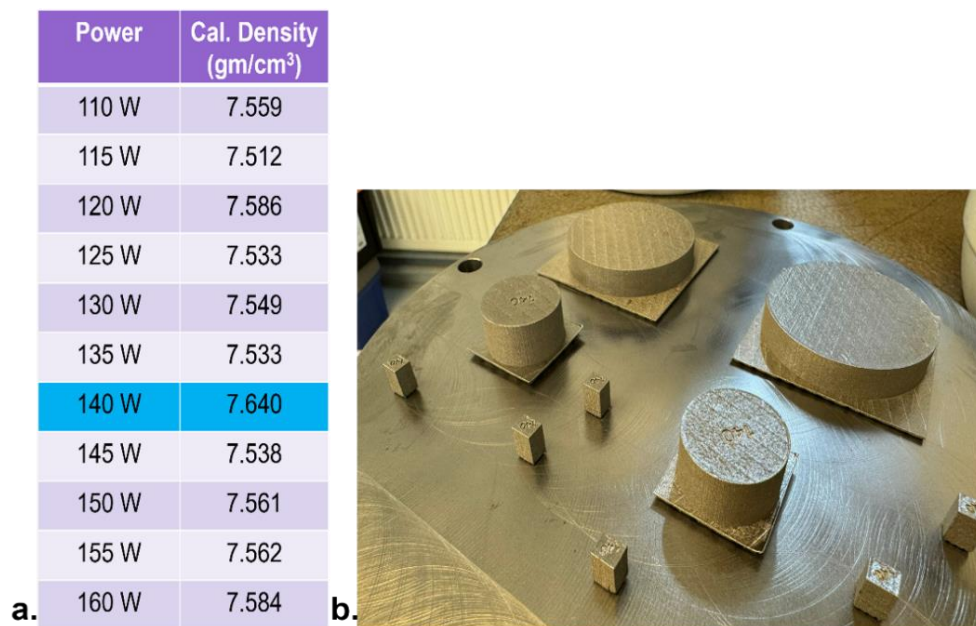


Figure 35. (a) The calculated density of as-built NiFDSS samples using Densimeter based on Archimedes' principle, (b) NiFDSS samples fabricated with the optimized process parameters

Using a similar approach, the RD of as-built 316L samples, whose process parameters were available in the Aconity database, was calculated at 99.80 %. So, in comparison, PBF-LB/Med 316L had fewer defects than as-built NiFDSS samples. More optimization works need to be done to attain a relative density of more than 99.5 % for NiFDSS.

Figure 36 illustrates the variance in the surface topography of the fabricated 316L sample and NiFDSS sample with the optimized parameter. More peaks and valleys were observed in 316L samples, showcasing surface irregularities compared to NiFDSS. The calculated surface

area roughness (S_a) by averaging the data obtained from six different regions was $11.26 \pm 0.23 \mu\text{m}$ for 316L and $8.68 \pm 0.34 \mu\text{m}$ for the NiFDSS sample. The higher surface roughness for 316L can be due to the bigger particle size, as PSD determines the surface finish, as coarser particles in the powders lead to a rougher surface [130].

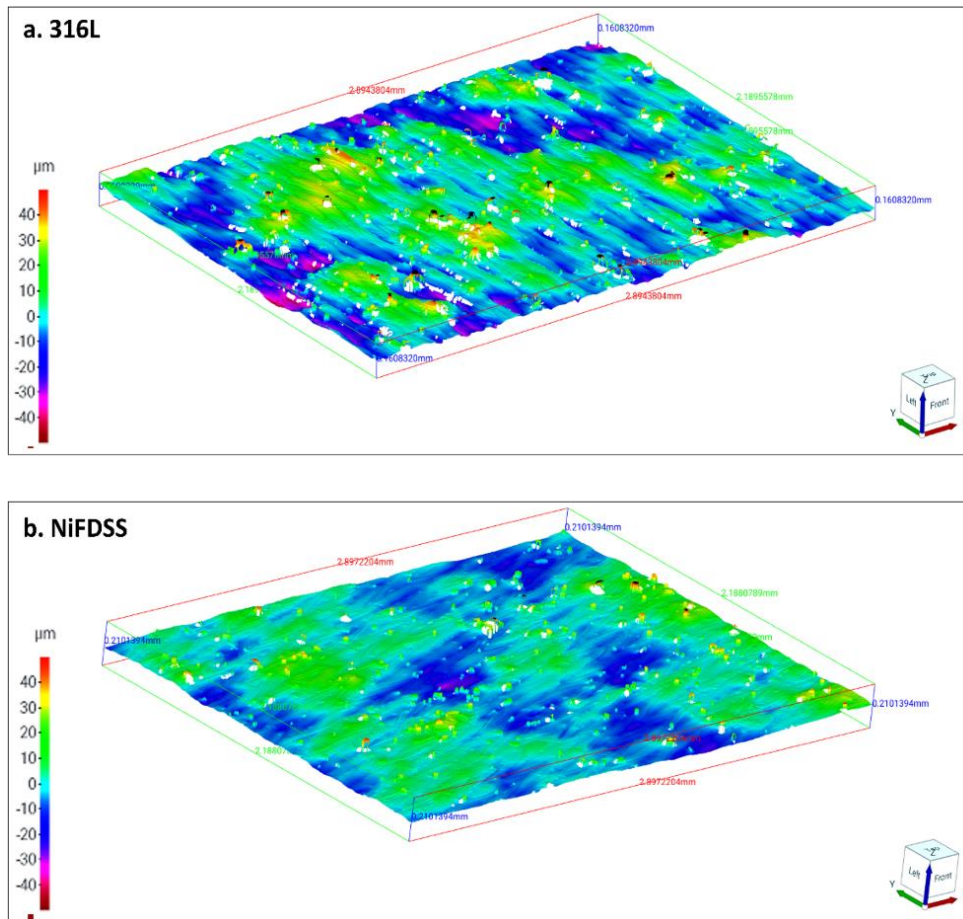


Figure 36. Surface topography of (a) as-built 316L (b) as-built NiFDSS, obtained using Alicona confocal microscopy

8.2 Microstructure and phase analysis

Figure 37 illustrates the phase composition of powder particles and samples used in this study. For 316L, both powder and as-built specimen had only austenitic peaks. In the case of NiFDSS, the powder and as-built sample had ferritic peaks. This is because while NiFDSS powders were gas-atomized from molten metal, austenite could not emerge into the matrix due to a very high cooling rate during solidification. A similar scenario occurred during PBF-LB/M of NiFDSS. Due to the cooling rate in the range of 10^5 to 10^6 K/s, a fully ferritic microstructure was retained. However, when the NiFDSS samples were HT, the austenite phase emerged into the microstructure from the ferritic grain boundaries, resulting in the detection of both austenite and ferrite peaks during XRD.

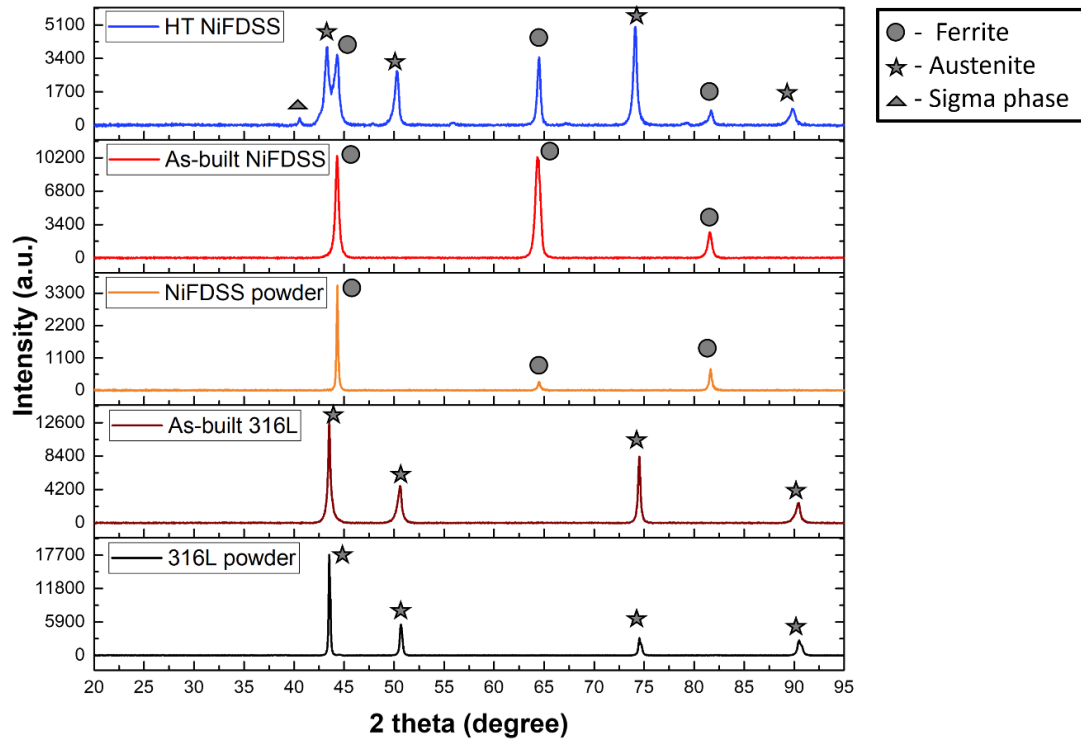


Figure 37. XRD peaks representing different phases present in 316L powder, as-built 316L sample, NiFDSS powder, as-built NiFDSS sample, and HT NiFDSS sample.

EBSID imaging shown in Figure 38 supports a similar analogy. The as-built 316L had 99.9 % austenite in the matrix, while the as-built NiFDSS had 98.8 % ferrite phase. After HT, as shown in Figure 38 (c), a duplex microstructure was obtained, containing 61.4 % ferrite, 34 % austenite, and 3.8 % unwanted sigma phase, which is detrimental to the corrosion and mechanical properties [131]. HT, followed by quenching, could not completely avoid the precipitation of the undesired intermetallic sigma phase for DSS.

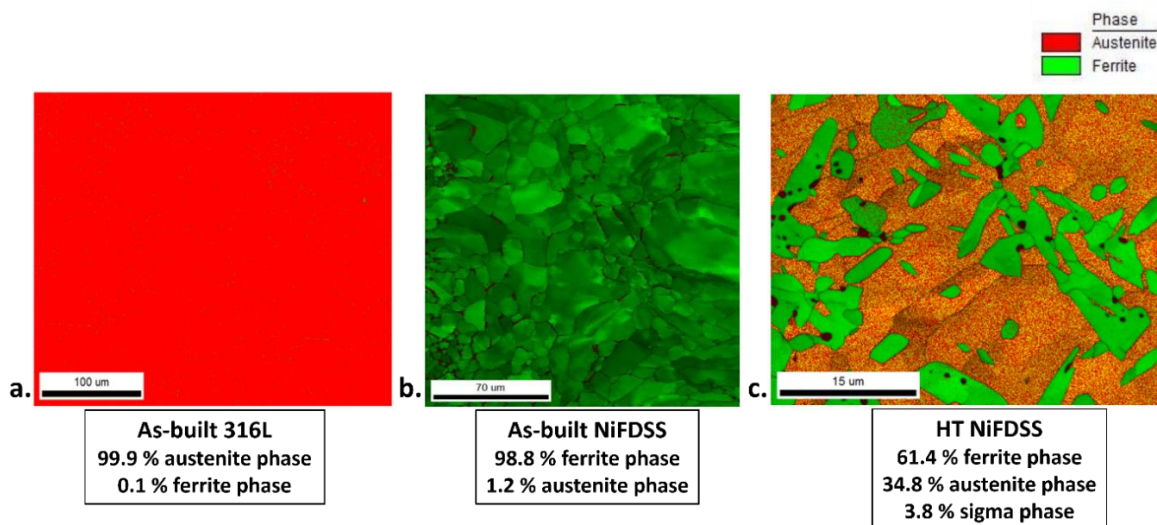


Figure 38. EBSD phase mapping of the specimens. Red indicates the austenite phase, green represents the ferritic phase, and small dark red dots are the sigma phase.

The graph in Figure 39 compares the hardness of different samples, with as-built NiFDSS showing the highest hardness due to its fully ferritic structure. The ferrite phase has higher hardness than austenite [127,132]. Since the HT NiFDSS had both phases in the microstructure, it had hardness values between those of the as-built NiFDSS and as-built 316L.

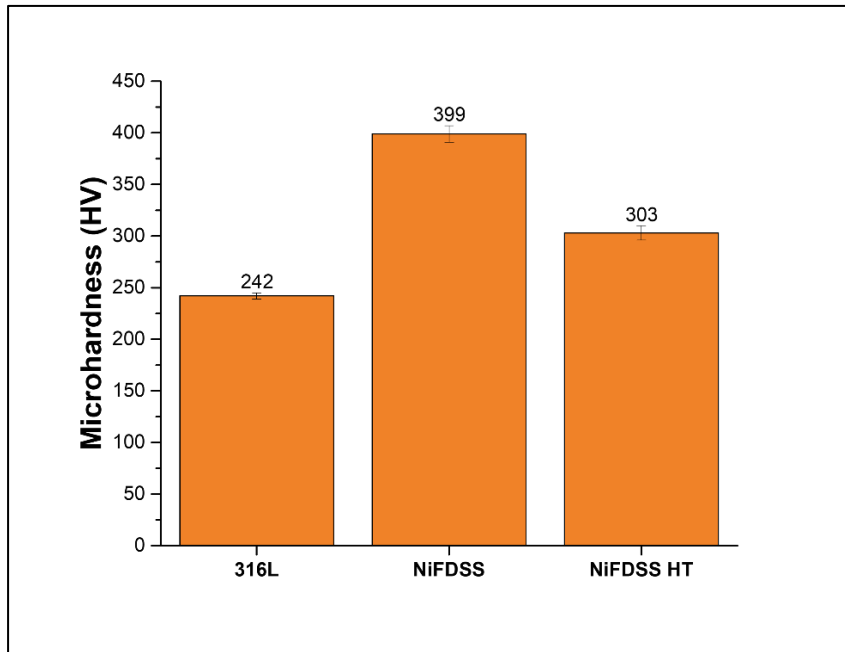


Figure 39. Comparison of Vickers microhardness of as-built 316L, as-built NiFDSS, and HT NiFDSS.

8.3 Tribocorrosion study

8.3.1 Wear analysis

In Figure 40, the wear track profile has been used to analyze the variance of wear depth. For 316L, uniform wear took place, as illustrated by the color map, as the dark pink area (the high wear zones) was scattered uniformly across the wear scar. However, localized wear had taken place for NiFDSS and more extreme for HT NiFDSS, as evidenced by the dark pink patches across the wear track.

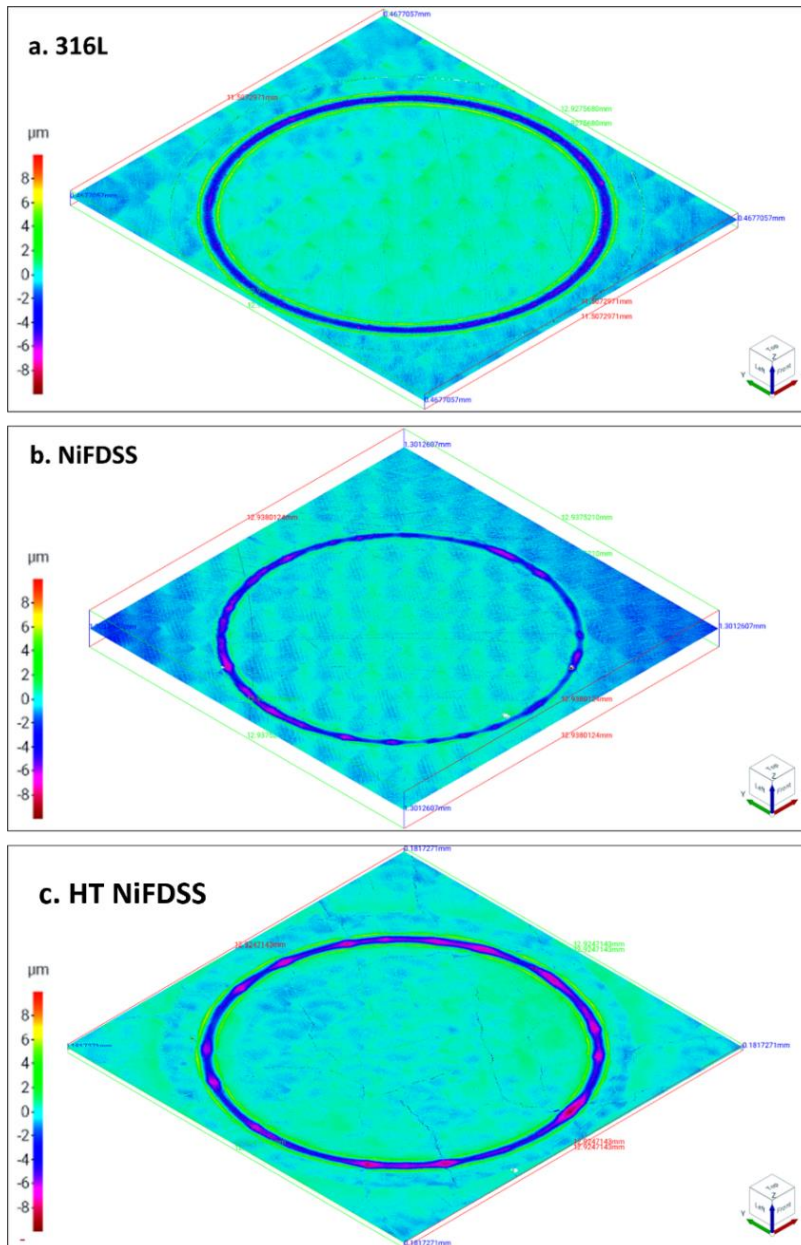


Figure 40. Wear track profile for analyzing the wear depth.

Figure 41 includes the images captured in the wear track area for the different samples. Wear tracks observed in Figure 41 explain the mechanism of wear. As seen in Figure 41 (a), metal chips were in the center of the wear track, pointing toward plastic deformation and adhesive wear. Abrasive wear also occurred as grooves were noticed along the wear direction. In the case of NiFDSS and HT NiFDSS, grooves were intense, and there were no metal chips, proving that the wear mechanism is fully abrasive due to the brittleness of the specimen. Further, there was a complete removal of metal particles from some regions, and, as shown in Figure 41 (c), those regions were bigger in the case of HT NiFDSS. This analysis aligns with the wear depth profile shown in Figure 40 (c). SEM analysis was planned to understand the wear mechanism in more detail. However, due to time limitations, it could not be performed.

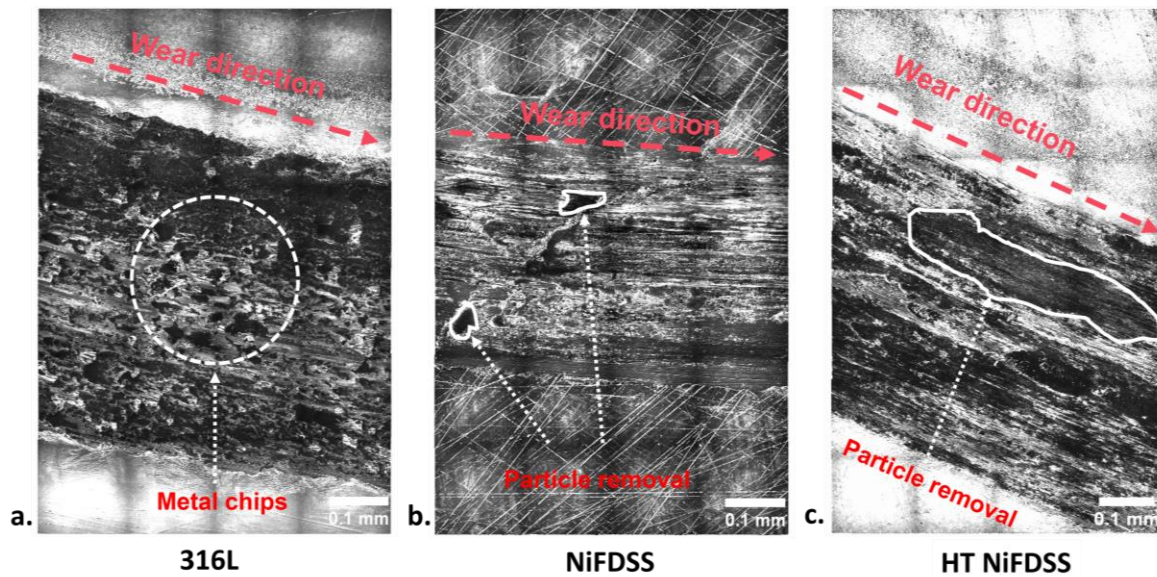


Figure 41. Wear track imaging to understand the wear mechanism.

Table 4 showcases the wear volumes determined for each sample to calculate the wear rate (W_r). W_r can be evaluated using the formula previously mentioned in Table 1. The applied normal force (F_n) is 60 N, and the total distance covered in this study is-

$$\begin{aligned} \text{Total distance } (D) &= \text{RPM} \times 2\pi R \times \text{time} & (6) \\ \text{i. e. } D &= (10 \times 2 \times 3.14 \times 3 \times 56) \text{ mm} = 10550.40 \text{ mm} \end{aligned}$$

Table 4. Calculated wear volume of the samples used in the study.

Sample	Wear volume (in mm ³)
As-built 316L	0.020
As-built NiFDSS	0.025
HT NiFDSS	0.030

Figure 42 represents the evaluated W_r for the specimens. The W_r of HT NiFDSS was maximum, followed by as-built NiFDSS and as-built 316L. The data proves the analysis done so far as the localized wear for NiFDSS in both conditions had increased its W_r compared to 316L, which had uniform wear taking place. This study confirms that 316L has better wear resistance than NiFDSS in both conditions since NiFDSS undergoes brittle fracture during the wear test. Wear behavior also depends on the RD . The wear resistance can be enhanced if more process optimization is performed to obtain a defect and crack-free NiFDSS sample.

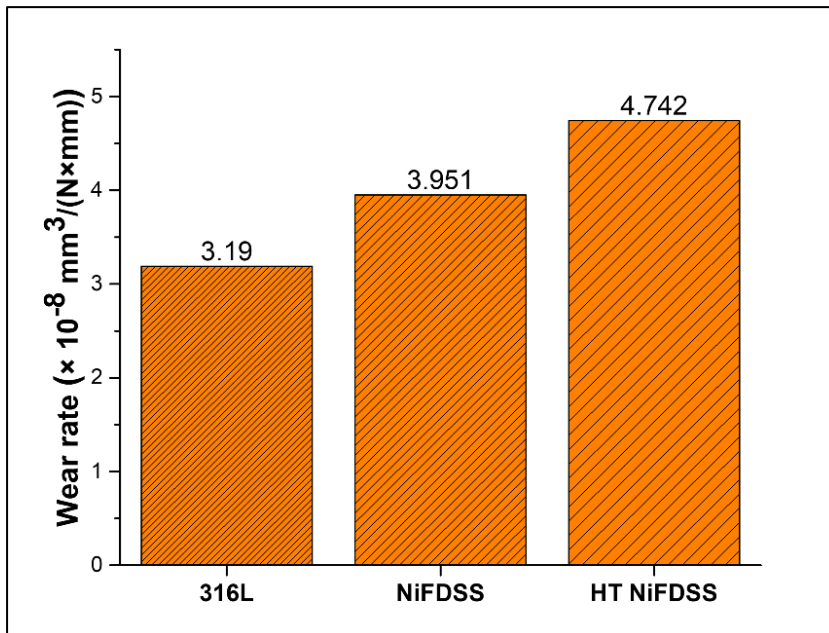


Figure 42. Wear rate comparison of as-built 316L, as-built NiFDSS, and HT NiFDSS

Figure 43 describes the variations in CoF during the tribocorrosion study. As shown in Figure 43, as-built NiFDSS had the lowest CoF , which can be attributed to its higher microhardness compared to 316L and HT NiFDSS. The CoF values oscillated for 316L, and for HT NiFDSS, the CoF values increased, remained stable, decreased, and increased to the stable value again. The reason behind this variation is unclear yet, and a more detailed analysis needs to be done.

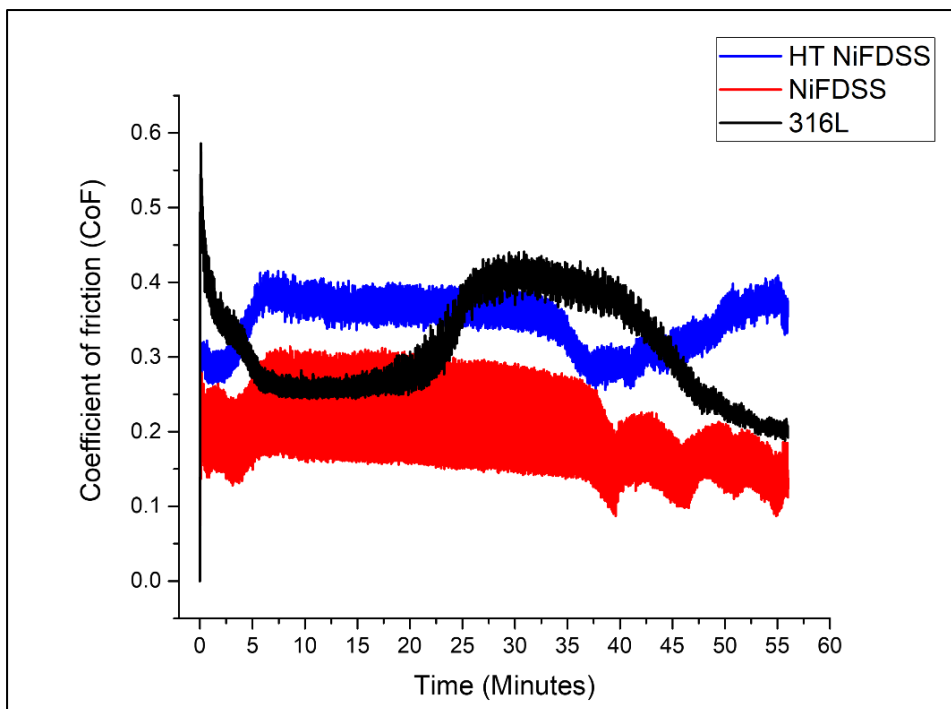


Figure 43. Variation of CoF during the wear test.

8.3.2 Corrosion test in static condition

Figure 44 (a) illustrates the polarisation curves obtained to study the corrosion behavior. 316L showcased the maximum passivation potential, i.e., OCP under a seawater environment, followed by NiFDSS and HT NiFDSS. As shown in Figure 44 (b), I_{corr} was the minimum for HT NiFDSS; thereby, it had the minimum corrosion rate ($C.R.$) as I_{corr} is directly proportional to $C.R.$ NiFDSS has a higher PREN value of 30.824 compared to 24.459 of 316L. So, the as-built NiFDSS outperformed the as-built 316L in corrosion resistance. Upon HT, due to the formation of a duplex phase that further enhanced the resistivity against corrosion, the $C.R.$ of HT NiFDSS was less than 50 % of as-built NiFDSS and 62 % than that of as-built 316L.

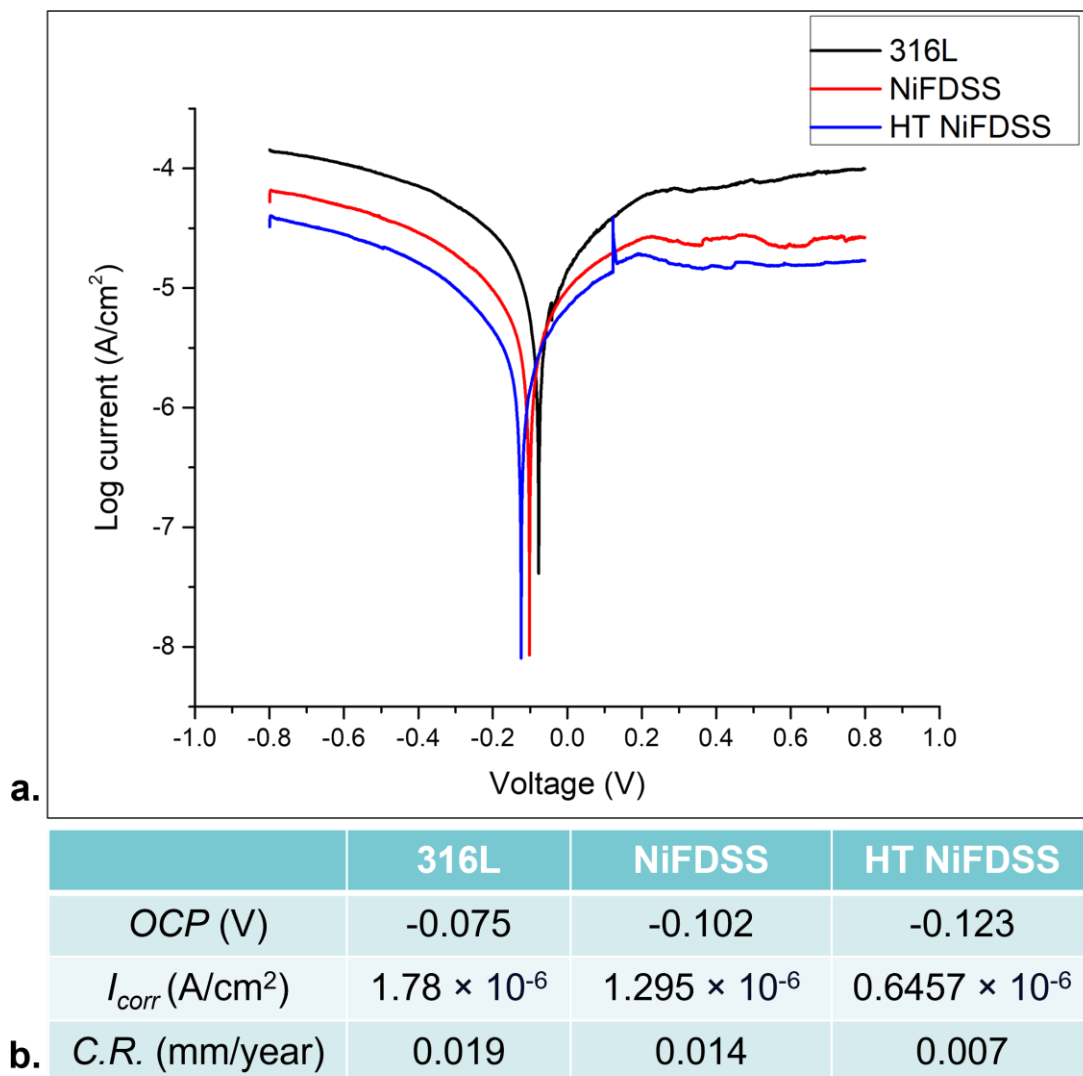


Figure 44. (a) Polarisation curves of 316L, NiFDSS, and HT NiFDSS in an artificial seawater environment (0.6 M NaCl) with pH 8.2 under static conditions, (b) The obtained data from evaluating the curves using IviumSoft software, comparing the OCP , I_{corr} , and $C.R.$

8.3.3 Corrosion test in dynamic condition

Figure 45 (a) describes the polarisation curves obtained under dynamic conditions, i.e., wear-induced corrosion. The setup containing the samples had a 10 RPM rotation against the counter load of 60 N, resulting in accelerated wear against the alumina ball. As-built NiFDSS had higher passivation potential in dynamic conditions. Following a similar trend in the case of the static condition, as shown in Figure 45 (b), HT NiFDSS had the least *C.R.* followed by as-built NiFDSS and as-built 316L.

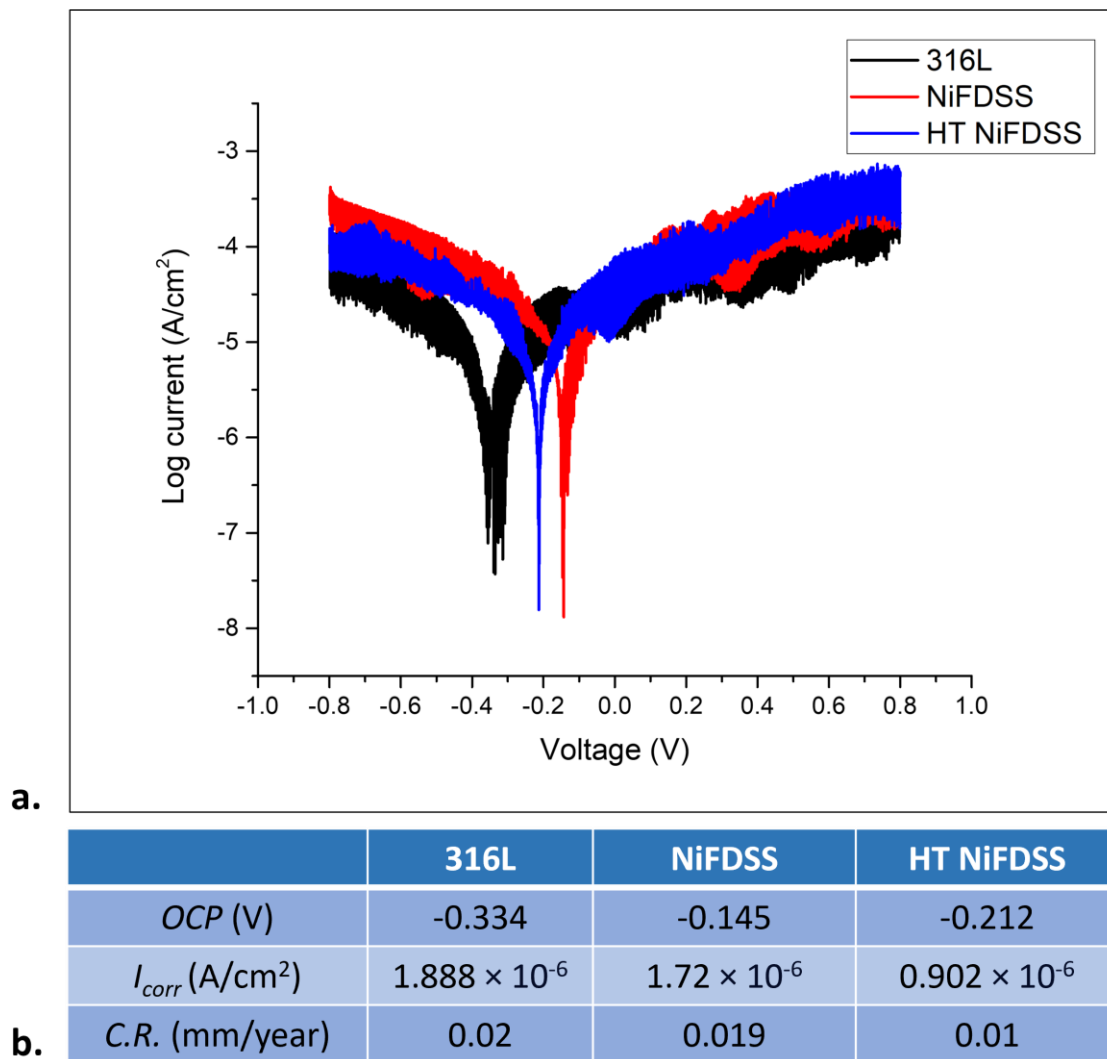


Figure 45. (a) Polarisation curves of 316L, NiFDSS, and HT NiFDSS in an artificial seawater environment (0.6 M NaCl) with pH 8.2 under dynamic condition of 10 RPM and 60 N counter load against alumina ball, (b) The obtained data from evaluating the curves using IviumSoft software, comparing the *OCP*, *I_{corr}*, and *C.R.*

Figure 46 compares the increase in *C.R.* in static vs dynamic conditions. A significant increase was noticed for as-built NiFDSS and HT NiFDSS, which could have resulted from higher and localized wear and more surface area exposure to corrosive conditions, as shown

in Figure 41 includes the images captured in the wear track area for the different samples. . However, for all the specimens in both conditions, *C.R.* fell below 0.025 mm/year, a critical threshold indicative of excellent corrosion resistance for the steel grade under consideration [110].

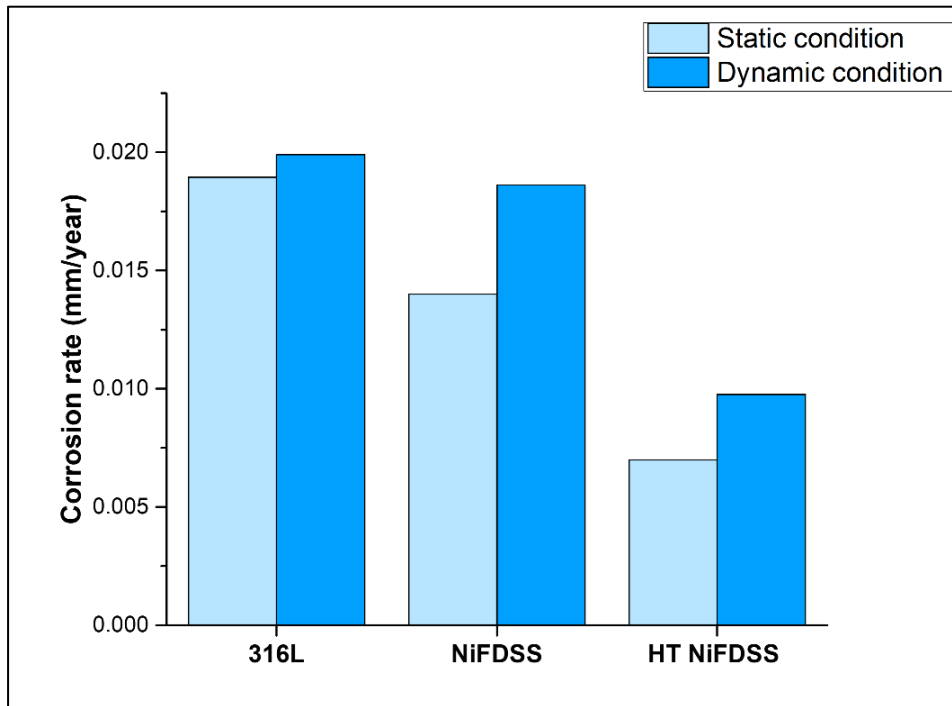


Figure 46. Comparison plots of *C.R.* of as-built NiFDSS, as-built 316L, and HT NiFDSS in static and dynamic conditions under an artificial seawater environment.

9 Conclusion

In conclusion, this study aimed to validate whether NiFDSS samples fabricated through PBF-LB/M could be an alternative to 316L for equipment used in seawater environments. The research focused on three primary questions: whether NiFDSS could exhibit wear and corrosion resistance comparable to 316L in seawater, both under static and mechanical loading conditions; how phase transformation induced by heat treatment affects the tribological behavior and corrosion resistance of NiFDSS; and the overall viability of NiFDSS for marine applications, as well as the role of PBF-LB/M in manufacturing these components.

After process parameter optimization, a relative density of 98.83 % was achieved for PBF-LB/Med NiFDSS samples. 316L in both powder and as-built condition had an austenitic phase. In the case of NiFDSS, powder, and as-built samples were fully ferritic, and a duplex microstructure was obtained after heat treatment. Through comprehensive investigation, it was found that NiFDSS had superior corrosion resistance in seawater environments compared to 316L grade, both in its as-built state and after heat treatment. The formation of a duplex phase in heat-treated NiFDSS enhanced its corrosion resistance. However, 316L demonstrated better wear resistance and uniform wear patterns, whereas NiFDSS showed localized wear in seawater conditions.

Further process optimization is necessary to achieve more than 99.5% relative density for as-built NiFDSS samples and improve their wear behavior. These findings provide industrially relevant insights and highlight the potential of NiFDSS as a viable choice for components in corrosive marine environments when the parts are not subjected to intense wear, with PBF-LB/M offering design flexibility and the ability to fabricate complex structures.

10 Further studies

In the present study, mechanical tests such as the nanoindentation test to determine the elastic modulus of samples and the tensile test to understand the ductility and fracture strength have not been performed. The in-detailed mechanical analysis should be conducted in the future to better understand the mechanical performance of NiFDSS compared to 316L for marine applications.

In the tribology section, SEM imaging on the wear track has not been included, which is crucial for understanding and comprehending the wear mechanisms involved. EDS mapping of elements in the wear track region can reveal whether 316L, NiFDSS, or HT NiFDSS has higher oxygen content in the passive oxide layer.

Moreover, expanding the scope of tribocorrosion tests to include multiple environmental conditions beyond artificial seawater would be beneficial. Understanding the behavior of NiFDSS and 316L under elevated temperatures, particularly in the 300-500°C range, could provide valuable insights into their hot corrosion resistance, which is crucial for applications in demanding environments, such as nuclear applications.

The present thesis is a preliminary step in a detailed, comprehensive study of NiFDSS. It lays the groundwork for future in-depth analyses and practical implementations within various industries.

References

- [1] P.-J. Cuna, *Alloying Elements in Stainless Steel and Other Chromium-Containing Alloys*, (2004).
- [2] C.O.A. Olsson, D. Landolt, *Passive films on stainless steels - Chemistry, structure and growth*, *Electrochim Acta* 48 (2003) 1093–1104. [https://doi.org/10.1016/S0013-4686\(02\)00841-1](https://doi.org/10.1016/S0013-4686(02)00841-1).
- [3] K.H. Lo, C.H. Shek, J.K.L. Lai, *Recent developments in stainless steels*, *Materials Science and Engineering R: Reports* 65 (2009) 39–104. <https://doi.org/10.1016/j.mser.2009.03.001>.
- [4] AUSTENITIC, MARTENSITIC, FERRITIC STAINLESS STEEL, (n.d.). <https://eagletube.com/about-us/news/austenitic-martensitic-ferritic-stainless-steel/> (accessed March 3, 2024).
- [5] P. Lambert, 6 - Sustainability of metals and alloys in construction, in: J.M. Khatib (Ed.), *Sustainability of Construction Materials*, Woodhead Publishing, 2009: pp. 148–170. <https://doi.org/https://doi.org/10.1533/9781845695842.148>.
- [6] S. Kahar, *Duplex Stainless Steels-An overview*, *Int J Eng Res Appl* 07 (2017) 27–36. <https://doi.org/10.9790/9622-0704042736>.
- [7] NA, *What is the difference between austenitic and martensitic stainless steel?*, (n.d.). <https://www.oshwin.com/blog/difference-between-austenitic-and-martensitic-stainless-steel.html#:~:text=The%20content%20of%20chromium%20in,to%20higher%20levels%20of%20chromium.> (accessed May 18, 2024).
- [8] M.A. Fajobi, T.R. Loto, O.O. Oluwole, *Austenitic 316L Stainless Steel; Corrosion and Organic Inhibitor: A Review*, *Key Eng Mater* 886 (2021) 126–132. <https://doi.org/10.4028/www.scientific.net/kem.886.126>.
- [9] Iris. Alvarez-Armas, Suzanne. Degallaix-Moreuil, *Duplex stainless steels*, ISTE, 2009.
- [10] M.F. McGuire, *Stainless steels for design engineers*, ASM International, 2008.
- [11] N. Haghadi, C. Ledermueller, H. Chen, Z. Chen, Q. Liu, X. Li, G. Rohrer, X. Liao, S. Ringer, S. Primig, *Evolution of microstructure and mechanical properties in 2205 duplex stainless steels during additive manufacturing and heat treatment*, *Materials Science and Engineering: A* 835 (2022). <https://doi.org/10.1016/j.msea.2022.142695>.
- [12] *History of duplex stainless steel*, (n.d.).
- [13] *History of duplex stainless steel*, (n.d.). <https://www.outokumpu.com/en/expertise/2020/duplex-90-years/history-of-duplex-stainless-steel> (accessed March 3, 2024).
- [14] R. Francis, G. Byrne, *Duplex stainless steels—alloys for the 21st century*, *Metals (Basel)* 11 (2021). <https://doi.org/10.3390/met11050836>.

- [15] S. Liu, C. Yue, X. Chen, Q. Zhu, Y. Tu, Pitting corrosion resistance on annealing treated super duplex stainless steel s32750, *Crystals (Basel)* 10 (2020) 1–15.
<https://doi.org/10.3390/CRYST10040294>.
- [16] S. Hägg Mameng, L. Wegrelius, R. Pettersson, A CORROSION MANAGEMENT AND APPLICATIONS ENGINEERING MAGAZINE FROM OUTOKUMPU Atmospheric Corrosion Resistance of Stainless Steel: Results of a Field Exposure Program in the Middle-East Atmospheric Corrosion Resistance of Stainless Steel: Results of a Field Exposure Program in the Middle-East, 2015.
- [17] Lean Duplex Stainless Steel, (2012).
- [18] J. Wang, P.J. Uggowitzer, R. Magdowski, M.O. Speidel, NICKEL-FREE DUPLEX STAINLESS STEELS, 1998.
- [19] A. Jadhav, V.S. Jadhav, A review on 3D printing: An additive manufacturing technology, *Mater Today Proc* 62 (2022) 2094–2099. <https://doi.org/10.1016/j.matpr.2022.02.558>.
- [20] M.H. Mobarak, M.A. Islam, N. Hossain, M.Z. Al Mahmud, M.T. Rayhan, N.J. Nishi, M.A. Chowdhury, Recent advances of additive manufacturing in implant fabrication – A review, *Applied Surface Science Advances* 18 (2023). <https://doi.org/10.1016/j.apsadv.2023.100462>.
- [21] J. Bedmar, S. García-Rodríguez, M. Roldán, B. Torres, J. Rams, Effects of the heat treatment on the microstructure and corrosion behavior of 316 L stainless steel manufactured by Laser Powder Bed Fusion, *Corros Sci* 209 (2022). <https://doi.org/10.1016/j.corsci.2022.110777>.
- [22] V.B. Vukkum, R.K. Gupta, Review on corrosion performance of laser powder-bed fusion printed 316L stainless steel: Effect of processing parameters, manufacturing defects, post-processing, feedstock, and microstructure, *Mater Des* 221 (2022).
<https://doi.org/10.1016/j.matdes.2022.110874>.
- [23] G.O. Barrionuevo, M. Walczak, J. Ramos-Grez, P. Mendez, A. Debut, Microstructure effect on sliding wear of 316L stainless steel selectively laser melted, *Materials Science and Technology* (2024). <https://doi.org/10.1177/02670836231217393>.
- [24] D. D’Andrea, Additive Manufacturing of AISI 316L Stainless Steel: A Review, *Metals (Basel)* 13 (2023). <https://doi.org/10.3390/met13081370>.
- [25] M. Hemachandra, S. Thapliyal, K. Adepu, A review on microstructural and tribological performance of additively manufactured parts, *J Mater Sci* 57 (2022) 17139–17161.
<https://doi.org/10.1007/s10853-022-07736-1>.
- [26] R. Moshfegh, E. Schedin, G. Li, H. He, A CORROSION MANAGEMENT AND APPLICATIONS ENGINEERING MAGAZINE FROM OUTOKUMPU Using Duplex Grades in Demanding Forming Operations-a CAE Based Product Development Using Duplex Grades in Demanding Forming Operations-a CAE Based Product Development, n.d.

- [27] G.A. Kantonen Tuomas, Producing novel stainless steels by laser powder bed fusion, n.d. https://www.utupub.fi/bitstream/handle/10024/174714/Kantonen_Tuomas_Thesis.pdf?sequence=1 (accessed January 6, 2024).
- [28] C. Nayak, A. Anand, N. Kamboj, T. Kantonen, K. Kajander, V. Tupala, T.J. Heino, R. Cherukuri, G. Mohanty, J. Čapek, E. Polatidis, S. Goel, A. Salminen, A. Ganvir, Tribological behavior and biocompatibility of novel Nickel-Free stainless steel manufactured via laser powder bed fusion for biomedical applications, *Mater Des* (2024) 113013. <https://doi.org/10.1016/J.MATDES.2024.113013>.
- [29] A. Adetunla, S. Afolalu, T.C. Jen, A. Ogundana, The Advances of Tribology in Materials and Energy Conservation and Engineering Innovation, in: *E3S Web of Conferences*, EDP Sciences, 2023. <https://doi.org/10.1051/e3sconf/202339101014>.
- [30] G.S. Frankel, Electrochemical Techniques in Corrosion: Status, Limitations, and Needs, *J ASTM Int* 5 (2008) JAI101241. <https://doi.org/10.1520/JAI101241>.
- [31] P. Ponthiaux, F. Wenger, J.-P. Celis, Tribocorrosion: Material Behavior Under Combined Conditions of Corrosion and Mechanical Loading, in: H. Shih (Ed.), *Corrosion Resistance*, IntechOpen, Rijeka, 2012: p. Ch. 4. <https://doi.org/10.5772/35634>.
- [32] W.S. Shin, B. Son, W. Song, H. Sohn, H. Jang, Y.J. Kim, C. Park, Heat treatment effect on the microstructure, mechanical properties, and wear behaviors of stainless steel 316L prepared via selective laser melting, *Materials Science and Engineering: A* 806 (2021). <https://doi.org/10.1016/j.msea.2021.140805>.
- [33] C. Orgeldinger, A. Seynstahl, T. Rosnitschek, S. Tremmel, Surface Properties and Tribological Behavior of Additively Manufactured Components: A Systematic Review, *Lubricants* 11 (2023). <https://doi.org/10.3390/lubricants11060257>.
- [34] A.M. Ralls, M. John, J. Noud, J. Lopez, K. LeSourd, I. Napier, N. Hallas, P.L. Menezes, Tribological, Corrosion, and Mechanical Properties of Selective Laser Melted Steel, *Metals (Basel)* 12 (2022). <https://doi.org/10.3390/met12101732>.
- [35] Low, medium, and high-carbon steel: everything you need to know, (2023). <https://www.essentracomponents.com/en-us/news/solutions/access-hardware/low-medium-high-carbon-steel> (accessed March 9, 2024).
- [36] Alloy Steel Vs Carbon Steel: Which One Is Better To Choose?, (2023). <https://waykenrm.com/blogs/alloy-steel-vs-carbon-steel/> (accessed March 9, 2024).
- [37] Team Xometry, High-Carbon Steel: Uses, Composition, and Its Properties, (2023). <https://www.xometry.com/resources/materials/high-carbon-steel/> (accessed March 9, 2024).
- [38] A.R. Marder, The metallurgy of zinc-coated steel, *Prog Mater Sci* 45 (2000) 191–271. [https://doi.org/https://doi.org/10.1016/S0079-6425\(98\)00006-1](https://doi.org/https://doi.org/10.1016/S0079-6425(98)00006-1).

- [39] G.P. Thomas, *The History of Stainless Steel – Celebrating 100 Years*, (2013).
<https://www.azom.com/article.aspx?ArticleID=8307#:~:text=In%201913%2C%20Harry%20Brearley%20of,metal%20that%20did%20not%20rust.> (accessed March 9, 2024).
- [40] Wikipedia contributors, *Stainless steel*, Wikipedia, The Free Encyclopedia (2024).
https://en.wikipedia.org/w/index.php?title=Stainless_steel&oldid=1211852740 (accessed March 9, 2024).
- [41] © Outokumpu, *Handbook of Stainless Steel*, n.d.
- [42] E. Mujanović, *Depassivation and Repassivation of Stainless Steels* Chair of General and Analytical Chemistry Lehrstuhl für Modellierung und Simulation metallurgischer Prozesse Doctoral Thesis, 2020.
- [43] M.F. McGuire, *Stainless steels for design engineers*, ASM International, 2008.
- [44] H. Mohrbacher, A. Kern, *Nickel Alloying in Carbon Steel: Fundamentals and Applications*, *Alloys 2* (2023) 1–28. <https://doi.org/10.3390/alloys2010001>.
- [45] R. Naraghi, *Martensitic Transformation in Austenitic Stainless Steels*, 2009.
- [46] Y. Chen, F. Zhang, Q. Yan, X. Zhang, Z. Hong, *Microstructure characteristics of 12Cr ferritic/martensitic steels with various yttrium additions*, *Journal of Rare Earths* 37 (2019) 547–554. <https://doi.org/https://doi.org/10.1016/j.jre.2018.08.013>.
- [47] M. Ismail, M. Bassiouni, *Evaluation of the Microstructure and Localized Corrosion Behaviour of AISI 2507 Super Duplex Stainless Steel Welds*, 2012.
- [48] C. Cui, V. Uhlenwinkel, A. Schulz, H.W. Zoch, *Austenitic stainless steel powders with increased nitrogen content for laser additive manufacturing*, *Metals (Basel)* 10 (2020).
<https://doi.org/10.3390/met10010061>.
- [49] J.-O. Andersson, T. Helander, L. Höglund, P. Shi, B. Sundman, *Thermo-Calc & DICTRA, computational tools for materials science*, *Calphad* 26 (2002) 273–312.
[https://doi.org/https://doi.org/10.1016/S0364-5916\(02\)00037-8](https://doi.org/https://doi.org/10.1016/S0364-5916(02)00037-8).
- [50] I. Stainless Steel Forum, *The Stainless Steel Family*, n.d. www.worldstainless.org.
- [51] S. Chandra-Ambhorn, S. Hayashi, L. Latu-Romain, P. Wongpromrat, *CHAPTER 4 High Temperature Oxidation of Stainless Steels*, *Solid State Phenomena* 300 (2020) 81–106.
<https://doi.org/10.4028/www.scientific.net/SSP.300.81>.
- [52] B. Li, S. Zhang, S. Wang, L. Wang, Y. He, Y. Cui, D. Liu, M. Wang, *Effects of Mo Particles Addition on the Microstructure and Properties of 316 L Stainless Steels Fabricated by Laser Powder Bed Fusion*, *Materials* 16 (2023). <https://doi.org/10.3390/ma16134827>.
- [53] J. Li, Y. Xu, X. Xiao, J. Zhao, L. Jiang, J. Hu, *A new resource-saving, high manganese and nitrogen super duplex stainless steel 25Cr-2Ni-3Mo-xMn-N*, *Materials Science and Engineering: A* 527 (2009) 245–251. <https://doi.org/10.1016/j.msea.2009.07.065>.
- [54] J. Da-wei, G. Chang-sheng, Z. Xiang-juan, L. Jun, S. Lu-lu, X. Xue-shan, *22Cr High-Mn-N Low-Ni Economical Duplex Stainless Steels*, 1050. www.sciencedirect.com.

- [55] Y. Kim, Y.S. Kim, Synergistic Effect of Nitrogen and Molybdenum on Localized Corrosion of Stainless Steels, 2010. <https://www.researchgate.net/publication/267790854>.
- [56] K.K. Pradhan, C.R. Matawale, Heat treatment analysis of SS304 for gas turbine application, *Mater Today Proc* 33 (2020) 5734–5739. <https://doi.org/https://doi.org/10.1016/j.matpr.2020.05.102>.
- [57] M. Farooq, Strengthening and degradation mechanisms in austenitic stainless steels at elevated temperature, KTH Royal Institute of Technology, 2013.
- [58] Team Xometry, Austenitic Stainless Steel: Definition, Composition, Types, Grades, Properties, and Applications, (2023). <https://www.xometry.com/resources/materials/austenitic-stainless-steel/> (accessed March 10, 2024).
- [59] T.W. Mukarati, Constitutive modelling of the strain hardening behaviour of metastable AISI 301LN austenitic stainless steel as a function of strain and temperature, 2020.
- [60] V. Zatkalíková, M. Uhrčík, L. Markovičová, L. Pastierovičová, L. Kuchariková, The Effect of Sensitization on the Susceptibility of AISI 316L Biomaterial to Pitting Corrosion, *Materials* 16 (2023). <https://doi.org/10.3390/ma16165714>.
- [61] DESIGN GUIDELINES FOR THE SELECTION AND USE OF STAINLESS STEEL NiDI Distributed by NICKEL DEVELOPMENT INSTITUTE courtesy of AMERICAN IRON AND STEEL INSTITUTE AND SPECIALTY STEEL INSTITUTE OF NORTH AMERICA, n.d.
- [62] M. Knyazeva, M. Pohl, Duplex Steels: Part I: Genesis, Formation, Structure, Metallography, Microstructure, and Analysis 2 (2013) 113–121. <https://doi.org/10.1007/s13632-013-0066-8>.
- [63] Iris. Alvarez-Armas, Suzanne. Degallaix-Moreuil, Duplex stainless steels, ISTE, 2009.
- [64] S. Patra, A. Agrawal, A. Mandal, A.S. Podder, Characteristics and Manufacturability of Duplex Stainless Steel: A Review, *Transactions of the Indian Institute of Metals* 74 (2021) 1089–1098. <https://doi.org/10.1007/s12666-021-02278-7>.
- [65] Ralph Davison & James Redmon, Practical guide to using duplex stainless steel, n.d. https://www.nickelinstitute.org/media/1764/practicalguidetousingduplexstainlesssteel_10044_.pdf (accessed March 10, 2024).
- [66] Duplex Stainless Steels: Part Two, Total Materia (n.d.). <https://www.totalmateria.com/page.aspx?ID=CheckArticle&site=kts&NM=210> (accessed March 10, 2024).
- [67] Dr. James Fritz, Practical guide to using duplex stainless steels, n.d.
- [68] M. Liljas, P. Johansson, H.-P. Liu, C.-O. Olsson, Development of a Lean Duplex Stainless Steel, *Steel Res Int* 79 (2008) 466–473. <https://doi.org/10.1002/srin.200806154>.
- [69] C. Zitelli, P. Folgarait, A. Di Schino, Laser powder bed fusion of stainless steel grades: A review, *Metals (Basel)* 9 (2019). <https://doi.org/10.3390/met9070731>.
- [70] P. Cătălin IANCU, E. Daniela IANCU, D. Alin STĂNCIOIU, Fiabilitate si Durabilitate- Fiability & Durability nr.1/2010 Editura, n.d.

- [71] I. Yadroitsev, I. Yadroitsava, A. Du Plessis, 2 - Basics of laser powder bed fusion, in: I. Yadroitsev, I. Yadroitsava, A. du Plessis, E. MacDonald (Eds.), *Fundamentals of Laser Powder Bed Fusion of Metals*, Elsevier, 2021: pp. 15–38. [https://doi.org/https://doi.org/10.1016/B978-0-12-824090-8.00024-X](https://doi.org/10.1016/B978-0-12-824090-8.00024-X).
- [72] B.J. Simonds, J. Tanner, A. Artusio-Glimpse, P.A. Williams, N. Parab, C. Zhao, T. Sun, The causal relationship between melt pool geometry and energy absorption measured in real time during laser-based manufacturing, *Appl Mater Today* 23 (2021) 101049. [https://doi.org/https://doi.org/10.1016/j.apmt.2021.101049](https://doi.org/10.1016/j.apmt.2021.101049).
- [73] C. Chua, Y. Liu, R.J. Williams, C.K. Chua, S.L. Sing, In-process and post-process strategies for part quality assessment in metal powder bed fusion: A review, *J Manuf Syst* 73 (2024) 75–105. [https://doi.org/https://doi.org/10.1016/j.jmsy.2024.01.004](https://doi.org/10.1016/j.jmsy.2024.01.004).
- [74] R. McCann, M. Obeidi, C. Hughes, E. McCarthy, D. Egan, R. Vijayaraghavan, A. Joshi, V. Garzon, D. Dowling, P. McNally, D. Brabazon, In-Situ Sensing, Process Monitoring and Machine Control in Laser Powder Bed Fusion: A Review, *Addit Manuf* 45 (2021) 102058. <https://doi.org/10.1016/j.addma.2021.102058>.
- [75] T. Herzog, M. Brandt, A. Trinchi, A. Sola, A. Molotnikov, Process monitoring and machine learning for defect detection in laser-based metal additive manufacturing, *J Intell Manuf* 35 (2023) 1–31. <https://doi.org/10.1007/s10845-023-02119-y>.
- [76] S. Cacace, M. Boccadoro, Q. Semeraro, Investigation on the effect of the gas-to-metal ratio on powder properties and PBF-LB/M processability, *Progress in Additive Manufacturing* (2023). <https://doi.org/10.1007/s40964-023-00490-z>.
- [77] S. Yim, H. Bian, K. Aoyagi, K. Yamanaka, A. Chiba, Effect of powder morphology on flowability and spreading behavior in powder bed fusion additive manufacturing process: A particle-scale modeling study, *Addit Manuf* 72 (2023). <https://doi.org/10.1016/j.addma.2023.103612>.
- [78] I. Baesso, D. Karl, A. Spitzer, A. Gurlo, J. Günster, A. Zocca, Characterization of powder flow behavior for additive manufacturing, *Addit Manuf* 47 (2021). <https://doi.org/10.1016/j.addma.2021.102250>.
- [79] C.Y. Yap, C.K. Chua, Z.L. Dong, Z.H. Liu, D.Q. Zhang, L.E. Loh, S.L. Sing, Review of selective laser melting: Materials and applications, *Appl Phys Rev* 2 (2015). <https://doi.org/10.1063/1.4935926>.
- [80] M.H. Ghoncheh, A. Shahriari, N. Birbilis, M. Mohammadi, Process-microstructure-corrosion of additively manufactured steels: a review, *Critical Reviews in Solid State and Materials Sciences* (2023). <https://doi.org/10.1080/10408436.2023.2255616>.
- [81] A. Evangelou, R. Stylianou, A. Loizou, D. Kim, A. Liang, P. Reed, G. Constantinides, T. Kyratsi, Effects of process parameters and scan strategy on the microstructure and density of

- stainless steel 316 L produced via laser powder bed fusion, *Journal of Alloys and Metallurgical Systems* 3 (2023) 100027. <https://doi.org/https://doi.org/10.1016/j.jalmes.2023.100027>.
- [82] B. Cheng, S. Shrestha, K. Chou, Stress and deformation evaluations of scanning strategy effect in selective laser melting, *Addit Manuf* 12 (2016) 240–251. <https://doi.org/10.1016/j.addma.2016.05.007>.
- [83] D. Buchbinder, W. Meiners, N. Pirch, K. Wissenbach, J. Schrage, Investigation on reducing distortion by preheating during manufacture of aluminum components using selective laser melting, *J Laser Appl* 26 (2013) 012004. <https://doi.org/10.2351/1.4828755>.
- [84] P. Bajaj, A. Hariharan, A. Kini, P. Kürnsteiner, D. Raabe, E.A. Jägler, Steels in additive manufacturing: A review of their microstructure and properties, *Materials Science and Engineering: A* 772 (2020). <https://doi.org/10.1016/j.msea.2019.138633>.
- [85] I. Tolosa, F. Garciandía, F. Zubiri, F. Zapirain, A. Esnaola, Study of mechanical properties of AISI 316 stainless steel processed by “selective laser melting”, following different manufacturing strategies, *International Journal of Advanced Manufacturing Technology* 51 (2010) 639–647. <https://doi.org/10.1007/s00170-010-2631-5>.
- [86] A. Röttger, K. Geenen, M. Windmann, F. Binner, W. Theisen, Comparison of microstructure and mechanical properties of 316 L austenitic steel processed by selective laser melting with hot-isostatic pressed and cast material, *Materials Science and Engineering: A* 678 (2016) 365–376. <https://doi.org/10.1016/j.msea.2016.10.012>.
- [87] J. Yu, M. Rombouts, G. Maes, Cracking behavior and mechanical properties of austenitic stainless steel parts produced by laser metal deposition, *Mater Des* 45 (2013) 228–235. <https://doi.org/10.1016/j.matdes.2012.08.078>.
- [88] G. Zhu, D. Li, A. Zhang, G. Pi, Y. Tang, The influence of standoff variations on the forming accuracy in laser direct metal deposition, *Rapid Prototyp J* 17 (2011) 98–106. <https://doi.org/10.1108/13552541111113844>.
- [89] Y. Xue, A. Pascu, M.F. Horstemeyer, L. Wang, P.T. Wang, Microporosity effects on cyclic plasticity and fatigue of LENSTM-processed steel, *Acta Mater* 58 (2010) 4029–4038. <https://doi.org/10.1016/j.actamat.2010.03.014>.
- [90] M. Ma, Z. Wang, D. Wang, X. Zeng, Control of shape and performance for direct laser fabrication of precision large-scale metal parts with 316L Stainless Steel, *Opt Laser Technol* 45 (2013) 209–216. <https://doi.org/10.1016/j.optlastec.2012.07.002>.
- [91] C.R. Xavier, H.G.D. Junior, J.A. De Castro, An experimental and numerical approach for the welding effects on the duplex stainless steel microstructure, *Materials Research* 18 (2015) 489–502. <https://doi.org/10.1590/1516-1439.302014>.
- [92] Y. Yin, Q. Tan, M. Bermingham, N. Mo, J. Zhang, M.X. Zhang, Laser additive manufacturing of steels, *International Materials Reviews* 67 (2022) 487–573. <https://doi.org/10.1080/09506608.2021.1983351>.

- [93] S. Astafurov, E. Astafurova, Phase composition of austenitic stainless steels in additive manufacturing: A review, *Metals (Basel)* 11 (2021). <https://doi.org/10.3390/met11071052>.
- [94] O.O. Salman, C. Gammer, A.K. Chaubey, J. Eckert, S. Scudino, Effect of heat treatment on microstructure and mechanical properties of 316L steel synthesized by selective laser melting, *Materials Science and Engineering: A* 748 (2019) 205–212. <https://doi.org/10.1016/j.msea.2019.01.110>.
- [95] M. Xu, H. Guo, Y. Wang, Y. Hou, Z. Dong, L. Zhang, Mechanical properties and microstructural characteristics of 316L stainless steel fabricated by laser powder bed fusion and binder jetting, *Journal of Materials Research and Technology* 24 (2023) 4427–4439. <https://doi.org/10.1016/j.jmrt.2023.04.069>.
- [96] V.B. Vukkum, R.K. Gupta, Review on corrosion performance of laser powder-bed fusion printed 316L stainless steel: Effect of processing parameters, manufacturing defects, post-processing, feedstock, and microstructure, *Mater Des* 221 (2022). <https://doi.org/10.1016/j.matdes.2022.110874>.
- [97] Z. Sun, X. Tan, S.B. Tor, C.K. Chua, Simultaneously enhanced strength and ductility for 3D-printed stainless steel 316L by selective laser melting, *NPG Asia Mater* 10 (2018) 127–136. <https://doi.org/10.1038/s41427-018-0018-5>.
- [98] Y.M. Wang, T. Voisin, J.T. McKeown, J. Ye, N.P. Calta, Z. Li, Z. Zeng, Y. Zhang, W. Chen, T.T. Roehling, R.T. Ott, M.K. Santala, P.J. Depond, M.J. Matthews, A. V. Hamza, T. Zhu, Additively manufactured hierarchical stainless steels with high strength and ductility, *Nat Mater* 17 (2018) 63–70. <https://doi.org/10.1038/NMAT5021>.
- [99] H. Xiang, W. Zhao, Y. Lu, Effect of solution temperature on microstructure and mechanical properties of selective laser melted Fe-22Cr-5Ni-0.26N duplex stainless steel, *Journal of Materials Research and Technology* 19 (2022) 1379–1389. <https://doi.org/10.1016/j.jmrt.2022.05.124>.
- [100] F. Hengsbach, P. Koppa, K. Duschik, M.J. Holzweissig, M. Burns, J. Nellesen, W. Tillmann, T. Tröster, K.P. Hoyer, M. Schaper, Duplex stainless steel fabricated by selective laser melting - Microstructural and mechanical properties, *Mater Des* 133 (2017) 136–142. <https://doi.org/10.1016/j.matdes.2017.07.046>.
- [101] M.K. Bikramjit Basu, Introduction, in: *Tribology of Ceramics and Composites*, 2011: pp. 1–6. <https://doi.org/https://doi.org/10.1002/9781118021668.ch1>.
- [102] M.K. Bikramjit Basu, Wear Mechanisms, in: *Tribology of Ceramics and Composites*, 2011: pp. 70–100. <https://doi.org/https://doi.org/10.1002/9781118021668.ch7>.
- [103] H. Czichos, Tribological Systems, in: H. Czichos (Ed.), *Introduction to Systems Thinking and Interdisciplinary Engineering*, Springer International Publishing, Cham, 2022: pp. 37–71. https://doi.org/10.1007/978-3-031-18239-6_3.

- [104] T. Bakalova, K. Boruvková, P. Louda, M. Atanasova, TYPE LIQUID LUBRICANTS AS AN ACTIVE FULL-FLEDGED ELEMENT OF THE TRIBOLOGICAL SYSTEM, (2015).
- [105] C.S. Yust, Tribology and wear, International Metals Reviews 30 (1985) 141–154.
<https://doi.org/10.1179/imtr.1985.30.1.141>.
- [106] A. Tsujimoto, W.W. Barkmeier, N.G. Fischer, K. Nojiri, Y. Nagura, T. Takamizawa, M.A. Latta, M. Miazaki, Wear of resin composites: Current insights into underlying mechanisms, evaluation methods and influential factors, Japanese Dental Science Review 54 (2018) 76–87.
<https://doi.org/10.1016/j.jdsr.2017.11.002>.
- [107] Dieter Landolt, Corrosion and Surface Chemistry of Metals, 1st Edition, EPFL Press, 2007.
- [108] A. Igual Munoz, N. Espallargas, S. Mischler, Corrosion Basis, in: A. Igual Munoz, N. Espallargas, S. Mischler (Eds.), Tribocorrosion, Springer International Publishing, Cham, 2020: pp. 7–17. https://doi.org/10.1007/978-3-030-48107-0_2.
- [109] B. Popov, Evaluation of Corrosion, in: 2015: pp. 1–28. <https://doi.org/10.1016/B978-0-444-62722-3.00001-X>.
- [110] J.R.S.D.S.R.G.B. Robert G. Kelly, Electrochemical Techniques in Corrosion Science and Engineering, 1st ed., CRC Press, 2002.
- [111] H.-B. Choe, H.-S. Lee, M.A. Ismail, M. Warid Hussin, J. Bahru, Evaluation of Electrochemical Impedance Properties of Anti-corrosion Films by Arc Thermal Metal Spraying Method, 2015. www.electrochemsci.org.
- [112] A. Revathi, U. Vijayalakshmi, M. Geetha, Comparative study of electrochemical behaviour of CP-titanium and Ti-6Al-4V with other titanium based alloys for biomedical applications, Materials Technology 29 (2014). <https://doi.org/10.1179/1753555713Y.0000000109>.
- [113] Engineering Materials Lab at ETH Zurich, Tafel extrapolation, (n.d).
<https://www.youtube.com/watch?v=jRTeSTNCU8> (accessed May 5, 2024).
- [114] A. Igual Munoz, N. Espallargas, S. Mischler, Tribocorrosion Phenomena and Concepts, in: A. Igual Munoz, N. Espallargas, S. Mischler (Eds.), Tribocorrosion, Springer International Publishing, Cham, 2020: pp. 35–42. https://doi.org/10.1007/978-3-030-48107-0_4.
- [115] A. Igual Munoz, N. Espallargas, S. Mischler, Tribocorrosion: Definitions and Relevance, in: A. Igual Munoz, N. Espallargas, S. Mischler (Eds.), Tribocorrosion, Springer International Publishing, Cham, 2020: pp. 1–6. https://doi.org/10.1007/978-3-030-48107-0_1.
- [116] A. López-Ortega, J.L. Arana, R. Bayón, Tribocorrosion of Passive Materials: A Review on Test Procedures and Standards, International Journal of Corrosion 2018 (2018).
<https://doi.org/10.1155/2018/7345346>.
- [117] J. Stendal, O. Fergani, H. Yamaguchi, N. Espallargas, A Comparative Tribocorrosion Study of Additive Manufactured and Wrought 316L Stainless Steel in Simulated Body Fluids, J Bio Tribocorros 4 (2018). <https://doi.org/10.1007/s40735-017-0125-9>.

- [118] R. Gao, E. Liu, Y. Zhang, L. Zhu, Z. Zeng, Tribocorrosion Behavior of SAF 2205 Duplex Stainless Steel in Artificial Seawater, *J Mater Eng Perform* 28 (2019) 414–422. <https://doi.org/10.1007/s11665-018-3791-y>.
- [119] Thermo-Calc Software, Sweden, (n.d.). <https://thermocalc.com/about-us/advance/partners/> (accessed May 23, 2024).
- [120] InfiniteFocus G6, (n.d.). <https://www.alicon.com/en/products/infinitefocus> (accessed May 23, 2024).
- [121] MALVERN MASTERSIZER 3000+ ULTRA, (n.d.). <https://www.atascientific.com.au/products/malvern-mastersizer-3000-ultra/> (accessed May 23, 2024).
- [122] FALCON 600 MICRO HARDNESS TESTER, (n.d.). <https://www.innovatest-europe.com/products/falcon-600/> (accessed May 23, 2024).
- [123] Empyrean Multi-Purpose Research X-Ray Diffractometer XRD, (n.d.). <https://www.azonano.com/equipment-details.aspx?EquipID=374> (accessed May 23, 2024).
- [124] Zeiss Crossbeam 540, (n.d.). <https://www-em.materials.ox.ac.uk/zeiss-crossbeam-540> (accessed May 23, 2024).
- [125] Thermo Scientific Apreo 2 SEM for Materials Science, (n.d.). <https://www.azom.com/equipment-details.aspx?EquipID=5812> (accessed May 23, 2024).
- [126] M. Narvan, A. Ghasemi, E. Fereiduni, S. Kendrish, M. Elbestawi, Part deflection and residual stresses in laser powder bed fusion of H13 tool steel, *Mater Des* 204 (2021). <https://doi.org/10.1016/j.matdes.2021.109659>.
- [127] C. Nayak, A. Anand, N. Kamboj, T. Kantonen, K. Kajander, V. Tupala, T.J. Heino, R. Cherukuri, G. Mohanty, J. Čapek, E. Polatidis, S. Goel, A. Salminen, A. Ganvir, Tribological Behavior and Biocompatibility of Novel Nickel-Free Stainless Steel Manufactured via Laser Powder Bed Fusion for Biomedical Applications, n.d. <https://ssrn.com/abstract=4797813>.
- [128] M. Lavanya, V.R. Murthy, P. Rao, Electrochemical investigation of erosion-corrosion behavior of 6061 aluminum alloy in marine environment, *Tribology in Industry* 40 (2018) 552–564. <https://doi.org/10.24874/ti.2018.40.04.04>.
- [129] ASTM International, Standard Practice for Calculation of Corrosion Rates and Related Information from Electrochemical Measurements 1, n.d. <https://doi.org/10.1520/G0102-89R15E01>.
- [130] A.B. Spierings, N. Herres, G. Levy, Influence of the particle size distribution on surface quality and mechanical properties in AM steel parts, *Rapid Prototyp J* 17 (2011) 195–202. <https://doi.org/10.1108/13552541111124770>.
- [131] K. Saeidi, S. Alvi, F. Lofaj, V.I. Petkov, F. Akhtar, Advanced mechanical strength in post heat treated SLM 2507 at room and high temperature promoted by hard/ductile sigma precipitates, *Metals (Basel)* 9 (2019). <https://doi.org/10.3390/met9020199>.

- [132] K.R. Gadelrab, G. Li, M. Chiesa, T. Souier, Local characterization of austenite and ferrite phases in duplex stainless steel using MFM and nanoindentation, *J Mater Res* 27 (2012) 1573–1579. <https://doi.org/10.1557/jmr.2012.99>.
- [133] Team Xometry, Ferritic Stainless Steel: Definition, Composition, Types, Properties, and Applications, (2023). <https://www.xometry.com/resources/materials/ferritic-stainless-steel/> (accessed March 10, 2024).
- [134] K.A. Cashell, N.R. Baddoo, Ferritic stainless steels in structural applications, *Thin-Walled Structures* 83 (2014) 169–181. <https://doi.org/https://doi.org/10.1016/j.tws.2014.03.014>.
- [135] P. Cheng, N. Zhong, N. Dai, X. Wu, J. Li, Y. Jiang, Intergranular corrosion behavior and mechanism of the stabilized ultra-pure 430LX ferritic stainless steel, *J Mater Sci Technol* 35 (2019) 1787–1796. <https://doi.org/https://doi.org/10.1016/j.jmst.2019.03.021>.

Appendices

Appendix 1 Ferritic stainless steel

The ferritic grade SS are chromium alloyed (more than 11 wt%), with minimal or no nickel addition [41]. These are the simplest and most economical variants of SS. Some grades include molybdenum for enhanced corrosion resistance, while niobium or titanium are added to improve weldability [43]. These Cr-steels exhibit magnetism due to their ferritic microstructure. While their strength is comparable with austenitic grades, due to the unavailability of nickel, they lack ductility and have poor formability. They showcase brittleness at cryogenic temperatures. Higher thermal conductivity, oxidation resistance, and better thermal fatigue resistance make ferritic grades suitable for high-temperature applications such as heat exchangers and boiler tubes [133]. Ferritic grades are widely utilized in structural components and equipment for chemical processing industries subjected to mildly corrosive environments [134]. Ferritic grades exhibit lower corrosion resistance than austenitic SS primarily due to their lower chromium content and poor nitrogen solubility. Further, ferritic grades are more prone to intergranular corrosion than austenitic SS due to the precipitation of chromium nitrides [135].

Appendix 2 Images

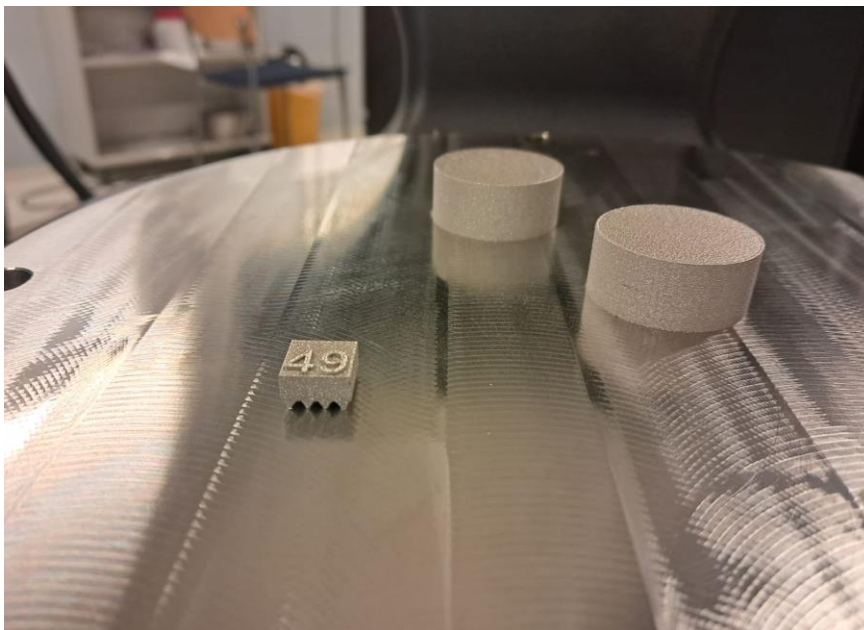


Figure A 1. As-built 316L samples.



Figure A 2. As-built NiFDSS samples after the second trial of process parameter optimization.

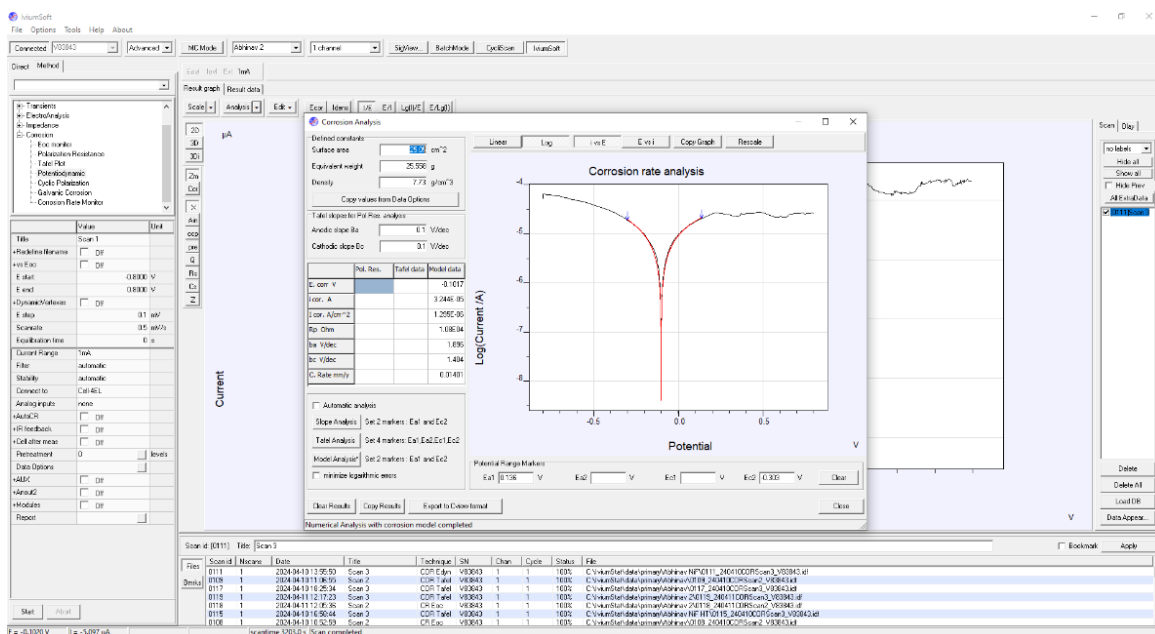


Figure A 3. IviumSoft software used in the C.R. calculation of as-built NiFDSS in static condition using model data analysis.

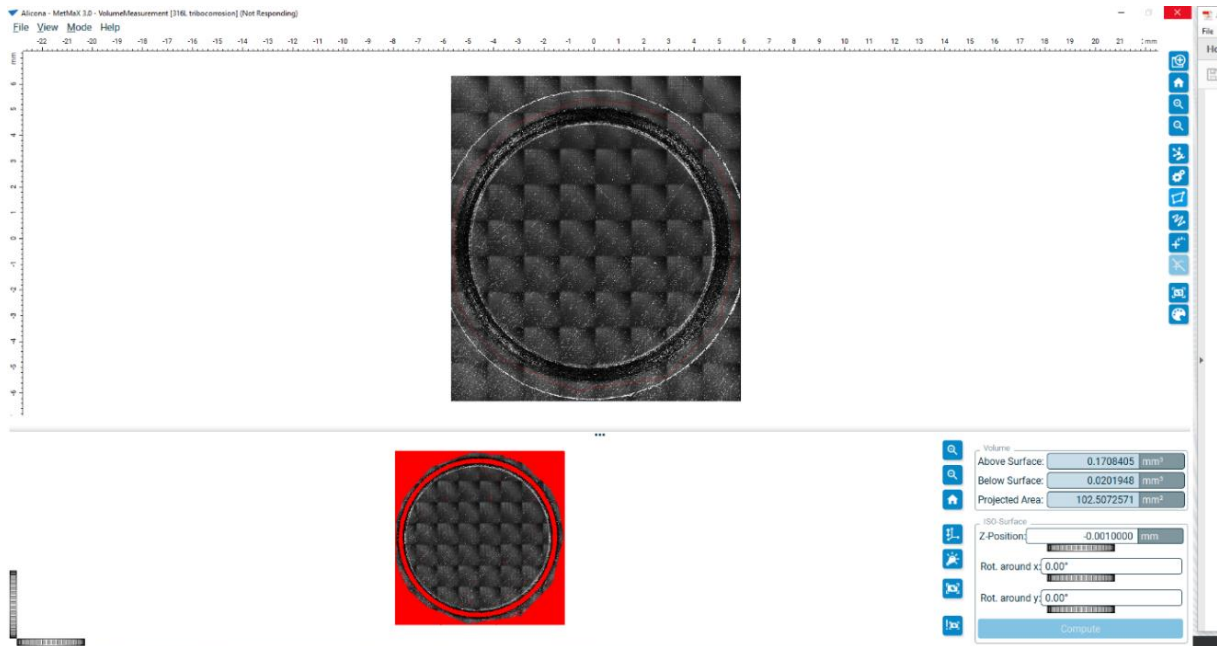


Figure A 4. As-built 316L wear volume calculation using MetaMax software.